# Long-lived (180 Myr) ductile flow within the Great Slave Lake shear zone

Dana Šilerová[1], Brendan Dyck[2], Jamie A Cutts[3], and Kyle Larson[2]

[1]Simon Fraser University
[2]University of British Columbia
[3]Geological Survey of Canada

December 21, 2022

**Abstract**

The Great Slave Lake shear zone (GSLsz) is a type example for deeply eroded continental transform boundaries located in the Northwest Territories, Canada. Formed during the oblique convergence of the Archean Rae and Slave cratons, the GSLsz has accommodated up to 700 km of dextral shear. Here we present the results of in situ U-Pb apatite and titanite geochronology from 11 samples that were collected across the strike of the shear zone. Both geochronometers record a near-continuous history of ductile shear during crustal cooling and exhumation that spans ca. 1920–1740 Ma. By integrating the geochronological data with structural and metamorphic observations across the structure, we propose a tectonic model for the shear zone that consists of three stages. The first stage (ca. 1920–1880 Ma) is characterized by strain accommodation along two coeval fault strands. During the second stage (ca. 1880–1800 Ma), ductile shear ceases along the northernmost fault strand and the locus of strain migrates southwards towards the hinterland of the Rae cratonic margin. In the third stage (ca. 1800–1740 Ma), ductile strain localizes back along the southern of the two original fault strands, after which the present-day surface level of the shear zone transitions to brittle shear. Our results highlight both the significance of the lateral migration of the zone of active deformation in major crustal shear zones as well as the localization of strain along existing crustal structures.

# Long-lived (180 Myr) ductile flow within the Great Slave Lake shear zone

**D. Šilerová[1], B. Dyck[2], J. A. Cutts[2,3], and K. Larson[2]**

[1]Department of Earth Sciences, Simon Fraser University, Burnaby, BC, Canada

[2]Department of Earth, Environmental and Geographical Sciences, University of British Columbia, Kelowna, BC, Canada

[3]Geological Survey of Canada, 601 Booth Street, K1A 0E8, Ottawa, ON, Canada

Corresponding author: Dana Šilerová (dana.silerova@smu.ca)

**Key Points:**

- (Re)crystallized apatite and titanite record a near-continuous history of ductile shear spanning ca. 1920–1740 Ma.
- Strain was initially (ca. 1920–1880 Ma) accommodated by two coeval fault strands.
- A faultward younging in the timing of (re)crystallization is consistent with strain localization during cooling and exhumation.

## Abstract

The Great Slave Lake shear zone (GSLsz) is a type example for deeply eroded continental transform boundaries located in the Northwest Territories, Canada. Formed during the oblique convergence of the Archean Rae and Slave cratons, the GSLsz has accommodated up to 700 km of dextral shear. Here we present the results of *in situ* U-Pb apatite and titanite geochronology from 11 samples that were collected across the strike of the shear zone. Both geochronometers record a near-continuous history of ductile shear during crustal cooling and exhumation that spans ca. 1920–1740 Ma. By integrating the geochronological data with structural and metamorphic observations across the structure, we propose a tectonic model for the shear zone that consists of three stages. The first stage (ca. 1920–1880 Ma) is characterized by strain accommodation along two coeval fault strands. During the second stage (ca. 1880–1800 Ma), ductile shear ceases along the northernmost fault strand and the locus of strain migrates southwards towards the hinterland of the Rae cratonic margin. In the third stage (ca. 1800–1740 Ma), ductile strain localizes back along the southern of the two original fault strands, after which the present-day surface level of the shear zone transitions to brittle shear. Our results highlight both the significance of the lateral migration of the zone of active deformation in major crustal shear zones as well as the localization of strain along existing crustal structures.

## 1 Introduction

Crustal-scale shear zones preserve a record of the temporal and structural evolution of the ductile portions of continental plate boundaries. Over the past few decades, there has been extensive research into the rheological behavior of crustal-scale shear zones (e.g., Scholz, 1988; Sibson, 1977, 1983) leading to a robust understanding of the physical manifestation of plate boundaries at depth (Cawood & Platt, 2021; Lusk & Platt, 2020; Platt & Behr, 2011). However, despite the integral role of these structures in controlling lithospheric strength over long geological periods, there is a general lack of data related to the spatial and temporal evolution of crustal-scale shear zones. The challenges associated with collecting and interpreting geochronological data in shear zones reflect the inherent complexity of shear zone histories as well as the effects of various processes on isotopic diffusion in mineral systems (see Oriolo et al., 2018 and references therein).

The Paleoproterozoic Great Slave Lake shear zone (GSLsz), located in the Northwest Territories, Canada, is a crustal-scale dextral transcurrent structure that marks the boundary between the Archean Rae and Slave cratons (Hanmer, 1988; Hanmer & Lucas, 1985; Hoffman, 1987). Stretching over 1000 km in length, and reaching up to 25 km in width, the GSLsz is one of the largest and best exposed Paleoproterozoic continental transform boundaries in the world. The GSLsz formed as a result of oblique convergence between those cratons, following initial collision ca. 1.95 Ga (Cutts & Dyck, 2022; Gibb & Thomas, 1977).

Extensive surface erosion synchronous with deformation along the GSLsz resulted in the exposure of a series of distinct mylonitic belts within the shear zone (Hanmer, 1988; Hanmer & Lucas, 1985) that preserve a continuous range of metamorphic conditions from the lower greenschist to granulite facies (Hanmer & Lucas, 1985). These mylonitic belts effectively comprise metamorphic units that exhibit decreasing width with decreasing metamorphic grade; the narrower, greenschist-grade belts are overprinted by brittle deformation features (Dyck et al., 2021; Hanmer, 1988; Hanmer et al., 1992). Because these observations are consistent with previously published fault zone models (e.g., Scholz, 1988; Sibson, 1977, 1983), the GSLsz has long been identified as a type example for deeply eroded continental transform boundaries (Dyck et al., 2021; Hanmer, 1988).

Although recent work has answered some of the fundamental questions surrounding the structure and metamorphic evolution of the GSLsz (Cutts & Dyck, 2022; Dyck et al., 2021), the timing of shear along the plate boundary remains poorly quantified. In this study, we document the timing of (re)crystallization of apatite and titanite along the GSLsz and integrate the results with petrographic and geochemical observations. In doing so, the dates are interpreted as reflecting shear-induced (re)crystallization and, thus, provide constraint on the duration of ductile shear in the GSLsz. We present a tectonic model for the GSLsz that can serve as a framework for elucidating histories of other transcurrent continental shear zones, both modern and extinct. This work highlights the importance of integrating various sources of data in order to overcome the challenges associated with interpreting geochronological data in geologically complex systems.

## 2 Geological context

Northwestern Laurentia is an amalgamation of the Archean Slave, Rae, Hearne, and Superior cratons that were assembled along a series of distinct Paleoproterozoic orogenic belts. From west to east these belts include the Wopmay Orogen, the Taltson magmatic zone, the Thelon tectonic zone, the Snowbird tectonic zone, and the Trans-Hudson Orogen (Fig. 1a; Hoffman, 1988). The western boundary of the Rae craton is itself divided into three segments, with the GSLsz forming the central segment. To the northeast of the GSLsz, the Thelon tectonic zone marks the boundary between the Slave and Rae cratons, and to the southwest, the Taltson magmatic zone separates the Rae craton from the Kiskatinaw-Chinchaga-Buffalo Head Superterrane.

The combined Taltson-Thelon margin was initially thought to have formed due to the subduction of oceanic crust beneath the Rae craton and the ensuing collision between Slave and Rae ca. 1.97 Ga (Hoffman, 1987; Thériault, 1992). Recent geochemical and geochronologic work, however, has led to the recognition of the Taltson magmatic zone and Thelon tectonic zone as two distinct structures, rather than one contiguous margin that was dextrally offset by the GSLsz (Berman et al., 2018; Card et al., 2014). The Thelon tectonic zone records older magmatic ages (2.07–1.92 Ga; Berman et al., 2018) and younger metamorphic ages (1.92–1.89 Ga; Berman et al., 2018) than the Taltson magmatic zone, which records younger magmatic ages (1.99–1.92 Ga; Bostock et al., 1987, 1991; Bostock & Loveridge, 1988; Chacko et al., 2000) and older metamorphic ages (1.94–1.92 Ga; Bethune et al., 2013; McDonough et al., 2011).

The GSLsz extends over 1000 km, from the foothills of the Rocky Mountains in the west to the Thelon Basin in the east (Fig. 1a). With the western half of the structure covered by Phanerozoic sedimentary rocks, exposure of the ductile structures is restricted to its eastern half where recent glaciation has contributed to near-continuous exposure of northeast striking mylonite belts. Two major brittle faults run parallel to the strike of the mylonite foliation; the McDonald fault and the Laloche River fault (Fig. 1b). The McDonald fault marks the northern boundary of the GSLsz, separating ultramylonites from the moderately deformed plutonic rocks of the Slave craton (Cutts et al., 2022), while the Laloche River fault bisects the center of the shear zone.

This study focuses on the westernmost segment of the exposed GSLsz (Fig. 1c) where the Laloche River fault separates two distinct structural domains. South of the Laloche River fault, the mylonitic foliation strikes NE–SW, parallel to the strike of the fault, and preserves epidote-amphibolite to greenschist facies metamorphic assemblages. To the north, the foliation strikes NNE-SSW and is truncated by the Laloche River fault. This northern structural domain preserves a series of parallel mylonite belts that last equilibrated under a wide range of metamorphic facies from granulite through to greenschist. The boundaries between metamorphic units are diffuse with higher-grade units overprinted by lower-grade mineral assemblages (Dyck et al., 2021). Accordingly, we define the boundaries between units by the appearance of the lower-grade mineral assemblage (retrograde index minerals).

Rocks from the granulite, upper-amphibolite and epidote-amphibolite belts all reached similar peak metamorphic conditions (~0.85 GPa, ~750 °C), while the final stages of equilibrium recorded by all samples collectively define a single metamorphic field gradient of ~1,000 °C/GPa across the shear zone (Dyck et al., 2021). These findings are consistent with the interpretation of Dyck et al. (2021) that the various mylonitic belts of the GSLsz developed over the course of a single progressive deformation event rather than during temporally distinct events.

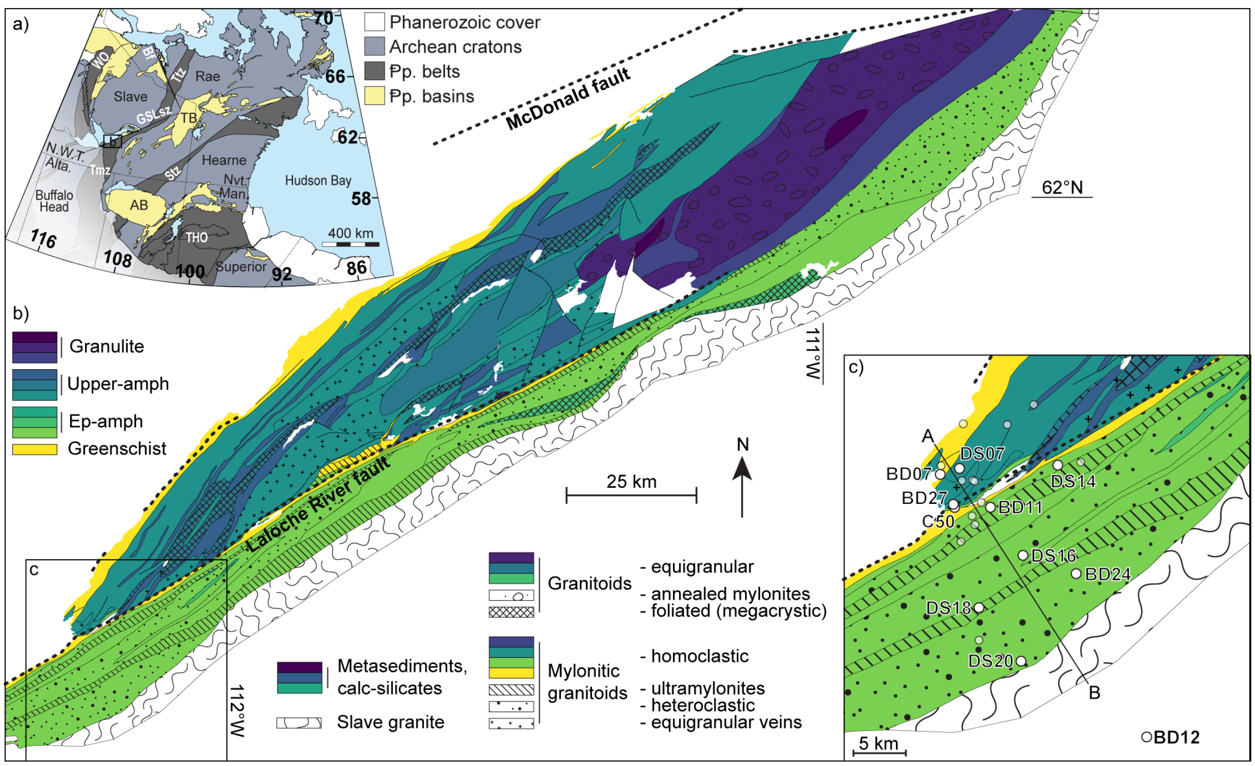


**Figure 1.** (a) Simplified bedrock map of northern Laurentia showing the positions of Archean cratons and other major tectonic elements, including the Great Slave Lake shear zone (GSLsz), Bathurst fault (Bf), Taltson magmatic zone (Tmz), Thelon tectonic zone (Ttz), Snowbird tectonic zone (Stz), Wopmay Orogen (WO), Trans-Hudson Orogen (THO), Thelon Basin (TB), and Athabasca Basin (AB). N.W.T – Northwest Territories, Alta. – Alberta, Nvt. – Nunavut, Man. – Manitoba. (b) Metamorphic units of the southwestern segment of the GSLsz. Units are based on protolith lithology as mapped by Hanmer (1988). (c) Field area with sample locations

(translucent white circles) and transect line; location shown in 1b. Samples used for accessory mineral petrochronology are labeled and marked by larger opaque white circles.

### 2.1 Previous geochronological work

Although several decades have passed since the GSLsz was first recognized as a major tectonic structure in northwestern Laurentia, there is a lack of modern geochronologic information for the timing and duration of ductile shear. Early attempts to date the structure used U-Pb ID-TIMS geochronology on zircon and the results were interpreted to indicate that peak activity of the shear zone occurred at ca. 1.980–1.924 Ga along its southwestern segment (Hanmer et al., 1992) and by 1978 ± 5 Ma along its northeastern segment (van Breemen et al., 1990). Transform motion along the shear zone was proposed to be bracketed between ca. 2.00–1.86 Ga (Bowring et al., 1984; Hanmer et al., 1992). However, the dates used to inform the timing of transform movement relied on geochronology from the host mylonitic granitoids or on interpretations of cross-cutting relationships between intrusive units and the mylonites rather than directly dating shear-induced recrystallization. Following its main period of activity, the GSLsz was offset dextrally by the McDonald fault. Late synkinematic dyke emplacement and biotite cooling ages constrain the onset of brittle deformation along the McDonald fault and conjugate Bathurst fault to ca. 1840 Ma, while a depositional age of ca. 1758 Ma for nearby synorogenic basin units has been proposed to bracket the end of brittle activity in the McDonald-Bathurst fault system (Ma et al., 2020; Rainbird & Davis, 2007).

Recent geochronological work done on samples from the southwestern segment of the GSLsz found that zircon and monazite U-Pb ages are unrelated to the transcurrent motion of the shear zone and, instead, record a margin-wide crustal thickening event associated with convergence of the Slave and Rae cratons (Cutts & Dyck, 2022). The timing of the peak metamorphism associated with crustal thickening is best informed by two garnet Lu-Hf ages of 1931 ± 12 and 1917 ± 6 Ma, which overlap the ca. 1933–1913 Ma age range recorded by zircon and monazite (Cutts & Dyck, 2022). Based on the observations of suprasolidus shear microstructures (Dyck et al., 2021; Hanmer et al., 1992), the maximum age of ductile shear along the GSLsz has been interpreted to coincide with the final stages of peak metamorphism at ca. 1920–1910 Ma (Cutts & Dyck, 2022).

## 3 Methods

### 3.1 Apatite and titanite geochronology

We conducted a ~15 km across-strike transect through the GSLsz to evaluate the record of shear-induced (re)crystallization preserved therein. Along the transect, we recorded the orientation of ductile fabrics as well as the characteristic metamorphic mineral assemblages. We collected 22 samples from which 11 were selected for *in-situ* U-Th-Pb accessory mineral petrochronology (Fig. 1c). Given the apparent lack of sensitivity of zircon and monazite to record the timing of deformation (Cutts & Dyck, 2022), we focused our study on apatite and titanite. Both minerals have a well-documented tendency to recrystallize during ductile deformation (e.g., Gordon et al., 2021; Kavanagh-Lepage et al., 2022; Moser et al., 2022; Odlum & Stockli, 2020; Ribeiro et al., 2020; Walters et al., 2022). Ten of the eleven samples are apatite-bearing and ten are titanite-bearing.

Target apatite and titanite grains were first identified in thin section using transmitted light microscopy. Following this, we collected backscattered electron (BSE; apatite, titanite) and cathodoluminescence (CL; apatite) images to determine the relationship of each grain with ductile fabrics and to identify zoning within individual grains. BSE imaging was done using the Tescan Mira 3 XMU field emission scanning electron microscope (SEM) at the Fipke Laboratory for Trace Element Research (FiLTER) at the University of British Columbia, Okanagan. For CL imaging, we used a Thermo Prisma tungsten-source SEM equipped with a four-channel polychromatic CL camera housed in the Department of Earth Sciences at Simon Fraser University. For both BSE and CL, we coated the samples with ~10 nm of carbon and used an accelerated voltage of 15 kV at a working distance of 10 mm.

*In-situ* U-Pb isotope and trace element analyses of apatite and titanite was carried out via laser ablation inductively coupled plasma mass spectrometry (LA-ICP-MS) in the FiLTER facility at the University of British Columbia, Okanagan. In total, twelve separate analytical sessions were run (four with apatite; eight with titanite). All spot analyses within individual samples were collected during the same session, except the titanite in GSL-18-C50, for which data were collected across two sessions. Five of the titanite sessions used a Photon Machines Analyte 193nm ArF excimer laser ablation system coupled to an Agilent 8900 Triple Quadrupole (QQQ) ICP-MS operated in single-quad mode. The other three titanite sessions and all four apatite sessions used an ESI New Wave Research 193nm ArF excimer laser ablation system coupled to an Agilent 8900 QQQ-ICP-MS operated in single-quad mode. Each session consisted of analyses of one to three apatite- or titanite-bearing samples. U-Pb isotopic ratios and trace element concentrations were collected from the same ablated spot volumes. Instrumentation settings for each analytical session are provided in Table S1. All U-Pb isotope and trace element data collected for unknowns and reference materials are presented in Tables S2 and S3 for apatite and titanite, respectively.

Apatite grains were ablated using a fluence of 4.00 J/cm$^2$, an ablation frequency of 8.00 Hz, and a spot size of 40 μm. Titanite grains were ablated using a fluence of 4.00–4.95 J/cm$^2$, an ablation frequency of 8.00 Hz, and a spot size between 25–40 μm. Prior to each spot analysis, the surface was pre-ablated with two laser pulses to clear the sample surface of debris. The acquisition run for each spot analysis lasted between 25–30 seconds and was followed by a washout period, lasting 10 seconds. Blocks of 8–10 unknown analyses were separated by analyses of reference materials for calibration purposes and to correct for instrumental drift and down-hole fractionation.

The primary reference material used for all apatite U-Pb LA-ICP-MS analyses was MAD1 (Thomson et al., 2012) as characterized in Apen et al. (2022; lower intercept age of 467 ± 9 Ma). Both MRC-1 (isochron age = 153.3 ± 0.2 Ma; Apen et al., 2022) and Mount McClure (common Pb corrected via total Pb-U isochron = 523.51 ± 1.53 Ma; Schoene & Bowring, 2006) apatite reference materials were analyzed as unknowns to assess reproducibility. Analyses of MRC-1 yielded lower intercept dates in Tera-Wasserburg space of 154 ± 1 Ma (mean squared weighted deviates [MSWD] = 1, n = 12/12), 155 ± 2 Ma (MSWD = 0.91, n = 14/15), 157 ± 2 Ma (MSWD = 1, n = 20/20), and 152 ± 2 Ma (MSWD = 1.7, n = 10/10). The two analytical runs that included Mount McClure apatite returned lower intercept dates of 522 ± 6 Ma (MSWD = 5.5, n = 14/15) and 531 ± 17 Ma (MSWD = 1.6, n = 19/20). With one exception, all analyses of apatite secondary reference materials overlap within uncertainty of expected ages; the one exception is within 1% of the expected age.

The reference materials used for titanite geochronology include MKED1, Mount McClure, and Mud Tank. MKED1 was used as the primary reference material for all titanite isotopic analyses ($^{206}Pb/^{238}U$ age of 1517.32 ± 32 Ma; Spandler et al., 2016). To assess the accuracy of the U-Pb results, the Mount McClure titanite reference material (common Pb corrected via total Pb-U isochron = 523.26 ± 0.72 Ma; Schoene & Bowring, 2006) was analyzed as an unknown in five analytical sessions while the titanite reference material Mud Tank (318.7 ± 1.0 Ma; Fisher et al., 2020) was used for the remaining three sessions. LA-ICP-MS analyses of Mount McClure titanite typically contain significant and variable common Pb contents. As such, lower intercept dates in Tera-Wasserburg space are used to assess how well the expected age was reproduced. Analyses of Mount McClure titanite yielded dates of 522 ± 3 Ma (MSWD = 1.7, n = 9/10), 529 ± 4 (MSWD = 0.72, n = 5/5), 523 ± 14 Ma (MSWD = 2.3, n = 6/6), 522 ± 12 Ma (MSWD = 2.1, n = 8/8), and 528 ± 4 Ma (MSWD = 1.3, n = 13/13). With one exception, all dates overlap the expected date within analytical uncertainty. The exception is well within (0.1%) the expected uncertainties associated with LA-ICP-MS U-Pb geochronology (e.g., Horstwood et al., 2016). Analyses of Mud Tank titanite were essentially homogeneous with respect to common Pb, and as such, $^{207}Pb$-corrected (Stacey & Kramers, 1975) $^{206}Pb/^{238}U$ weighted mean dates were used to assess reproducibility. The three analytical runs with Mud Tank titanite yielded dates of 319 ± 1 Ma (MSWD 2.9, n = 9/10), 316 ± 1 Ma (MSWD 1.5, n = 13/14) and 316 ± 1 Ma (MSWD 1.2, n = 17/17). All Mud Tank results are within 0.3% of the expected date, again well-within expected reproducibility.

Glasses NIST 610 and NIST 612 were used as reference materials for trace element analyses for both apatite and titanite. Concentrations were normalized to assumed stoichiometric concentrations of Ca for apatite and Si for titanite. Trace element concentrations in secondary reference materials are typically within 5–15% of expected values, with Zr < 5%.

## 3.2 U-Pb data analysis

The LA-ICP-MS data were initially reduced using Iolite (Paton et al., 2011) to normalize down-hole fractionation and instrument drift over analytical runs. Excess dispersion in the $^{207}Pb/^{206}Pb$ and $^{206}Pb/^{238}U$ ratios was calculated from secondary reference materials (e.g., Mount McClure, Mud Tank, MRC-1) and added to apatite and titanite analyses using in-house data processing scripts. Typical dispersion values were < 1.5%. Tera-Wasserburg diagrams and trace element plots were constructed using ChrontouR (Larson, 2022) and DataGraph (Visual DataTools, 2021). When constructing Tera-Wasserburg diagrams for specimens with multiple populations, the intercept of a single regression through all included data was used for the individual regressions to be internally consistent. Uncertainties reported in-text and depicted in figures refer to internal (2 standard error; 2SE) uncertainties only.

## 3.3 Zirconium-in-titanite geothermometry

Zirconium (Zr) concentrations were measured in each titanite spot analysis and (re)crystallization temperatures were calculated using the Zr-in-titanite geothermometer of Hayden et al. (2008). The activities of titania ($TiO_2$) and silica ($SiO_2$) were assumed to be 0.8 and 1.0, respectively; an activity of titania between 0.75–0.85 is considered an acceptable estimate for a wide range of metamorphic rocks (Kapp et al., 2009; Kohn, 2017). Recent estimates for the last recorded equilibrium conditions across most metamorphic units in the field area include pressures between approximately 0.4–0.7 GPa (Dyck et al., 2021). Because it is difficult to determine the equilibrium mineral assemblage associated with titanite crystallization, as well as the lack of independent pressure constraints for the samples analyzed, we chose a value of 0.5 GPa as the best approximation for pressure as it applies to the broadest range of samples. Temperatures calculated with the Zr-in-titanite geothermometer are only moderately pressure-dependent; a change in pressure of 0.1 GPa corresponds to a change in temperature of 10–13 °C for the grains analyzed. Uncertainties reported for temperatures in-text reflect the standard calibration uncertainty of ± 20 °C reported by Hayden et al. (2008).

## 4 Results

### 4.1 Sample petrography

Of the 11 samples selected for *in situ* U-Th-Pb accessory mineral petrochronology, 4 were collected north of the Laloche River fault (GSL-18-BD07, GSL-21-DS07, GSL-18-BD27, GSL-18-C50) while the remaining 7 are from south of the fault (Fig. 1c). Detailed petrographic descriptions for all samples are presented in Text S1, photomicrographs of key microstructural features in Figure 2, and grain characteristics of apatite and titanite in Table 1.

The four samples collected in the northern structural domain exhibit broad ranges in degree of mylonitization, lithology, and metamorphic facies, with three samples (GSL-21-DS07, GSL-18-BD27, GSL-18-C50) of mylonitic schist and one (GSL-18-BD07) of ultramylonitic granodiorite. The preserved metamorphic facies in the four samples range from the greenschist facies (GSL-18-BD07) to the epidote-amphibolite (GSL-21-DS07, GSL-18-C50) and upper-amphibolite facies (GSL-18-BD27). Two of the samples (GSL-18-BD07, GSL-18-C50) contain both apatite and titanite, whereas the remaining two samples each contain only one of the minerals (titanite in GSL-21-DS07; apatite in GSL-18-BD27). Apatite and titanite occur primarily in the matrix of each sample and are aligned with the foliation (Fig. 2a). One exception is GSL-21-DS07, in which there is extensive evidence of late fluid alteration and titanite occurs predominantly along late, coarse-grained quartz-epidote veins (Fig. 2b). Another exception is GSL-18-C50, which consists of a very fine-grained mylonitic matrix that wraps large clinozoisite–amphibole–titanite pseudomorphs after garnet (Dyck et al., 2021). Most apatite and titanite grains in the sample occur within the garnet pseudomorph and are aligned oblique to the matrix foliation.

South of the Laloche River fault, six samples (GSL-21-DS14, GSL-18-BD11, GSL-21-DS16, GSL-21-DS18, GSL-18-BD24, GSL-21-DS20) were collected from the southern structural domain of the shear zone while the remaining sample (GSL-21-BD12) was collected from a supracrustal unit in the Rutledge Group south of the shear zone (Fig. 1c). Except for GSL-21-DS14 (greenschist facies), all samples collected from the southern structural domain preserve epidote-amphibolite facies mineral assemblages. Furthermore, all six samples exhibit similar mineralogy and microstructure, with one of the six (GSL-18-BD11) identified as a mylonitic granodiorite and the remaining five as amphibole mylonitic granodiorites. The sample collected south of the shear zone (GSL-21-BD12) stands apart as an upper-amphibolite facies amphibole schist. All samples exhibit a strong, anastomosing foliation that is defined by the orientation of matrix-forming minerals, usually amphibole or biotite, and by the alignment of quartz ribbons and micaceous layers. Each of the seven samples contains both apatite and titanite, the grains of which occur primarily in the mylonitic matrix and are well-aligned with the foliation (Figs. 2c & d). One sample (GSL-21-DS16) contains two titanite populations, identified based on textural observations (Fig. 2e). The first population consists of sub- to anhedral titanite grains that are well-aligned with the foliation (referred to as "fabric-aligned titanite"), while the second consists of small, round titanite grains clustered together around long masses of ilmenite ("clustered titanite"). Several samples contain titanite grains that exhibit distinct core-rim structures (Fig. 2f).

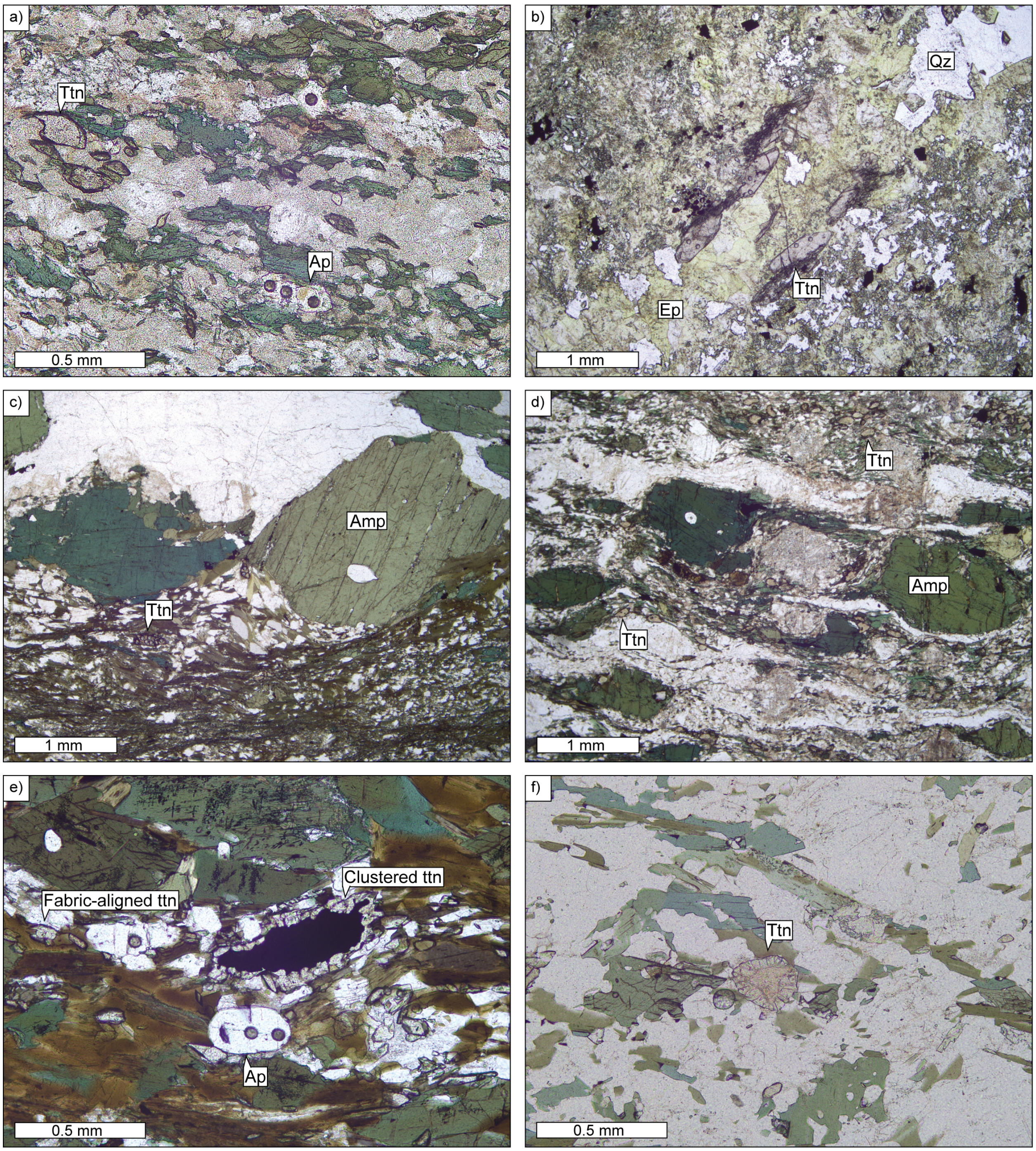


**Figure 2.** Summary of microstructural characteristics of apatite- and titanite-bearing samples. Mineral abbreviations follow Whitney and Evans (2010). (a) Well-aligned apatite and titanite

grains (GSL-18-BD07). (b) Titanite grains associated with late coarse-grained quartz-epidote vein (GSL-21-DS07). (c) Mylonitic fabric defined by fine-grained micaceous domains wrapping around amphibole porphyroclasts (GSL-21-DS14). (d) Well-developed foliation wrapping amphibole porphyroclasts (GSL-21-DS18). (e) Fabric-aligned and clustered titanite grains in GSL-21-DS16. (f) Core-rim structure visible in a titanite grain (GSL-18-BD24).

314 **Table 1.** Summary of apatite and titanite grain characteristics.

| Sample | Latitude (degrees) | Longitude (degrees) | Mineral | Grain characteristics | | | | |
|---|---|---|---|---|---|---|---|---|
| | | | | Occurrence | Relationship to fabric | Size (µm) | Shape | Zoning |
| GSL-18-BD07 | 61.643778 | -112.212944 | Ap | Matrix | Aligned | 50–100 | Sub- to anhedral | Patchy core-rim |
| | | | Ttn | Matrix | Aligned | 60–700 | Elongate, sub- to euhedral | Homogeneous or irregular patchy |
| GSL-21-DS07 | 61.646371 | -112.195418 | Ttn | Along qz-ep veins | Not aligned | 200–1000 | Euhedral | Oscillatory |
| GSL-18-BD27 | 61.630500 | -112.200944 | Ap | Matrix + inclusions in grt | Varies | 50–200 | Rounded, subhedral | Homogeneous |
| GSL-18-C50 | 61.629250 | -112.199889 | Ap | Within grt pseudomorph (+ matrix) | Oblique (+ aligned) | 50–400 | Anhedral, fractured | Patchy or core-rim |
| | | | Ttn | Within grt pseudomorph | Oblique | 100–800 | Rhombic | Patchy or oscillatory |
| GSL-21-DS14 | 61.647845 | -112.105861 | Ap | Matrix | Aligned | 60–500 | Elongate | Patchy |
| | | | Ttn | Matrix | Aligned | 50–200 | Subhedral | Core-rim |
| GSL-18-BD11 | 61.629250 | -112.167250 | Ap | Matrix | Aligned | 60–250 | Elongate, sub- to anhedral | Oscillatory or core-rim |
| | | | Ttn | Matrix, along micaceous layers | Aligned | 20–120 | Blocky | Homogeneous |

| | | | | | | | | |
|---|---|---|---|---|---|---|---|---|
| GSL-21-DS16 | 61.608126 | -112.137535 | Ap | Matrix, in amp-rich domains | Aligned | 80–250 | Rounded, elongate | Irregular core-rim |
| | | | Ttn | Fabric-aligned ttn: matrix | Aligned | 25–120 | Sub- to anhedral | Core-rim |
| | | | | Clustered ttn: surrounding masses of ilm | Not aligned | 25–120 | Elongate clusters of rounded grains | Core-rim |
| GSL-21-DS18 | 61.585146 | -112.177447 | Ap | Matrix | Aligned | 50–200 | Elongate, sub- to euhedral | Patchy, uncommon bright cores |
| | | | Ttn | Matrix, often with bt | Aligned | 50–350 | Elongate, sub- to anhedral | Irregular patchy |
| GSL-18-BD24 | 61.600083 | -112.089167 | Ap | Matrix | Aligned | 50–200 | Elongate, sub- to euhedral | Patchy, uncommon bright cores |
| | | | Ttn | Matrix | Aligned | 100–1500 | Sub- to anhedral | Core-rim |
| GSL-21-DS20 | 61.561525 | -112.139314 | Ap | Matrix | Aligned | 70–300 | Elongate, sub- to euhedral | Irregular oscillatory |
| | | | Ttn | Matrix, often with amp + bt | Aligned | 50–500 | Rhombic | Homogeneous |
| GSL-21-BD12 | 61.530367 | -112.034200 | Ap | Matrix + inclusions in amp | Varies | 50–200 | Anhedral | Patchy core-rim |
| | | | Ttn | Matrix | Aligned | 50–200 | Blocky to anhedral | Patchy core-rim |

**Note.** Samples are ordered geographically, NW to SE. Mineral abbreviations follow Whitney and Evans (2010).

4.2 Apatite U-Pb and trace element results

Tera-Wasserburg diagrams and representative REE profiles for all apatite populations are presented in Figures 3 and 4a, respectively. Detailed trace element plots as well as BSE and CL images of representative grains for all populations are presented in Figure S1 and full analytical results for all unknowns and reference materials are reported in Table S2. In the following text, unless otherwise specified, uncertainties reported refer to internal uncertainties only and do not reflect the externally reproducible uncertainties.

All apatite-bearing samples contain one main age population (Fig. 3). Lower intercept dates were calculated using the robust regression of Powell et al. (2020) for all populations and range from ca. 1920–1760 Ma. The oldest apatite populations are from samples collected north of the Laloche River fault and yield lower intercept dates of 1918 ± 10 Ma (GSL-18-C50; spine width [s] = 0.67) and 1915 ± 12 Ma (GSL-18-BD07; s = 0.57). The remainder of the apatite populations yield lower intercept dates between ca. 1860–1760 Ma.

Apatite spot analyses across all samples yield similar REE profiles with the main difference between analyses being the relative abundance of elements. Analyses that are classified as low-U analyses (<0.4 ppm) and that correspond to grains that disaggregated during ablation tend to exhibit the lowest overall concentrations of REE.

Four samples (GSL-18-BD27, GSL-21-DS14, GSL-21-DS18, GSL-21-DS20) exhibit depletion in Eu relative to Sm and Gd (Fig. 4a) with mean Eu/Eu* ranging from 0.15–0.60, the greatest of which is recorded in GSL-18-BD27 (mean Eu/Eu* = 0.15). There does not appear to be a correlation between Eu/Eu* and other REE ratios.

Three samples (GSL-18-BD27, GSL-18-C50, GSL-21-DS16) exhibit significant enrichment of LREE relative to HREE (Fig. 4a), with mean $La_n/Yb_n$ ranging from 16.79–17.76. Despite the similarities in relative LREE enrichment, these three samples exhibit distinct REE profiles. GSL-18-BD27 has a significant negative Eu anomaly, giving its REE profile a sawtooth appearance, while GSL-18-C50 and GSL-21-DS16 exhibit steadier decreases in REE concentration across their profiles, consistent with the overall enrichment of LREE relative to HREE observed (Fig. 4a). Five samples (GSL-18-BD07, GSL-21-DS18, GSL-18-BD24, GSL-21-DS20, GSL- 21-BD12) also exhibit enrichment of LREE relative to HREE (Fig. 4a), but record slightly lower mean $La_n/Yb_n$, with values ranging from 2.06–9.20. Meanwhile, the two remaining samples (GSL-21-DS14, GSL-18-BD11) exhibit an overall depletion of LREE relative to HREE (Fig. 4a), with mean $La_n/Yb_n$ of 0.45 and 0.49, respectively.

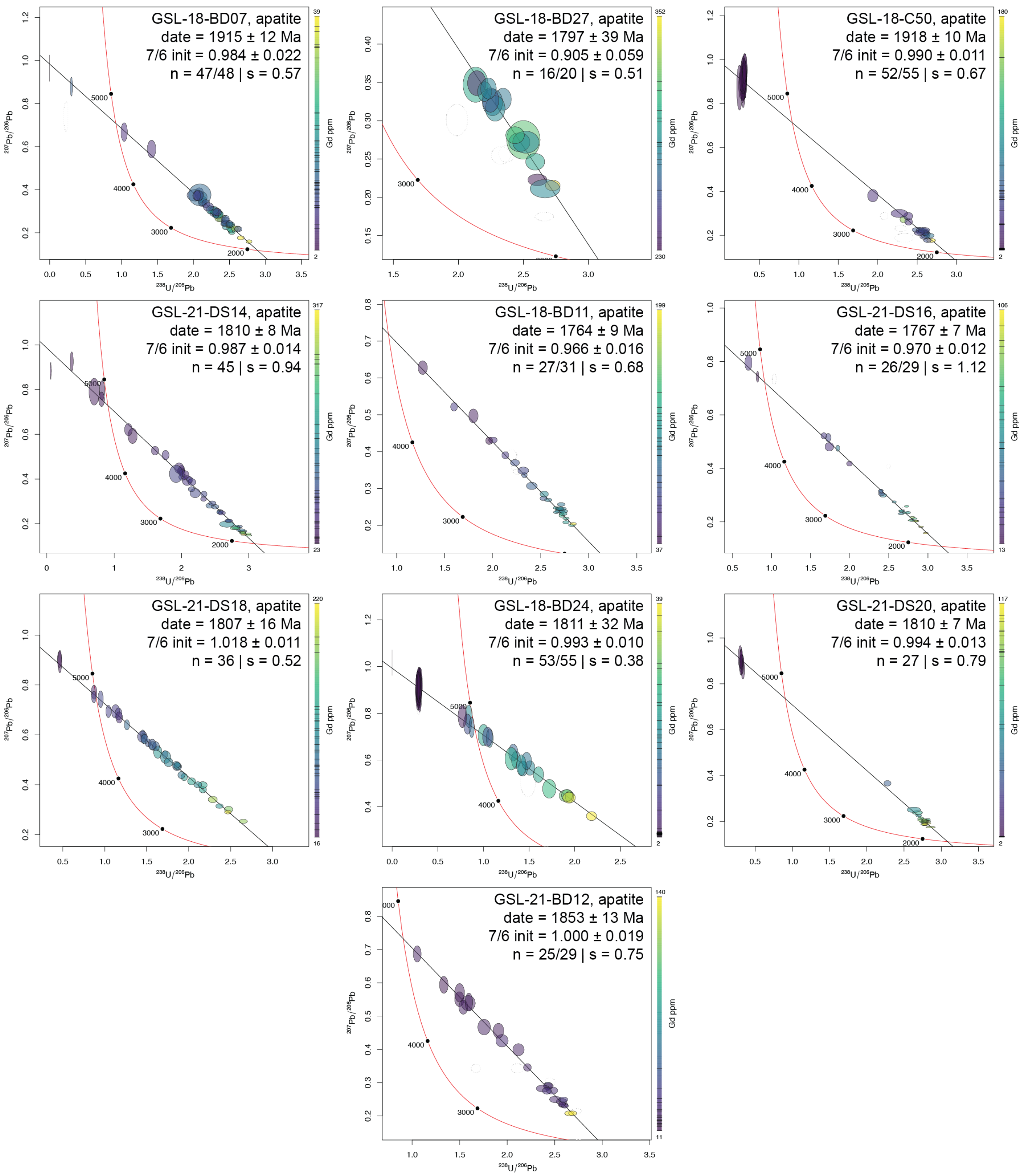


**Figure 3.** Tera-Wasserburg diagrams for each apatite population, constructed using ChrontouR (Larson, 2022). 7/6 init – initial $^{207}Pb/^{206}Pb$ ratio.

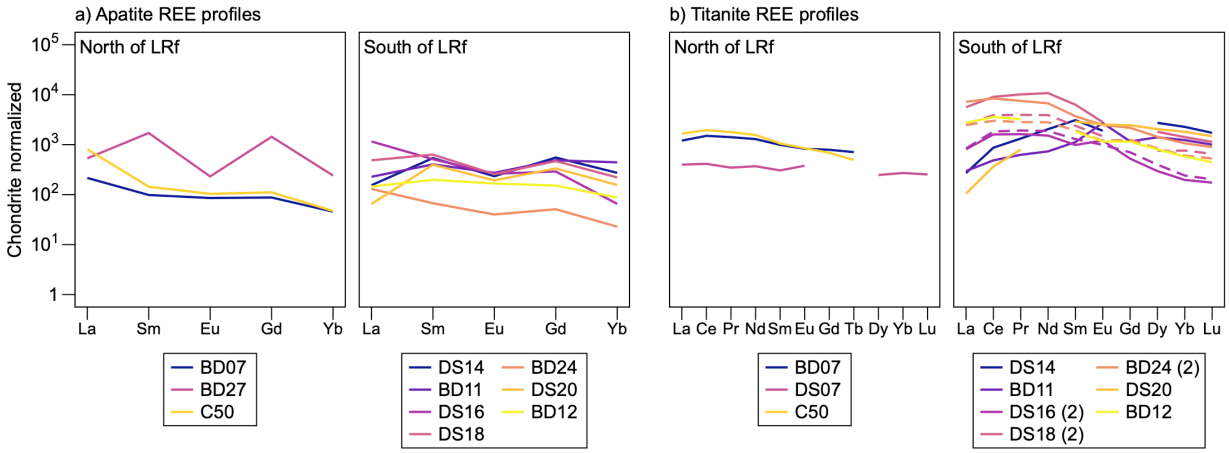


**Figure 4.** Average REE profiles for all apatite (a) and titanite (b) populations. All samples contain one population of each mineral, except for DS16, DS18, and BD24, which each contain two titanite populations; dashed lines indicate secondary populations (clustered titanite in DS16; BSE-dark titanite in DS18, BD24). LRf – Laloche River fault.

### 4.3 Titanite U-Pb and trace element results

Tera-Wasserburg diagrams and representative REE profiles for all titanite populations are presented in Figures 5 and 4b, respectively. Detailed trace element plots and BSE images of representative grains for all populations are presented in Figure S2 and full analytical results for all unknowns and reference materials are reported in Table S3. As with the apatite data, unless otherwise specified, uncertainties reported in-text refer to internal uncertainties only.

With the exceptions of GSL-18-BD24, GSL-21-DS16, and GSL-21-DS18, which each contain two distinct populations characterized by differences in grain morphology and trace element profiles, most titanite-bearing samples contain one main age population (Fig. 5). Lower intercept dates were calculated for all populations and range from ca. 1910–1740 Ma across the shear zone. The oldest titanite populations yield lower intercept dates of 1904 ± 9 Ma (GSL-18-BD07; s = 1.19) and 1888 ± 11 Ma (GSL-18-C50; s = 1.27) and occur in the same two samples that have the oldest apatite populations. Meanwhile, the youngest titanite populations are from samples collected south of the Laloche River fault and yield lower intercept dates of 1740 ± 9 Ma (GSL-21-DS14; s = 0.90) and 1768 ± 9 Ma (clustered titanite in GSL-21-DS16; s = 1.11). The remainder of the lower intercept dates fall between ca. 1870–1790 Ma.

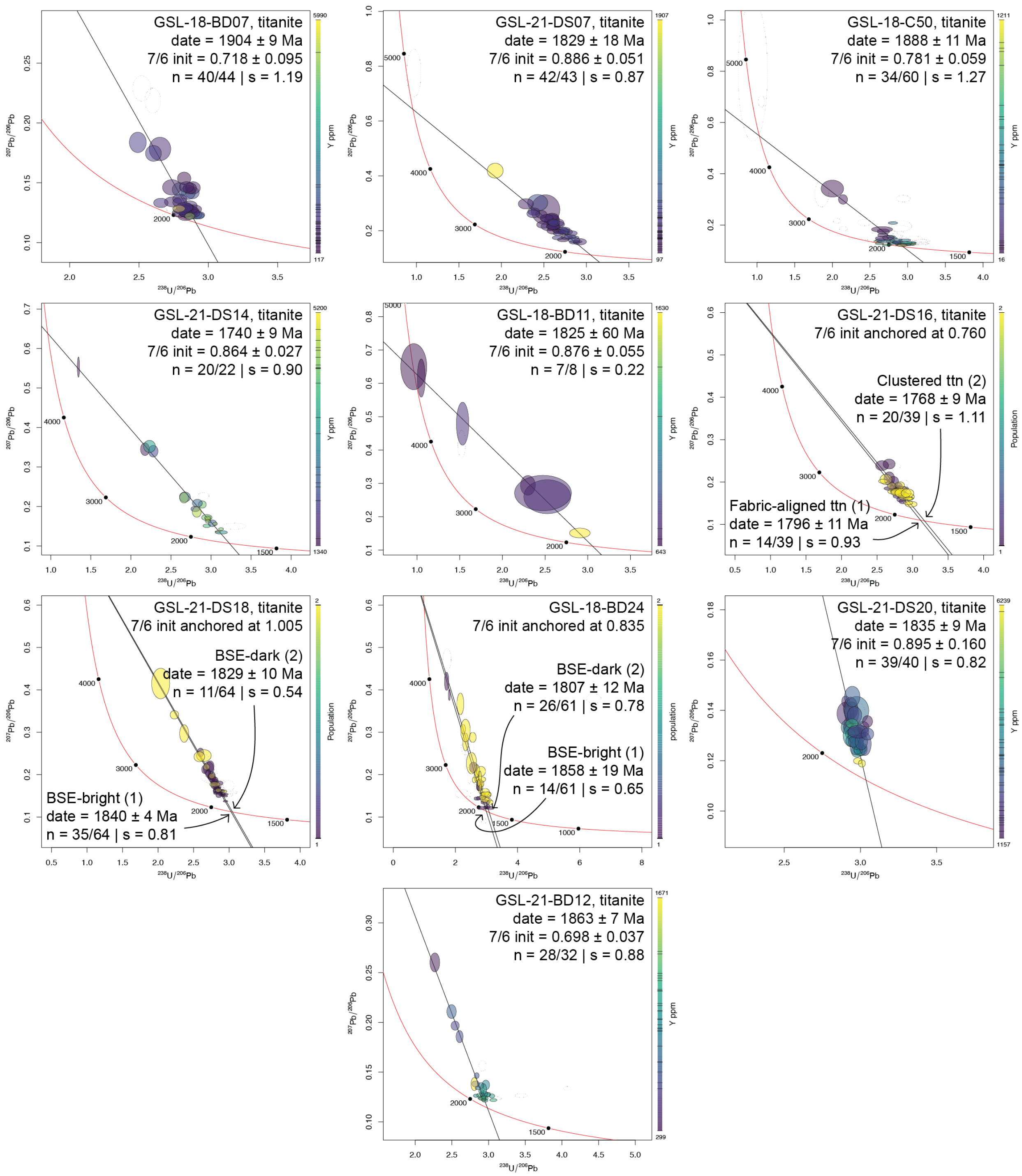


**Figure 5.** Tera-Wasserburg diagrams for each titanite population, constructed using ChrontouR (Larson, 2022). 7/6 init – initial $^{207}Pb/^{206}Pb$ ratio.

Most analyses within individual samples have similar REE profiles with the main difference between analyses being the relative abundance of elements. Seven populations (GSL-21-BD12, two in GSL-18-BD24, two in GSL-21-DS16, two in GSL-21-DS18) exhibit strikingly similar concave-down REE profiles that show an overall enrichment in LREE relative to HREE

(Fig. 4b). These samples record mean $La_n/Lu_n$ ranging from 4.24–8.67. All seven populations exhibit little to no enrichment of LREE relative to MREE, with mean $La_n/Sm_n$ ranging from 0.67–2.11; however, all seven populations show enrichment of MREE relative to HREE, with mean $Sm_n/Lu_n$ ranging from 3.37–6.34. Three additional samples (GSL-21-DS14, GSL-18-BD11, GSL-21-DS20) also have concave-down REE profiles but show an overall depletion in LREE relative to HREE (Fig. 4b), with mean $La_n/Lu_n$ ranging from 0.08–0.38. All three further exhibit a depletion in LREE relative to MREE, with mean $La_n/Sm_n$ ranging from 0.04–0.43, as well as a relatively low enrichment of MREE relative to HREE, with mean $Sm_n/Lu_n$ ranging from 1.04–1.90. One sample (GSL-21-DS07) has a relatively flat REE profile compared to the others (Fig. 4b), with a mean $La_n/Lu_n$ of 1.71. The mean $La_n/Sm_n$ and $Sm_n/Lu_n$ are similarly stable, with values of 1.43 and 1.23.

The REE profiles for the distinct age populations in GSL-18-BD24, GSL-21-DS16, and GSL-21-DS18 differ. In GSL-21-DS16, most of the analyses from the fabric-aligned titanite population exhibit enrichment in Eu relative to Sm and Gd, whereas there is no enrichment in Eu in the analyses from the clustered titanite population (Fig. 4b). In GSL-18-BD24 and GSL-21-DS18, the BSE-bright and BSE-dark populations exhibit similar overall patterns in REE profiles, however, the BSE-dark analyses typically record lower REE concentrations than the analyses from BSE-bright domains (Fig. 4b). For example, Sm concentrations in GSL-18-BD24 range from 271–932 ppm (BSE-bright) compared with 49–606 ppm (BSE-dark), while in GSL-21-DS18, they range from 328–1384 ppm (BSE-bright) compared with 146–812 ppm (BSE-dark).

### 4.4 Zr-in-titanite thermometry

Zr-in-titanite temperatures were calculated for each of the titanite analyses following the steps outlined by Hayden et al. (2008). Mean and median temperatures were calculated for each titanite population. Mean temperatures are used for comparison between populations. A box-and-whisker plot of temperatures calculated for each titanite population is presented in Figure 6 and full results are reported in Table S4. Titanite records temperatures ranging from approximately 630–950 °C across all samples. Mean temperatures calculated for each of the thirteen titanite populations range from 674 ± 20 °C (GSL-21-DS07) up to 768 ± 20 °C (GSL-18-C50).

## 5 Discussion

### 5.1 A temporal record of dynamic (re)crystallization

The lower intercept dates recorded by all apatite and titanite populations are plotted in Figure 6 according to sample position along the transect of the study area. The apatite and titanite chronometers yield overlapping ranges of dates across the shear zone, spanning from ca. 1920–1760 Ma and ca. 1910–1740 Ma, respectively. The range of dates recorded by both chronometers post-date prograde-to-peak metamorphism in the shear zone as recorded by two garnet Lu-Hf ages of 1931 ± 12 and 1917 ± 6 Ma and overlapping zircon and monazite ages (ca. 1933–1913 Ma; Cutts & Dyck, 2022). Furthermore, the dates yielded by apatite and titanite south of the Laloche River fault (ca. 1860–1760 and ca. 1870–1740 Ma, respectively) post-date the crystallization of plutonic host rocks within the shear zone (> 1930 Ma; Cutts et al., 2022). Together, these relationships indicate that the populations both north and south of the Laloche River fault are unlikely to represent either a primary igneous or prograde metamorphic origin.

Both chronometers record older dates on the north side of the Laloche River fault (Fig. 6) with the oldest apatite and titanite dates occurring in the same two samples: GSL-18-BD07 (apatite 1915 ± 12 Ma; titanite 1904 ± 9 Ma) and GSl-18-C50 (apatite 1918 ± 10 Ma; titanite 1888 ± 11 Ma). Moreover, both chronometers demonstrate an overall younging trend toward the fault in the southern structural domain (Fig. 6). A similar pattern is also reflected in Zr-in-titanite temperatures, which exhibit an overall decrease from south of the study area towards the Laloche River fault (Fig. 6).

In all but three populations (GSL-21-BD27, GSL-21-DS07, clustered titanite in GSL-21-DS16), apatite and titanite grains have a shape-preferred orientation that is aligned with ductile shear fabrics (Figs. 2a, c & d). Considering these textural observations in conjunction with the timing and nature of apatite and titanite (re)crystallization in the shear zone, we interpret the apatite and titanite dates as recording syn-kinematic (re)crystallization, which encompasses both dynamic recrystallization of, or re-equilibration of the U-Pb system in, pre-existing apatite and titanite as well as syn-tectonic growth of new grains. It is possible that the apatite and titanite grains that are aligned with shear planes do not record the timing of the shear process (i.e., they record pre-shear (re)crystallization processes), however, given that the apatite and titanite data are significantly younger than prograde-to-peak metamorphism as outlined above, it is unlikely that these chronometers are recording earlier magmatic or metamorphic events. Moreover, given that apatite and titanite dates at similar structural positions typically overlap, we consider it unlikely that they are cooling ages. Apatite has a nominal closure temperature (in the sense of Dodson, 1973) of ~425–530 ˚C (Chamberlain & Bowring, 2001; Cherniak et al., 1991) whereas recent estimates for titanite closure temperatures are much higher in excess of 700 ˚C (Gao et al., 2012; Kohn, 2017; Kohn & Corrie, 2011; Spencer et al., 2013; Stearns et al., 2015).

While most of the apatite and titanite populations are interpreted to record the timing of ductile shear, two titanite populations (GSL-21-DS07, clustered titanite in GSL-21-DS16) and one apatite population (GSL-18-BD27) exhibit distinct textural and geochemical characteristics that require additional explanation. Titanite grains in GSL-21-DS07 occur predominantly along late coarse-grained quartz-epidote veins (Fig. 2b) and exhibit oscillatory zoning in BSE (Fig S2b). Titanite also occurs in the heavily altered matrix of the sample. These grains display resorption textures and exhibit irregular, patchy zoning (Fig. S2b), which we interpret as textural evidence of fluid alteration. Analyses from the quartz-epidote vein-hosted grains yield flat REE profiles that are distinct from all other titanite populations (Fig. 4b). The lack of enrichment or depletion in any of the REE is consistent with titanite (re)crystallization occurring in a relatively isolated system, away from the presence of other REE-bearing minerals (e.g., allanite, garnet; Garber et al., 2017). This observation is consistent with the interpretation that titanite in this sample (re)crystallized due to the fluid infiltration that resulted in the formation of quartz-epidote veins. Meanwhile, the clustered titanite in GSL-21-DS16 are differentiated from the fabric-aligned titanite in this sample by the absence of a strong positive Eu anomaly in their geochemical signature (Fig. 4b). The positive Eu anomaly exhibited by the fabric-aligned titanite is interpreted as indicating (re)crystallization coeval with plagioclase breakdown (e.g., Garber et al., 2017). Given the geochemical differences between the two populations and the lack of alignment of the clustered titanite with the mylonitic fabric (Fig. 2e), we interpret the clustered titanite as reflecting post-kinematic (re)crystallization in a plagioclase-free environment. Finally, the apatite population in GSL-18-BD27 yields a distinct REE profile with an overall enrichment in REE and a pronounced negative Eu anomaly (Fig. 4a). These geochemical characteristics have been previously interpreted to reflect hydrothermal alteration of apatite (e.g., Adlakha et al., 2018), and while the specific effects of a fluid on apatite REE chemistry may vary between localities, various studies have demonstrated the sensitivity of apatite trace element systematics to hydrothermal activity (e.g., Bouzari et al., 2016; Mao et al., 2016; Ribeiro et al., 2020). Furthermore, although apatite in this sample occurs both in the matrix and as inclusions in garnet, both types of apatite record matching REE signatures (Fig. 4a), which is consistent with all apatite grains re-equilibrating with a fluid.

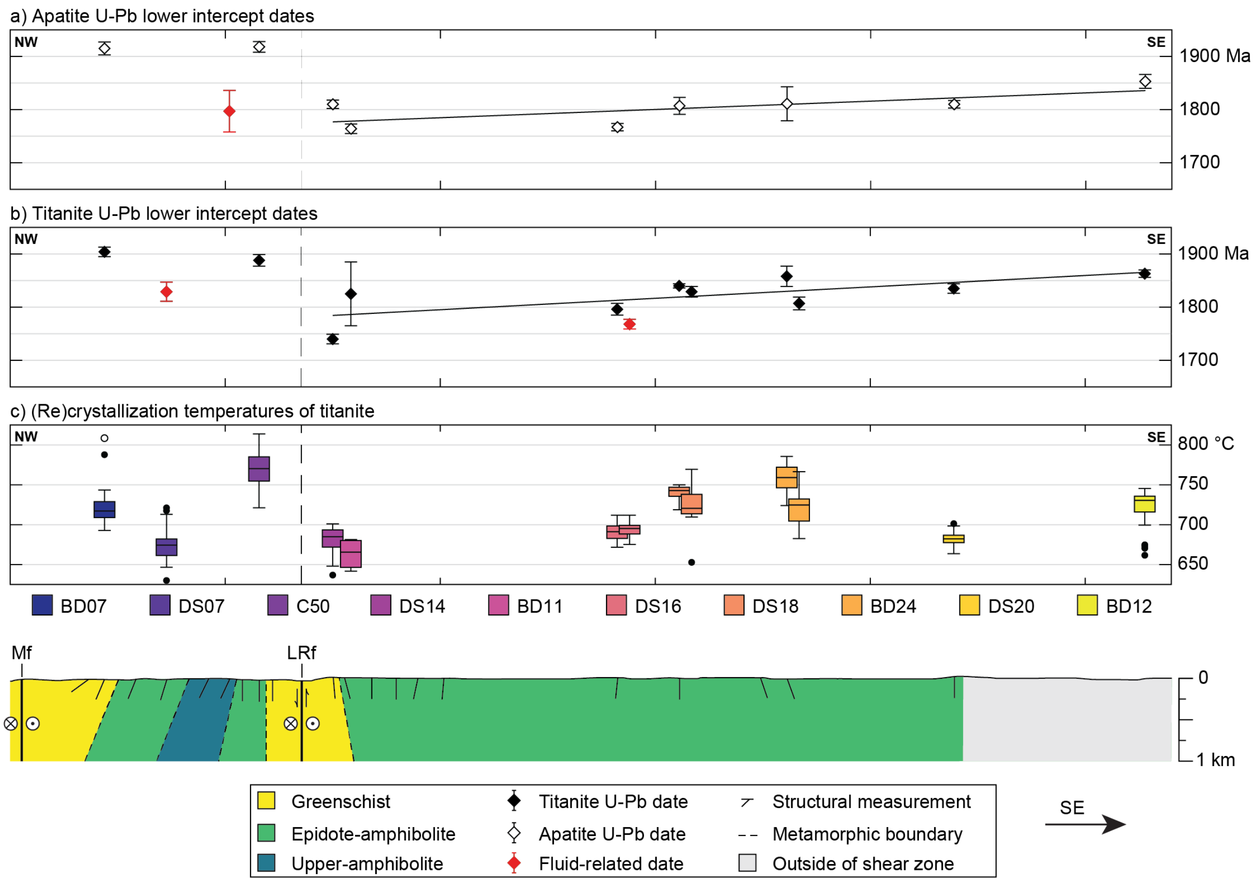


**Figure 6.** Summary of petrochronology results plotted along the transect of the study area (Fig. 1c). The McDonald fault (Mf) and the Laloche River fault (LRf) are marked and the position of the Laloche River fault is indicated on the plots by a dashed line. The horizontal position of each marker corresponds to its approximate position along the transect. (a) Lower intercept dates of apatite with 2σ error bars. A linear fit to the data in the southern structural domain indicates a faultward younging trend. (b) Lower intercept dates of titanite with 2σ error bars. A linear fit to the data in the southern structural domain (excluding clustered titanite in GSL-21-DS16) indicates a faultward younging trend. (c) Box and whisker plot of the titanite (re)crystallization temperatures, calculated using the geothermometer of Hayden et al. (2008). Outliers are indicated by solid and open circles, which correspond to values larger than 1.5 and 3x the interquartile range, respectively.

### 5.2 Architecture and temporal evolution of the GSLsz

Figure 7 presents a simplified model of the GSLsz. This model builds on basic Sibson-Scholz shear zone models, which consist of a zone of active deformation that is narrow near the surface and broadens with depth, giving it a characteristic triangular shape (Scholz, 1988). In the upper crust, deformation is dominated by brittle processes and strain is localized along one or more discrete fault surfaces, whereas in the middle to lower crust, there is a gradual transition from brittle to ductile processes and strain is distributed across a broadening zone of deformation. One key prediction of the Sibson-Scholz model is the overprinting of higher-grade metamorphic mineral assemblages by lower-grade ones, which is observed in all units of the GSLsz. This overprinting is the result of the crust being exhumed and consequently experiencing decreases in both pressure and temperature, reflected by changes in the stable mineral assemblage. Because the metamorphic conditions preserved at the surface level of the GSLsz reflect the lowest-grade mineral assemblages associated with ductile fabrics, the observed metamorphic grade can be used to estimate depth at which a package of crustal material exited the zone of active shear.

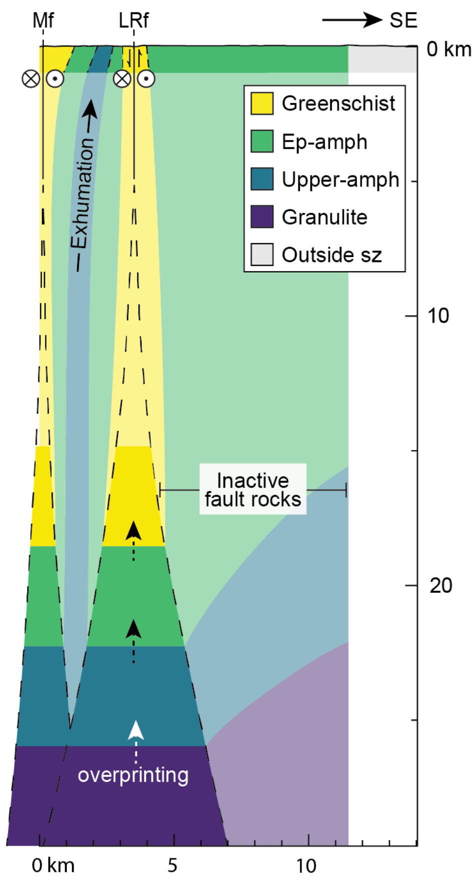


**Figure 7.** Two-strand shear zone model proposed for the GSLsz. The McDonald fault (Mf) and the Laloche River fault (LRf) are marked. The zones of active deformation are outlined by dashed lines. Gs refers to greenschist facies, Ep-amph to epidote-amphibolite facies, and upper-amph to upper-amphibolite facies.

Our simplified model of the GSLsz adopts the peak thermal gradient of ~1000 °C/GPa reported by Dyck et al. (2021), which is based on petrological modelling of units from the northern structural domain. Using this thermal gradient, the depths corresponding to key thermal boundaries between metamorphic facies are estimated by assuming an average overburden density of 2750 kg/m$^3$. The following thermal boundaries are assumed: (1) greenschist facies corresponds to the temperature range of 400–500 °C, (2) epidote-amphibolite facies to 500–600 °C, (3) upper-amphibolite facies to 600–700 °C, and (4) granulite facies to 700–800 °C (Palin & Dyck, 2021). The depths calculated for the thermal boundaries are used to define the vertical extent of metamorphic layers in the shear zone.

Based on the observed symmetry of the metamorphic units exposed between the McDonald and Laloche River faults, we propose that the GSLsz initially had two simultaneously active strands of deformation, with one centered on the McDonald fault and the other centered on the Laloche River fault (Fig. 7). As the width of the actively deforming region narrowed structurally upward, a symmetrical pattern would have developed with respect to the most recent recorded conditions of metamorphism and shear-(re)crystallization. The two greenschist facies belts and neighboring epidote-amphibolite rocks that are centered on the McDonald and Laloche River faults are consistent with progressive localization of strain along these structures.

Figure 8 presents a kinematic model for the GSLsz that builds on the two-strand model presented in Figure 7. By using the apatite ages as a record of the time at which a sample exited the actively deforming shear zone (and stopped (re)crystallizing), we estimate both the position and width of the zones of active deformation over time. We propose three main stages for the temporal evolution of the GSLsz (Fig. 8). In stage 1 (ca. 1920–1880 Ma), there are two strands of active deformation centered on the McDonald and Laloche River faults. In stage 2 (ca. 1880–1800 Ma), ductile deformation associated with the McDonald fault ceases and the locus of deformation shifts southwards towards the Laloche River fault and one (or more) parallel strands operating to the south of the Laloche River fault. During stage 3 (ca. 1800–1740 Ma), the active deformation south of the Laloche River fault migrates northward, leaving no lower-grade brittle record to the south of the fault. From the lack of variability in metamorphic grade on the south side of the Laloche River fault, we interpret that the localization of shear along the fault occurred while the now present-day surface was 15–20 km deep, and still below the base of the seismogenic crust.

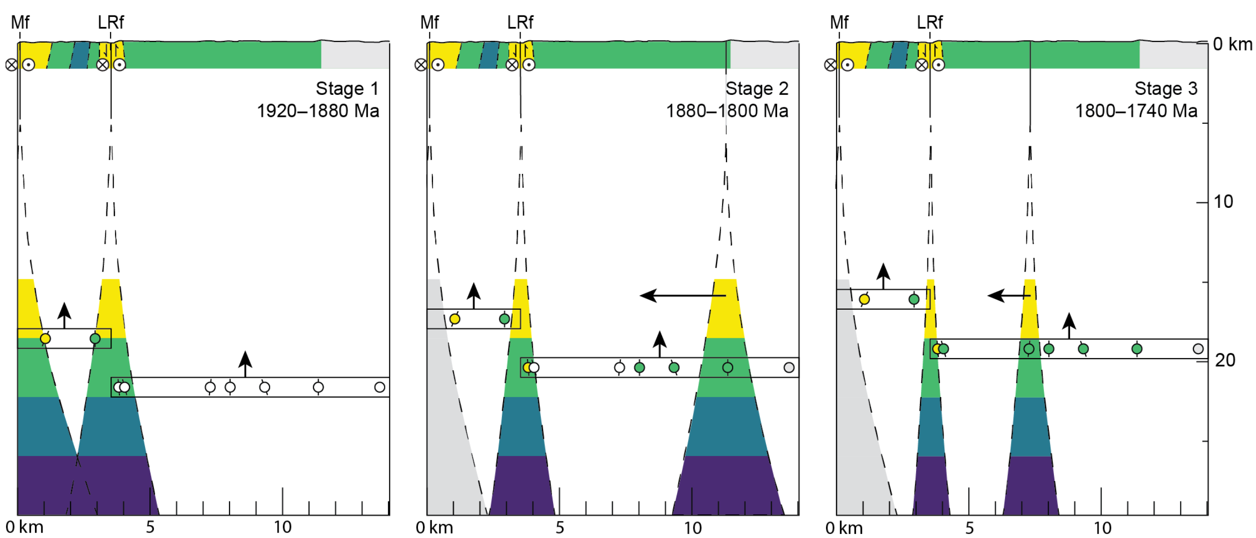


**Figure 8.** Tectonic model for the GSLsz. Colors correspond to metamorphic facies: yellow to greenschist, green to epidote-amphibolite, blue to upper-amphibolite, purple to granulite. A thermal gradient of 1000 °C/GPa is assumed for all stages. Apatite samples are indicated by circles. Colored circles indicate samples that have exited the actively deforming shear zone by

the end of each stage. Arrows illustrate the exhumation of crustal layers as well as the lateral migration of the actively deforming strands over time. The McDonald fault (Mf) and Laloche River fault (LRf) are marked in each panel.

Our kinematic model (Fig. 8) involves a broad width of crust that was last deformed under epidote-amphibolite facies conditions. The active shear zone may have significantly widened when the stress that was originally accommodated by the McDonald fault is transferred southwards into the Rae craton. The Rae cratonic margin would have been relatively young at the time when the GSLsz was developed with voluminous Talston age (1.99–1.92 Ga) plutonism making up the bulk of the leading edge of the craton. It is possible that the (then) recent magmatism would contribute to an elevated crustal thermal gradient and a less-competent Rae margin. Along similar lines, the higher peak-metamorphic conditions and crustal thickening recorded in the northern domain may have led to a dehydrated and more competent Slave margin.

Over the span of 50 to 100 Myr, it is possible that an actively deforming strand shifted laterally by up to 10 km. In our model, the loci of shear shifted back towards the Laloche River fault and the McDonald fault upon exhumation. Therefore, the only evidence of localized, low-grade deformation has been lost due to the erosion of the upper-crustal expressions of these structures. The migration of the actively deforming strands over time does not change the interpretation that the strands decrease in width and range over time.

The presence of multiple active strands within major shear zones, as well as the lateral migration of these actively deforming strands, has been documented in modern-day analogues. The Karakoram fault zone in southwestern Tibet is known to have had several active fault strands throughout its history with varying amounts of slip occurring along each of these structures (e.g., Searle, 1996; Dunlap et al., 1998; Phillips et al., 2004). The North Anatolian fault zone in Turkey provides another example of a major strike-slip fault system consisting of multiple active branches (e.g., Okay et al., 1999; Hejl et al., 2010). Yet another well-known example would be the San Andreas fault system, which consists of over a dozen faults that all record distinct but often overlapping slip histories (e.g., Scharer and Streig, 2019). Each of these major transform systems yields extensive evidence of seismic activity along both main and subsidiary structures, a phenomenon that likely applied to the GSLsz as well.

Our model highlights several key observations, including the discrepancy in ages recorded across the Laloche River fault (Fig. 8). We posit that the Laloche River fault represents a much more significant tectonic boundary than previously thought. Both the apatite and titanite chronometers record significantly older ages of dynamic (re)crystallization on the north side of the Laloche River fault, while on the south side of the fault, they record younger ages that define a younging trend towards the centre of the shear zone. There may be several contributing factors that explain the age and depth discrepancy recorded across the fault, including: 1) a component of dip-slip motion along the Laloche River fault, resulting in the vertical juxtaposition of units of different ages; 2) the Laloche River fault represents a major tectonic boundary with inherent differences in rheology; and 3) there was an increased crustal thermal gradient in the southern structural domain at the time of deformation.

If the first explanation for the age discrepancy holds true, then the age difference recorded across the Laloche River fault could be the result of a north side-down component of dip-slip motion along the fault. Hanmer (1988) and Dyck et al. (2021) report evidence of a shallow north side-down dip-slip component along the Laloche River fault, including mineral lineations and slickenlines along splay fault surfaces. Using the estimates of sample depth from the kinematic model, approximately 2–5 km of dip-slip motion would be required to bring all the samples to the same structural level.

The second explanation for the age discrepancy, which is that the Laloche River fault represents the suture between the Rae and Slave cratons, assumes a difference in crustal affinity across the boundary. This interpretation is consistent with lithological differences found across the shear zone. Recent work focusing on the plutonic rocks hosting the GSLsz has revealed distinct geochemical and geochronological signatures in zircon on either side of the Laloche River fault (Cutts et al., 2022). To the north of the fault, zircon preserve Archean ages and mantle oxygen isotope compositions, while to the south, they are Proterozoic in age and preserve heavier oxygen isotope compositions (Cutts et al., 2022). Additionally, mylonitic rocks on the south side of the Laloche River fault appear to reflect a broadly homogeneous deformation event, with minimal variation in the developed resultant textures and mineral assemblages, while those found north of the Laloche River fault preserve broad ranges in degree of mylonitization as well as metamorphic conditions, which extend up to granulite facies. There is a notable lack of evidence for high-pressure (>1 GPa), migmatization, and granulite facies metamorphism to the south of the fault (Dyck et al., 2021). Another key difference across the Laloche River fault is the presence of metasedimentary lithologies to the north of the fault, whereas none have been documented on the south side, indicating contrasting lithotectonic architectures. Together, these lines of evidence point to a difference in crustal affinity across the Laloche River fault consistent with the Laloche River fault representing the suture between the Rae and Slave cratons.

The third explanation for the age discrepancy involves a difference in crustal thermal gradient across the Laloche River fault. A modest increase in the thermal gradient of the southern structural domain, from 1000 to ~1100 °C/GPa, would reconcile the apparent differences in recrystallization depths at any given time. With the younger ages found only to south of the fault, there is no need for a step-change in temperatures across the fault. Instead, the entire shear zone could have experienced heating as it matured.

Considering the apatite and titanite ages in the context of the Rae-Slave suture, we interpret the older ages on the north side of the suture as recording the initial stages of strike-slip deformation related to the oblique collision between the Rae and Slave cratons. We interpret the ages on the south side of the suture as the broad-scale deformational response of the western Rae cratonic margin to the convergence and subsequent transform motion along the cratonic boundary. As there are no younger ages related to ductile deformation on the north side of the suture, the Slave craton likely remained relatively stable and rigid following its response to the initial collision, whereas the younger and weaker Rae cratonic margin continued to accommodate the bulk of the deformation related to the convergence.

## 6 Conclusions

We present *in situ* U-Pb geochronology results for the shear-induced (re)crystallization of apatite and titanite, which yield new information on the timing and duration of ductile deformation along the GSLsz and record a near-continuous history of ductile shear spanning ca. 1920–1740 Ma. Based on the integration of this new geochronological data with structural and metamorphic observations across the structure, we propose a time-dependent kinematic model for the GSLsz that involves three stages of evolution. During stage 1 (ca. 1920–1880 Ma), ductile shear is localized along two strands of active deformation in the northern structural domain, centered on the McDonald and Laloche River faults. Stage 2 (ca. 1880–1800 Ma) involves the cessation of shear along the McDonald fault and the migration of the locus of deformation into the southern structural domain. Finally, during stage 3 (ca. 1800–1740 Ma), deformation localizes back along the Laloche River fault. These interpretations reveal further complexities in the case of the GSLsz, including the posited presence of the Slave-Rae suture along the Laloche River fault, as supported by other lithological and geochemical work, and the significance of the lateral migration of the zone of active deformation in major crustal shear zones. Our results illustrate the necessity of providing structural and metamorphic context for geochronological data to accurately constrain the evolution of crustal-scale structures and we believe that the approach outlined here is widely applicable to other continental transform systems.

## Acknowledgments

We respectfully acknowledge the unceded traditional territories of the Dene peoples, including the Łútsël K'é (Lutsel K'e) and the Deninu Kų́ę́ (Deninu Kue) First Nations, on which we conducted fieldwork. We thank Mark Button, Sudip Shrestha and Dan Gibson for their technical support and Alix Osinchuk and Rebecca Canam for fieldwork support. Funding for this study was provided by a Natural Sciences and Engineering Research Council (NSERC) graduate scholarship awarded to DS, a NSERC Discovery Grant awarded to BD, as well as support from Natural Resource Canada's Polar Continental Shelf and GEM Geoscience programs.

## Open Research

All U-Pb isotope and trace element data used in this manuscript are available in Supplementary Tables S2–S4 and are also available from the Open Science Framework online repository via https://doi.org/10.17605/OSF.IO/WP3XQ (Šilerová et al., 2022).

## References

Adlakha, E., Hanley, J., Falck, H., & Boucher, B. (2018). The origin of mineralizing hydrothermal fluids recorded in apatite chemistry at the Cantung W–Cu skarn deposit, NWT, Canada. *European Journal of Mineralogy*, *30*(6), 1095–1113. https://doi.org/10.1127/ejm/2018/0030-2780

Apen, F. E., Wall, C. J., Cottle, J. M., Schmitz, M. D., Kylander-Clark, A. R. C., & Seward, G. G. E. (2022). Apatites for destruction: Reference apatites from Morocco and Brazil for U-Pb petrochronology and Nd and Sr isotope geochemistry. *Chemical Geology*, *590*, 120689. https://doi.org/10.1016/j.chemgeo.2021.120689

Berman, R. G., Davis, W. J., Sanborn-Barrie, M., Whalen, J. B., Taylor, B. E., McMartin, I., McCurdy, M. W., Mitchell, R. K., Ma, S., Coyle, M., Roberts, B., & Craven, J. A. (2018). Report of activities for the GEM-2 Chantrey-Thelon activity: Thelon Tectonic Zone project, Nunavut. *Geological Survey of Canada*. https://doi.org/10.4095/306622

Bethune, K. M., Berman, R. G., Rayner, N., & Ashton, K. E. (2013). Structural, petrological and U–Pb SHRIMP geochronological study of the western Beaverlodge domain: Implications for crustal architecture, multi-stage orogenesis and the extent of the Taltson orogen in the

SW Rae craton, Canadian Shield. *Precambrian Research*, *232*, 89–118. https://doi.org/10.1016/j.precamres.2013.01.001

Bostock, H. H., & Loveridge, W. D. (1988). Geochronology of the Taltson Magmatic Zone and its eastern cratonic margin, District of Mackenzie. *Radiogenic Age and Isotopic Studies: Report 2; Geological Survey of Canada, Paper no. 88-2*, 59–65. https://doi.org/10.4095/126603

Bostock, H. H., van Breemen, O., & Loveridge, W. D. (1987). Proterozoic geochronology in the Taltson Magmatic Zone, N.W.T. *Radiogenic Age and Isotopic Studies: Report 1; Geological Survey of Canada, Paper no. 87-2*, 73–80. https://doi.org/10.4095/122751

Bostock, H. H., van Breemen, O., & Loveridge, W. D. (1991). Further geochronology of plutonic rocks in northern Taltson Magmatic Zone, District of Mackenzie, N.W.T. *Radiogenic Age and Isotopic Studies: Report 4; Geological Survey of Canada, Paper no. 90-2*, 67–78. https://doi.org/10.4095/131938

Bouzari, F., Hart, C. J. R., Bissig, T., & Barker, S. (2016). Hydrothermal alteration revealed by apatite luminescence and chemistry: A potential indicator mineral for exploring covered porphyry copper deposits. *Economic Geology*, *111*(6), 1397–1410. https://doi.org/10.2113/econgeo.111.6.1397

Bowring, S. A., Schmus, W. R. V., & Hoffman, P. F. (1984). U–Pb zircon ages from Athapuscow aulacogen, East Arm of Great Slave Lake, N.W.T., Canada. *Canadian Journal of Earth Sciences*, *21*(11), 1315–1324. https://doi.org/10.1139/e84-136

Cawood, T. K., & Platt, J. P. (2021). What controls the width of ductile shear zones? *Tectonophysics*, *816*, 229033. https://doi.org/10.1016/j.tecto.2021.229033

Chacko, T., De, S. K., Creaser, R. A., & Muehlenbachs, K. (2000). Tectonic setting of the Taltson magmatic zone at 1.9–2.0–Ga: A granitoid-based perspective. *Canadian Journal of Earth Sciences*, *37*(11), 1597–1609. https://doi.org/10.1139/e00-029

Chamberlain, K. R., & Bowring, S. A. (2001). Apatite–feldspar U–Pb thermochronometer: A reliable, mid-range (~450°C), diffusion-controlled system. *Chemical Geology*, *172*(1), 173–200. https://doi.org/10.1016/S0009-2541(00)00242-4

Cherniak, D. J., Lanford, W. A., & Ryerson, F. J. (1991). Lead diffusion in apatite and zircon using ion implantation and Rutherford Backscattering techniques. *Geochimica et Cosmochimica Acta*, *55*(6), 1663–1673. https://doi.org/10.1016/0016-7037(91)90137-T

Cutts, J. A., Dyck, B., Davies, J., & Stern, R. (2022). Tectonic setting and provenance of plutonic rocks hosting the Great Slave Lake shear zone from microanalytical zircon U-Pb geochronology and oxygen and hafnium isotopes. *GAC-MAC-IAH-CNC-CSPG 2022 Halifax Meeting: Abstracts*, *45*, 94. https://doi.org/10.12789/geocanj.2022.49.188

Cutts, J. A., & Dyck, B. (2022). Incipient collision of the Rae and Slave cratons at ca. 1.95 Ga. *GSA Bulletin*. https://doi.org/10.1130/B36393.1

Dunlap, W. J., Weinberg, R. F., & Searle, M. P. (1998). Karakoram fault zone rocks cool in two phases. *Journal of the Geological Society*, *155*(6), 903–912. https://doi.org/10.1144/gsjgs.155.6.0903

Dyck, B., Goddard, R. M., Wallis, D., Hansen, L. N., & Martel, E. (2021). Metamorphic evolution of the Great Slave Lake shear zone. *Journal of Metamorphic Geology*, *39*(5), 567–590. https://doi.org/10.1111/jmg.12576

Fisher, C. M., Bauer, A. M., Luo, Y., Sarkar, C., Hanchar, J. M., Vervoort, J. D., Tapster, S. R., Horstwood, M., & Pearson, D. G. (2020). Laser ablation split-stream analysis of the Sm-Nd and U-Pb isotope compositions of monazite, titanite, and apatite – Improvements, potential reference materials, and application to the Archean Saglek Block gneisses. *Chemical Geology*, *539*, 119493. https://doi.org/10.1016/j.chemgeo.2020.119493

Gao, X.-Y., Zheng, Y.-F., Chen, Y.-X., & Guo, J. (2012). Geochemical and U–Pb age constraints on the occurrence of polygenetic titanites in UHP metagranite in the Dabie orogen. *Lithos*, *136–139*, 93–108. https://doi.org/10.1016/j.lithos.2011.03.020

Garber, J. M., Hacker, B. R., Kylander-Clark, A. R. C., Stearns, M., & Seward, G. (2017). Controls on trace element uptake in metamorphic titanite: Implications for petrochronology. *Journal of Petrology*, *58*, 1031–1057. doi:10.1093/petrology/egx046

Gibb, R. A., & Thomas, M. D. (1977). The Thelon front: A cryptic suture in the Canadian Shield? *Tectonophysics*, *38*(3–4), 211–222. https://doi.org/10.1016/0040-1951(77)90211-6

Gordon, S. M., Kirkland, C. L., Reddy, S. M., Blatchford, H. J., Whitney, D. L., Teyssier, C., Evans, N. J., & McDonald, B. J. (2021). Deformation-enhanced recrystallization of titanite drives decoupling between U-Pb and trace elements. *Earth and Planetary Science Letters*, *560*, 116810. https://doi.org/10.1016/j.epsl.2021.116810

Hanmer, S. (1988). Great Slave Lake Shear Zone, Canadian Shield: Reconstructed vertical profile of a crustal-scale fault zone. *Tectonophysics*, *149*(3–4), 245–264. https://doi.org/10.1016/0040-1951(88)90176-X

Hanmer, S., Bowring, S., van Breemen, O., & Parrish, R. (1992). Great Slave Lake shear zone, NW Canada: Mylonitic record of Early Proterozoic continental convergence, collison and indentation. *Journal of Structural Geology*, *14*(7), 757–773. https://doi.org/10.1016/0191-8141(92)90039-Y

Hanmer, S., & Lucas, S. B. (1985). Anatomy of a ductile transcurrent shear: The Great Slave Lake Shear Zone, District of Mackenzie, NWT (preliminary report). *Current Research Part B; Geological Survey of Canada, Paper no. 85-1B*, 7–22. https://doi.org/10.4095/120223

Hayden, L. A., Watson, E. B., & Wark, D. A. (2008). A thermobarometer for sphene (titanite). *Contributions to Mineralogy and Petrology*, *155*(4), 529–540. https://doi.org/10.1007/s00410-007-0256-y

Hejl, E., Bernroider, M., Parlak, O., & Weingartner, H. (2010). Fission-track thermochronology, vertical kinematics, and tectonic development along the western extension of the North Anatolian Fault zone. *Journal of Geophysical Research: Solid Earth*, *115*(B10). https://doi.org/10.1029/2010JB007402

Hoffman, P. F. (1987). Continental transform tectonics: Great Slave Lake shear zone (ca. 1.9 Ga), northwest Canada. *Geology*, *15*(9), 785–788. https://doi.org/10.1130/0091-7613(1987)15<785:CTTGSL>2.0.CO;2

Hoffman, P. F. (1988). United Plates of America, the birth of a craton: Early Proterozoic assembly and growth of Laurentia. *Annual Review of Earth and Planetary Sciences*, *16*(1), 543–603. https://doi.org/10.1146/annurev.ea.16.050188.002551

Horstwood, M. S. A., Košler, J., Gehrels, G., Jackson, S. E., McLean, N. M., Paton, C., Pearson, N. J., Sircombe, K., Sylvester, P., Vermeesch, P., Bowring, J. F., Condon, D. J., & Schoene, B. (2016). Community-derived standards for LA-ICP-MS U-(Th-)Pb geochronology – Uncertainty propagation, age interpretation and data reporting. *Geostandards and Geoanalytical Research*, *40*(3), 311–332. https://doi.org/10.1111/j.1751-908X.2016.00379.x

Hull, J. (1988). Thickness-displacement relationships for deformation zones. *Journal of Structural Geology*, *10*(4), 431–435. https://doi.org/10.1016/0191-8141(88)90020-X

Kapp, P., Manning, C. E., & Tropper, P. (2009). Phase-equilibrium constraints on titanite and rutile activities in mafic epidote amphibolites and geobarometry using titanite–rutile equilibria. *Journal of Metamorphic Geology*, *27*(7), 509–521. https://doi.org/10.1111/j.1525-1314.2009.00836.x

Kavanagh-Lepage, C., Gervais, F., Larson, K., Grazziani, R., & Moukhsil, A. (2022). Deformation induced decoupling between U-Pb and trace elements in titanite revealed through petrochronology and study of localized deformation. *Geoscience Frontiers*. https://doi.org/10.1016/j.gsf.2022.101496

Kohn, M. J. (2017). Titanite petrochronology. *Reviews in Mineralogy and Geochemistry*, *83*(1), 419–441. https://doi.org/10.2138/rmg.2017.83.13

Kohn, M. J., & Corrie, S. L. (2011). Preserved Zr-temperatures and U–Pb ages in high-grade metamorphic titanite: Evidence for a static hot channel in the Himalayan orogen. *Earth and Planetary Science Letters*, *311*(1–2), 136–143. https://doi.org/10.1016/j.epsl.2011.09.008

Larson, K. P. (2022). ChrontouR: Geochronology plotting scripts in R [Software]. Open Science Framework. https://doi.org/10.17605/OSF.IO/P46MB

Lusk, A. D. J., & Platt, J. P. (2020). The deep structure and rheology of a plate boundary-scale shear zone: Constraints from an exhumed Caledonian shear zone, NW Scotland. *Lithosphere*, *2020*(1), 8824736. https://doi.org/10.2113/2020/8824736

Ma, S. M., Kellett, D. A., Godin, L., & Jercinovic, M. J. (2020). Localisation of the brittle Bathurst fault on pre-existing fabrics: A case for structural inheritance in the northeastern Slave craton, western Nunavut, Canada. *Canadian Journal of Earth Sciences*, *57*(6), 725–746. https://doi.org/10.1139/cjes-2019-0100

Mao, M., Rukhlov, A. S., Rowins, S. M., Spence, J., & Coogan, L. A. (2016). Apatite trace element compositions: A robust new tool for mineral exploration. *Economic Geology*, *111*(5), 1187–1222. https://doi.org/10.2113/econgeo.111.5.1187

McDonough, M. R., McNicoll, V. J., Schetselaar, E. M., & Grover, T. W. (2011). Geochronological and kinematic constraints on crustal shortening and escape in a two-sided oblique-slip collisional and magmatic orogen, Paleoproterozoic Taltson magmatic zone, northeastern Alberta. *Canadian Journal of Earth Sciences, 37*(11), 1549–1573. https://doi.org/10.1139/e00-089

Miller, A. R., Cumming, G. L., & Krstic, D. (1989). U–Pb, Pb–Pb, and K–Ar isotopic study and petrography of uraniferous phosphate-bearing rocks in the Thelon Formation, Dubawnt Group, Northwest Territories, Canada. *Canadian Journal of Earth Sciences*, *26*(5), 867–880. https://doi.org/10.1139/e89-070

Moser, A. C., Hacker, B. R., Gehrels, G. E., Seward, G. G. E., Kylander-Clark, A. R. C., & Garber, J. M. (2022). Linking titanite U-Pb dates to coupled deformation and dissolution-reprecipitation. *Contributions to Mineralogy and Petrology*, *177*(3), 42. https://doi.org/10.1007/s00410-022-01906-9

Mulch, A., Teyssier, C., Cosca, M. A., & Vennemann, T. W. (2006). Thermomechanical analysis of strain localization in a ductile detachment zone. *Journal of Geophysical Research: Solid Earth*, *111*(B12). https://doi.org/10.1029/2005JB004032

Odlum, M. L., & Stockli, D. F. (2020). Geochronologic constraints on deformation and metasomatism along an exhumed mylonitic shear zone using apatite U-Pb, geochemistry, and microtextural analysis. *Earth and Planetary Science Letters*, *538*, 116177. https://doi.org/10.1016/j.epsl.2020.116177

Okay, A. I., Demirbağ, E., Kurt, H., Okay, N., & Kuşçu, İ. (1999). An active, deep marine strike-slip basin along the North Anatolian fault in Turkey. *Tectonics*, *18*(1), 129–147. https://doi.org/10.1029/1998TC900017

Oriolo, S., Wemmer, K., Oyhantçabal, P., Fossen, H., Schulz, B., & Siegesmund, S. (2018). Geochronology of shear zones – A review. *Earth-Science Reviews*, *185*, 665-683. https://doi.org/10.1016/j.earscirev.2018.07.007

Palin, R. M., & Dyck, B. (2021). Metamorphism of pelitic (Al-rich) rocks. In D. Alderton & S. A. Elias (Eds.), *Encyclopedia of Geology* (Second Edition, pp. 445–456). Academic Press. https://doi.org/10.1016/B978-0-08-102908-4.00081-3

Paton, C., Hellstrom, J., Paul, B., Woodhead, J., & Hergt, J. (2011). Iolite: Freeware for the visualisation and processing of mass spectrometric data. *Journal of Analytical Atomic Spectrometry*, *26*(12), 2508. https://doi.org/10.1039/c1ja10172b

Phillips, R. J., Parrish, R. R., & Searle, M. P. (2004). Age constraints on ductile deformation and long-term slip rates along the Karakoram fault zone, Ladakh. *Earth and Planetary Science Letters*, *226*(3–4), 305–319. https://doi.org/10.1016/j.epsl.2004.07.037

Platt, J. P., & Behr, W. M. (2011). Deep structure of lithospheric fault zones. *Geophysical Research Letters*, *38*(24). https://doi.org/10.1029/2011GL049719

Powell, R., Green, E. C. R., Marillo Sialer, E., & Woodhead, J. (2020). Robust isochron calculation. *Geochronology*, *2*, 325–342. https://doi.org/10.5194/gchron-2-325-2020

Rainbird, R. H., & Davis, W. J. (2007). U-Pb detrital zircon geochronology and provenance of the late Paleoproterozoic Dubawnt Supergroup: Linking sedimentation with tectonic reworking of the western Churchill Province, Canada. *GSA Bulletin, 119*(3–4), 314–328. https://doi.org/10.1130/B25989.1

Ribeiro, B. V., Lagoeiro, L., Faleiros, F. M., Hunter, N. J. R., Queiroga, G., Raveggi, M., Cawood, P. A., Finch, M., & Campanha, G. A. C. (2020). Strain localization and fluid-assisted deformation in apatite and its influence on trace elements and U–Pb systematics.

*Earth and Planetary Science Letters*, *545*, 116421. https://doi.org/10.1016/j.epsl.2020.116421

Scharer, K., & Streig, A. (2019). The San Andreas fault system: Complexities along a major transform fault system and relation to earthquake hazards. In *Transform Plate Boundaries and Fracture Zones* (pp. 249–269). Elsevier. https://doi.org/10.1016/B978-0-12-812064-4.00010-4

Schoene, B., & Bowring, S. A. (2006). U–Pb systematics of the McClure Mountain syenite: Thermochronological constraints on the age of the $^{40}Ar/^{39}Ar$ standard MMhb. *Contributions to Mineralogy and Petrology*, *151*(5), 615. https://doi.org/10.1007/s00410-006-0077-4

Scholz, C. H. (1988). The brittle-plastic transition and the depth of seismic faulting. *Geologische Rundschau*, *77*(1), 319–328. https://doi.org/10.1007/BF01848693

Searle, M. P. (1996). Geological evidence against large-scale pre-Holocene offsets along the Karakoram Fault: Implications for the limited extrusion of the Tibetan plateau. *Tectonics*, *15*(1), 171–186. https://doi.org/10.1029/95TC01693

Sibson, R. H. (1977). Fault rocks and fault mechanisms. *Journal of the Geological Society*, *133*(3), 191–213. https://doi.org/10.1144/gsjgs.133.3.0191

Sibson, R. H. (1983). Continental fault structure and the shallow earthquake source. *Journal of the Geological Society*, *140*(5), 741–767. https://doi.org/10.1144/gsjgs.140.5.0741

Šilerová, D., Dyck, B., Cutts, J. A., & Larson, K. (2022) GSLsz apatite and titanite geochronology [Dataset]. Open Science Framework. https://doi.org/10.17605/OSF.IO/WP3XQ

Spandler, C., Hammerli, J., Sha, P., Hilbert-Wolf, H., Hu, Y., Roberts, E., & Schmitz, M. (2016). MKED1: A new titanite standard for in situ analysis of Sm–Nd isotopes and U–Pb geochronology. *Chemical Geology*, *425*, 110–126. https://doi.org/10.1016/j.chemgeo.2016.01.002

Spencer, K. J., Hacker, B. R., Kylander-Clark, A. R. C., Andersen, T. B., Cottle, J. M., Stearns, M. A., Poletti, J. E., & Seward, G. G. E. (2013). Campaign-style titanite U–Pb dating by laser-ablation ICP: Implications for crustal flow, phase transformations and titanite closure. *Chemical Geology*, *341*, 84–101. https://doi.org/10.1016/j.chemgeo.2012.11.012

Stacey, J. S., & Kramers, J. D. (1975). Approximation of terrestrial lead isotope evolution by a two-stage model. *Earth and Planetary Science Letters*, *26*(2), 207–221. https://doi.org/10.1016/0012-821X(75)90088-6

Stearns, M. A., Hacker, B. R., Ratschbacher, L., Rutte, D., & Kylander-Clark, A. R. C. (2015). Titanite petrochronology of the Pamir gneiss domes: Implications for middle to deep crust exhumation and titanite closure to Pb and Zr diffusion. *Tectonics*, *34*(4), 784–802. https://doi.org/10.1002/2014TC003774

Thériault, R. J. (1992). Nd isotopic evolution of the Taltson Magmatic Zone, Northwest Territories, Canada: Insights into early Proterozoic accretion along the western margin of the Churchill Province. *The Journal of Geology*, *100*(4), 465–475.

Thomson, S. N., Gehrels, G. E., Ruiz, J., & Buchwaldt, R. (2012) Routine low-damage apatite U-Pb dating using laser ablation–multicollector–ICPMS. *Geochemistry, Geophysics, Geosystems*, *13*(2), Q0AA21. https://doi.org/10.1029/2011GC003928

van Breemen, O., Hanmer, S., & Parrish, R. R. (1990) Archean and Proterozoic mylonites along the southeastern margin of the Slave Structural Province, Northwest Territories. *Radiogenic Age and Isotopic Studies: Report 3; Geological Survey of Canada, Paper no. 89-2*, 55–61. https://doi.org/10.4095/129070

Vermeesch, P. (2018). IsoplotR: A free and open toolbox for geochronology. *Geoscience Frontiers*, *9*(5), 1479–1493. https://doi.org/10.1016/j.gsf.2018.04.001

Visual DataTools, Inc. (2021). DataGraph (Version 5.0) [Software]. https://www.visualdatatools.com/

Wallis, D., Lloyd, G. E., & Hansen, L. N. (2018). The role of strain hardening in the transition from dislocation-mediated to frictional deformation of marbles within the Karakoram Fault Zone, NW India. *Journal of Structural Geology*, *107*, 25–37. https://doi.org/10.1016/j.jsg.2017.11.008

Walters, J. B., Cruz-Uribe, A. M., Song, W. J., Gerbi, C., & Biela, K. (2022). Strengths and limitations of in situ U–Pb titanite petrochronology in polymetamorphic rocks: An example from western Maine, USA. *Journal of Metamorphic Geology*, *40*(6), 1043–1066. https://doi.org/10.1111/jmg.12657

Whitney, D. L., & Evans, B. W. (2010). Abbreviations for names of rock-forming minerals. *American Mineralogist*, *95*, 185–187. https://doi.org/10.2138/am.2010.3371

# Long-lived (180 Myr) ductile flow within the Great Slave Lake shear zone

**D. Šilerová[1], B. Dyck[2], J. A. Cutts[2,3], and K. Larson[2]**

[1]Department of Earth Sciences, Simon Fraser University, Burnaby, BC, Canada

[2]Department of Earth, Environmental and Geographical Sciences, University of British Columbia, Kelowna, BC, Canada

[3]Geological Survey of Canada, 601 Booth Street, K1A 0E8, Ottawa, ON, Canada

Corresponding author: Dana Šilerová (dana.silerova@smu.ca)

**Key Points:**

- (Re)crystallized apatite and titanite record a near-continuous history of ductile shear spanning ca. 1920–1740 Ma.
- Strain was initially (ca. 1920–1880 Ma) accommodated by two coeval fault strands.
- A faultward younging in the timing of (re)crystallization is consistent with strain localization during cooling and exhumation.

## Abstract

The Great Slave Lake shear zone (GSLsz) is a type example for deeply eroded continental transform boundaries located in the Northwest Territories, Canada. Formed during the oblique convergence of the Archean Rae and Slave cratons, the GSLsz has accommodated up to 700 km of dextral shear. Here we present the results of *in situ* U-Pb apatite and titanite geochronology from 11 samples that were collected across the strike of the shear zone. Both geochronometers record a near-continuous history of ductile shear during crustal cooling and exhumation that spans ca. 1920–1740 Ma. By integrating the geochronological data with structural and metamorphic observations across the structure, we propose a tectonic model for the shear zone that consists of three stages. The first stage (ca. 1920–1880 Ma) is characterized by strain accommodation along two coeval fault strands. During the second stage (ca. 1880–1800 Ma), ductile shear ceases along the northernmost fault strand and the locus of strain migrates southwards towards the hinterland of the Rae cratonic margin. In the third stage (ca. 1800–1740 Ma), ductile strain localizes back along the southern of the two original fault strands, after which the present-day surface level of the shear zone transitions to brittle shear. Our results highlight both the significance of the lateral migration of the zone of active deformation in major crustal shear zones as well as the localization of strain along existing crustal structures.

## 1 Introduction

Crustal-scale shear zones preserve a record of the temporal and structural evolution of the ductile portions of continental plate boundaries. Over the past few decades, there has been extensive research into the rheological behavior of crustal-scale shear zones (e.g., Scholz, 1988; Sibson, 1977, 1983) leading to a robust understanding of the physical manifestation of plate boundaries at depth (Cawood & Platt, 2021; Lusk & Platt, 2020; Platt & Behr, 2011). However, despite the integral role of these structures in controlling lithospheric strength over long geological periods, there is a general lack of data related to the spatial and temporal evolution of crustal-scale shear zones. The challenges associated with collecting and interpreting geochronological data in shear zones reflect the inherent complexity of shear zone histories as well as the effects of various processes on isotopic diffusion in mineral systems (see Oriolo et al., 2018 and references therein).

The Paleoproterozoic Great Slave Lake shear zone (GSLsz), located in the Northwest Territories, Canada, is a crustal-scale dextral transcurrent structure that marks the boundary between the Archean Rae and Slave cratons (Hanmer, 1988; Hanmer & Lucas, 1985; Hoffman, 1987). Stretching over 1000 km in length, and reaching up to 25 km in width, the GSLsz is one of the largest and best exposed Paleoproterozoic continental transform boundaries in the world. The GSLsz formed as a result of oblique convergence between those cratons, following initial collision ca. 1.95 Ga (Cutts & Dyck, 2022; Gibb & Thomas, 1977).

Extensive surface erosion synchronous with deformation along the GSLsz resulted in the exposure of a series of distinct mylonitic belts within the shear zone (Hanmer, 1988; Hanmer & Lucas, 1985) that preserve a continuous range of metamorphic conditions from the lower greenschist to granulite facies (Hanmer & Lucas, 1985). These mylonitic belts effectively comprise metamorphic units that exhibit decreasing width with decreasing metamorphic grade; the narrower, greenschist-grade belts are overprinted by brittle deformation features (Dyck et al., 2021; Hanmer, 1988; Hanmer et al., 1992). Because these observations are consistent with previously published fault zone models (e.g., Scholz, 1988; Sibson, 1977, 1983), the GSLsz has long been identified as a type example for deeply eroded continental transform boundaries (Dyck et al., 2021; Hanmer, 1988).

Although recent work has answered some of the fundamental questions surrounding the structure and metamorphic evolution of the GSLsz (Cutts & Dyck, 2022; Dyck et al., 2021), the timing of shear along the plate boundary remains poorly quantified. In this study, we document the timing of (re)crystallization of apatite and titanite along the GSLsz and integrate the results with petrographic and geochemical observations. In doing so, the dates are interpreted as reflecting shear-induced (re)crystallization and, thus, provide constraint on the duration of ductile shear in the GSLsz. We present a tectonic model for the GSLsz that can serve as a framework for elucidating histories of other transcurrent continental shear zones, both modern and extinct. This work highlights the importance of integrating various sources of data in order to overcome the challenges associated with interpreting geochronological data in geologically complex systems.

## 2 Geological context

Northwestern Laurentia is an amalgamation of the Archean Slave, Rae, Hearne, and Superior cratons that were assembled along a series of distinct Paleoproterozoic orogenic belts. From west to east these belts include the Wopmay Orogen, the Taltson magmatic zone, the Thelon tectonic zone, the Snowbird tectonic zone, and the Trans-Hudson Orogen (Fig. 1a; Hoffman, 1988). The western boundary of the Rae craton is itself divided into three segments, with the GSLsz forming the central segment. To the northeast of the GSLsz, the Thelon tectonic zone marks the boundary between the Slave and Rae cratons, and to the southwest, the Taltson magmatic zone separates the Rae craton from the Kiskatinaw-Chinchaga-Buffalo Head Superterrane.

The combined Taltson-Thelon margin was initially thought to have formed due to the subduction of oceanic crust beneath the Rae craton and the ensuing collision between Slave and Rae ca. 1.97 Ga (Hoffman, 1987; Thériault, 1992). Recent geochemical and geochronologic work, however, has led to the recognition of the Taltson magmatic zone and Thelon tectonic zone as two distinct structures, rather than one contiguous margin that was dextrally offset by the GSLsz (Berman et al., 2018; Card et al., 2014). The Thelon tectonic zone records older magmatic ages (2.07–1.92 Ga; Berman et al., 2018) and younger metamorphic ages (1.92–1.89 Ga; Berman et al., 2018) than the Taltson magmatic zone, which records younger magmatic ages (1.99–1.92 Ga; Bostock et al., 1987, 1991; Bostock & Loveridge, 1988; Chacko et al., 2000) and older metamorphic ages (1.94–1.92 Ga; Bethune et al., 2013; McDonough et al., 2011).

The GSLsz extends over 1000 km, from the foothills of the Rocky Mountains in the west to the Thelon Basin in the east (Fig. 1a). With the western half of the structure covered by Phanerozoic sedimentary rocks, exposure of the ductile structures is restricted to its eastern half where recent glaciation has contributed to near-continuous exposure of northeast striking mylonite belts. Two major brittle faults run parallel to the strike of the mylonite foliation; the McDonald fault and the Laloche River fault (Fig. 1b). The McDonald fault marks the northern boundary of the GSLsz, separating ultramylonites from the moderately deformed plutonic rocks of the Slave craton (Cutts et al., 2022), while the Laloche River fault bisects the center of the shear zone.

This study focuses on the westernmost segment of the exposed GSLsz (Fig. 1c) where the Laloche River fault separates two distinct structural domains. South of the Laloche River fault, the mylonitic foliation strikes NE–SW, parallel to the strike of the fault, and preserves epidote-amphibolite to greenschist facies metamorphic assemblages. To the north, the foliation strikes NNE-SSW and is truncated by the Laloche River fault. This northern structural domain preserves a series of parallel mylonite belts that last equilibrated under a wide range of metamorphic facies from granulite through to greenschist. The boundaries between metamorphic units are diffuse with higher-grade units overprinted by lower-grade mineral assemblages (Dyck et al., 2021). Accordingly, we define the boundaries between units by the appearance of the lower-grade mineral assemblage (retrograde index minerals).

Rocks from the granulite, upper-amphibolite and epidote-amphibolite belts all reached similar peak metamorphic conditions (~0.85 GPa, ~750 °C), while the final stages of equilibrium recorded by all samples collectively define a single metamorphic field gradient of ~1,000 °C/GPa across the shear zone (Dyck et al., 2021). These findings are consistent with the interpretation of Dyck et al. (2021) that the various mylonitic belts of the GSLsz developed over the course of a single progressive deformation event rather than during temporally distinct events.

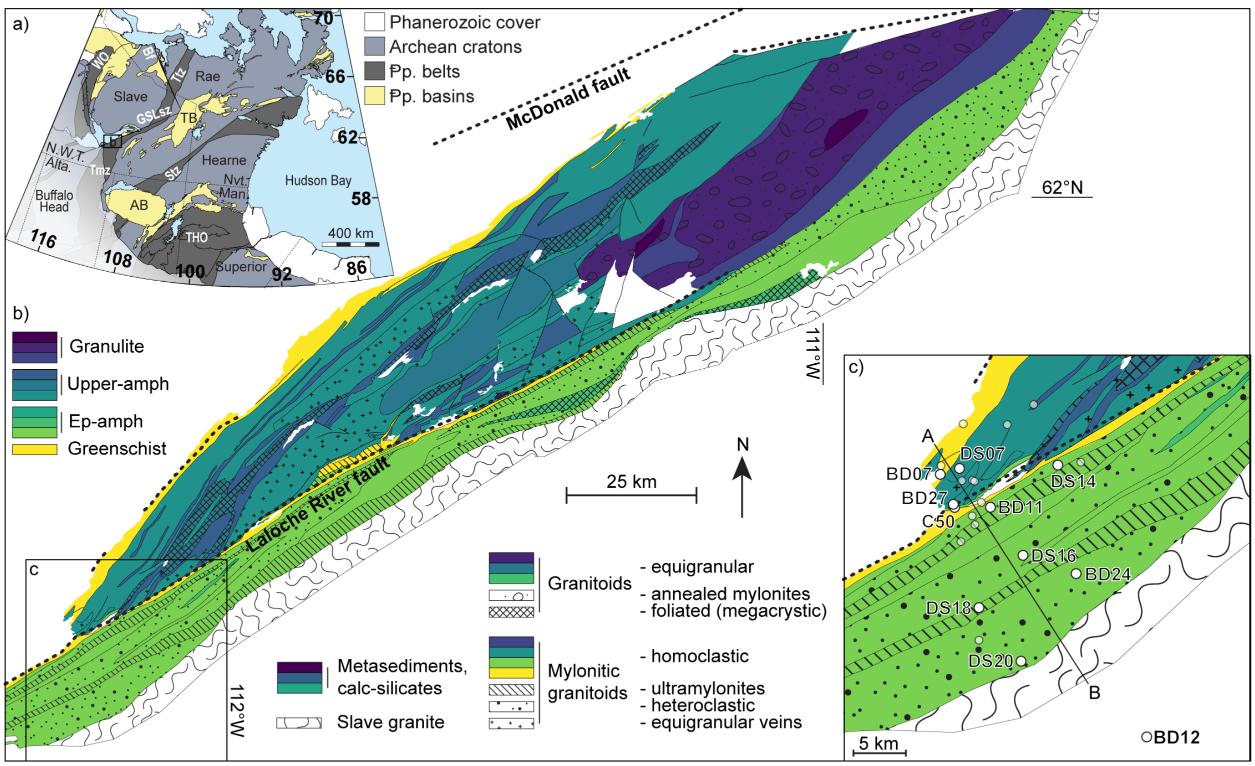


**Figure 1.** (a) Simplified bedrock map of northern Laurentia showing the positions of Archean cratons and other major tectonic elements, including the Great Slave Lake shear zone (GSLsz), Bathurst fault (Bf), Taltson magmatic zone (Tmz), Thelon tectonic zone (Ttz), Snowbird tectonic zone (Stz), Wopmay Orogen (WO), Trans-Hudson Orogen (THO), Thelon Basin (TB), and Athabasca Basin (AB). N.W.T – Northwest Territories, Alta. – Alberta, Nvt. – Nunavut, Man. – Manitoba. (b) Metamorphic units of the southwestern segment of the GSLsz. Units are based on protolith lithology as mapped by Hanmer (1988). (c) Field area with sample locations

(translucent white circles) and transect line; location shown in 1b. Samples used for accessory mineral petrochronology are labeled and marked by larger opaque white circles.

### 2.1 Previous geochronological work

Although several decades have passed since the GSLsz was first recognized as a major tectonic structure in northwestern Laurentia, there is a lack of modern geochronologic information for the timing and duration of ductile shear. Early attempts to date the structure used U-Pb ID-TIMS geochronology on zircon and the results were interpreted to indicate that peak activity of the shear zone occurred at ca. 1.980–1.924 Ga along its southwestern segment (Hanmer et al., 1992) and by 1978 ± 5 Ma along its northeastern segment (van Breemen et al., 1990). Transform motion along the shear zone was proposed to be bracketed between ca. 2.00–1.86 Ga (Bowring et al., 1984; Hanmer et al., 1992). However, the dates used to inform the timing of transform movement relied on geochronology from the host mylonitic granitoids or on interpretations of cross-cutting relationships between intrusive units and the mylonites rather than directly dating shear-induced recrystallization. Following its main period of activity, the GSLsz was offset dextrally by the McDonald fault. Late synkinematic dyke emplacement and biotite cooling ages constrain the onset of brittle deformation along the McDonald fault and conjugate Bathurst fault to ca. 1840 Ma, while a depositional age of ca. 1758 Ma for nearby synorogenic basin units has been proposed to bracket the end of brittle activity in the McDonald-Bathurst fault system (Ma et al., 2020; Rainbird & Davis, 2007).

Recent geochronological work done on samples from the southwestern segment of the GSLsz found that zircon and monazite U-Pb ages are unrelated to the transcurrent motion of the shear zone and, instead, record a margin-wide crustal thickening event associated with convergence of the Slave and Rae cratons (Cutts & Dyck, 2022). The timing of the peak metamorphism associated with crustal thickening is best informed by two garnet Lu-Hf ages of 1931 ± 12 and 1917 ± 6 Ma, which overlap the ca. 1933–1913 Ma age range recorded by zircon and monazite (Cutts & Dyck, 2022). Based on the observations of suprasolidus shear microstructures (Dyck et al., 2021; Hanmer et al., 1992), the maximum age of ductile shear along the GSLsz has been interpreted to coincide with the final stages of peak metamorphism at ca. 1920–1910 Ma (Cutts & Dyck, 2022).

## 3 Methods

### 3.1 Apatite and titanite geochronology

We conducted a ~15 km across-strike transect through the GSLsz to evaluate the record of shear-induced (re)crystallization preserved therein. Along the transect, we recorded the orientation of ductile fabrics as well as the characteristic metamorphic mineral assemblages. We collected 22 samples from which 11 were selected for *in-situ* U-Th-Pb accessory mineral petrochronology (Fig. 1c). Given the apparent lack of sensitivity of zircon and monazite to record the timing of deformation (Cutts & Dyck, 2022), we focused our study on apatite and titanite. Both minerals have a well-documented tendency to recrystallize during ductile deformation (e.g., Gordon et al., 2021; Kavanagh-Lepage et al., 2022; Moser et al., 2022; Odlum & Stockli, 2020; Ribeiro et al., 2020; Walters et al., 2022). Ten of the eleven samples are apatite-bearing and ten are titanite-bearing.

Target apatite and titanite grains were first identified in thin section using transmitted light microscopy. Following this, we collected backscattered electron (BSE; apatite, titanite) and cathodoluminescence (CL; apatite) images to determine the relationship of each grain with ductile fabrics and to identify zoning within individual grains. BSE imaging was done using the Tescan Mira 3 XMU field emission scanning electron microscope (SEM) at the Fipke Laboratory for Trace Element Research (FiLTER) at the University of British Columbia, Okanagan. For CL imaging, we used a Thermo Prisma tungsten-source SEM equipped with a four-channel polychromatic CL camera housed in the Department of Earth Sciences at Simon Fraser University. For both BSE and CL, we coated the samples with ~10 nm of carbon and used an accelerated voltage of 15 kV at a working distance of 10 mm.

*In-situ* U-Pb isotope and trace element analyses of apatite and titanite was carried out via laser ablation inductively coupled plasma mass spectrometry (LA-ICP-MS) in the FiLTER facility at the University of British Columbia, Okanagan. In total, twelve separate analytical sessions were run (four with apatite; eight with titanite). All spot analyses within individual samples were collected during the same session, except the titanite in GSL-18-C50, for which data were collected across two sessions. Five of the titanite sessions used a Photon Machines Analyte 193nm ArF excimer laser ablation system coupled to an Agilent 8900 Triple Quadrupole (QQQ) ICP-MS operated in single-quad mode. The other three titanite sessions and all four apatite sessions used an ESI New Wave Research 193nm ArF excimer laser ablation system coupled to an Agilent 8900 QQQ-ICP-MS operated in single-quad mode. Each session consisted of analyses of one to three apatite- or titanite-bearing samples. U-Pb isotopic ratios and trace element concentrations were collected from the same ablated spot volumes. Instrumentation settings for each analytical session are provided in Table S1. All U-Pb isotope and trace element data collected for unknowns and reference materials are presented in Tables S2 and S3 for apatite and titanite, respectively.

Apatite grains were ablated using a fluence of 4.00 J/cm$^2$, an ablation frequency of 8.00 Hz, and a spot size of 40 μm. Titanite grains were ablated using a fluence of 4.00–4.95 J/cm$^2$, an ablation frequency of 8.00 Hz, and a spot size between 25–40 μm. Prior to each spot analysis, the surface was pre-ablated with two laser pulses to clear the sample surface of debris. The acquisition run for each spot analysis lasted between 25–30 seconds and was followed by a washout period, lasting 10 seconds. Blocks of 8–10 unknown analyses were separated by analyses of reference materials for calibration purposes and to correct for instrumental drift and down-hole fractionation.

The primary reference material used for all apatite U-Pb LA-ICP-MS analyses was MAD1 (Thomson et al., 2012) as characterized in Apen et al. (2022; lower intercept age of 467 ± 9 Ma). Both MRC-1 (isochron age = 153.3 ± 0.2 Ma; Apen et al., 2022) and Mount McClure (common Pb corrected via total Pb-U isochron = 523.51 ± 1.53 Ma; Schoene & Bowring, 2006) apatite reference materials were analyzed as unknowns to assess reproducibility. Analyses of MRC-1 yielded lower intercept dates in Tera-Wasserburg space of 154 ± 1 Ma (mean squared weighted deviates [MSWD] = 1, n = 12/12), 155 ± 2 Ma (MSWD = 0.91, n = 14/15), 157 ± 2 Ma (MSWD = 1, n = 20/20), and 152 ± 2 Ma (MSWD = 1.7, n = 10/10). The two analytical runs that included Mount McClure apatite returned lower intercept dates of 522 ± 6 Ma (MSWD = 5.5, n = 14/15) and 531 ± 17 Ma (MSWD = 1.6, n = 19/20). With one exception, all analyses of apatite secondary reference materials overlap within uncertainty of expected ages; the one exception is within 1% of the expected age.

The reference materials used for titanite geochronology include MKED1, Mount McClure, and Mud Tank. MKED1 was used as the primary reference material for all titanite isotopic analyses ($^{206}Pb/^{238}U$ age of 1517.32 ± 32 Ma; Spandler et al., 2016). To assess the accuracy of the U-Pb results, the Mount McClure titanite reference material (common Pb corrected via total Pb-U isochron = 523.26 ± 0.72 Ma; Schoene & Bowring, 2006) was analyzed as an unknown in five analytical sessions while the titanite reference material Mud Tank (318.7 ± 1.0 Ma; Fisher et al., 2020) was used for the remaining three sessions. LA-ICP-MS analyses of Mount McClure titanite typically contain significant and variable common Pb contents. As such, lower intercept dates in Tera-Wasserburg space are used to assess how well the expected age was reproduced. Analyses of Mount McClure titanite yielded dates of 522 ± 3 Ma (MSWD = 1.7, n = 9/10), 529 ± 4 (MSWD = 0.72, n = 5/5), 523 ± 14 Ma (MSWD = 2.3, n = 6/6), 522 ± 12 Ma (MSWD = 2.1, n = 8/8), and 528 ± 4 Ma (MSWD = 1.3, n = 13/13). With one exception, all dates overlap the expected date within analytical uncertainty. The exception is well within (0.1%) the expected uncertainties associated with LA-ICP-MS U-Pb geochronology (e.g., Horstwood et al., 2016). Analyses of Mud Tank titanite were essentially homogeneous with respect to common Pb, and as such, $^{207}Pb$-corrected (Stacey & Kramers, 1975) $^{206}Pb/^{238}U$ weighted mean dates were used to assess reproducibility. The three analytical runs with Mud Tank titanite yielded dates of 319 ± 1 Ma (MSWD 2.9, n = 9/10), 316 ± 1 Ma (MSWD 1.5, n = 13/14) and 316 ± 1 Ma (MSWD 1.2, n = 17/17). All Mud Tank results are within 0.3% of the expected date, again well-within expected reproducibility.

Glasses NIST 610 and NIST 612 were used as reference materials for trace element analyses for both apatite and titanite. Concentrations were normalized to assumed stoichiometric concentrations of Ca for apatite and Si for titanite. Trace element concentrations in secondary reference materials are typically within 5–15% of expected values, with Zr < 5%.

### 3.2 U-Pb data analysis

The LA-ICP-MS data were initially reduced using Iolite (Paton et al., 2011) to normalize down-hole fractionation and instrument drift over analytical runs. Excess dispersion in the $^{207}Pb/^{206}Pb$ and $^{206}Pb/^{238}U$ ratios was calculated from secondary reference materials (e.g., Mount McClure, Mud Tank, MRC-1) and added to apatite and titanite analyses using in-house data processing scripts. Typical dispersion values were < 1.5%. Tera-Wasserburg diagrams and trace element plots were constructed using ChrontouR (Larson, 2022) and DataGraph (Visual DataTools, 2021). When constructing Tera-Wasserburg diagrams for specimens with multiple populations, the intercept of a single regression through all included data was used for the individual regressions to be internally consistent. Uncertainties reported in-text and depicted in figures refer to internal (2 standard error; 2SE) uncertainties only.

### 3.3 Zirconium-in-titanite geothermometry

Zirconium (Zr) concentrations were measured in each titanite spot analysis and (re)crystallization temperatures were calculated using the Zr-in-titanite geothermometer of Hayden et al. (2008). The activities of titania ($TiO_2$) and silica ($SiO_2$) were assumed to be 0.8 and 1.0, respectively; an activity of titania between 0.75–0.85 is considered an acceptable estimate for a wide range of metamorphic rocks (Kapp et al., 2009; Kohn, 2017). Recent estimates for the last recorded equilibrium conditions across most metamorphic units in the field area include pressures between approximately 0.4–0.7 GPa (Dyck et al., 2021). Because it is difficult to determine the equilibrium mineral assemblage associated with titanite crystallization, as well as the lack of independent pressure constraints for the samples analyzed, we chose a value of 0.5 GPa as the best approximation for pressure as it applies to the broadest range of samples. Temperatures calculated with the Zr-in-titanite geothermometer are only moderately pressure-dependent; a change in pressure of 0.1 GPa corresponds to a change in temperature of 10–13 °C for the grains analyzed. Uncertainties reported for temperatures in-text reflect the standard calibration uncertainty of ± 20 °C reported by Hayden et al. (2008).

# 4 Results

## 4.1 Sample petrography

Of the 11 samples selected for *in situ* U-Th-Pb accessory mineral petrochronology, 4 were collected north of the Laloche River fault (GSL-18-BD07, GSL-21-DS07, GSL-18-BD27, GSL-18-C50) while the remaining 7 are from south of the fault (Fig. 1c). Detailed petrographic descriptions for all samples are presented in Text S1, photomicrographs of key microstructural features in Figure 2, and grain characteristics of apatite and titanite in Table 1.

The four samples collected in the northern structural domain exhibit broad ranges in degree of mylonitization, lithology, and metamorphic facies, with three samples (GSL-21-DS07, GSL-18-BD27, GSL-18-C50) of mylonitic schist and one (GSL-18-BD07) of ultramylonitic granodiorite. The preserved metamorphic facies in the four samples range from the greenschist facies (GSL-18-BD07) to the epidote-amphibolite (GSL-21-DS07, GSL-18-C50) and upper-amphibolite facies (GSL-18-BD27). Two of the samples (GSL-18-BD07, GSL-18-C50) contain both apatite and titanite, whereas the remaining two samples each contain only one of the minerals (titanite in GSL-21-DS07; apatite in GSL-18-BD27). Apatite and titanite occur primarily in the matrix of each sample and are aligned with the foliation (Fig. 2a). One exception is GSL-21-DS07, in which there is extensive evidence of late fluid alteration and titanite occurs predominantly along late, coarse-grained quartz-epidote veins (Fig. 2b). Another exception is GSL-18-C50, which consists of a very fine-grained mylonitic matrix that wraps large clinozoisite–amphibole–titanite pseudomorphs after garnet (Dyck et al., 2021). Most apatite and titanite grains in the sample occur within the garnet pseudomorph and are aligned oblique to the matrix foliation.

South of the Laloche River fault, six samples (GSL-21-DS14, GSL-18-BD11, GSL-21-DS16, GSL-21-DS18, GSL-18-BD24, GSL-21-DS20) were collected from the southern structural domain of the shear zone while the remaining sample (GSL-21-BD12) was collected from a supracrustal unit in the Rutledge Group south of the shear zone (Fig. 1c). Except for GSL-21-DS14 (greenschist facies), all samples collected from the southern structural domain preserve epidote-amphibolite facies mineral assemblages. Furthermore, all six samples exhibit similar mineralogy and microstructure, with one of the six (GSL-18-BD11) identified as a mylonitic granodiorite and the remaining five as amphibole mylonitic granodiorites. The sample collected south of the shear zone (GSL-21-BD12) stands apart as an upper-amphibolite facies amphibole schist. All samples exhibit a strong, anastomosing foliation that is defined by the orientation of matrix-forming minerals, usually amphibole or biotite, and by the alignment of quartz ribbons and micaceous layers. Each of the seven samples contains both apatite and titanite, the grains of which occur primarily in the mylonitic matrix and are well-aligned with the foliation (Figs. 2c & d). One sample (GSL-21-DS16) contains two titanite populations, identified based on textural observations (Fig. 2e). The first population consists of sub- to anhedral titanite grains that are well-aligned with the foliation (referred to as “fabric-aligned titanite”), while the second consists of small, round titanite grains clustered together around long masses of ilmenite (“clustered titanite”). Several samples contain titanite grains that exhibit distinct core-rim structures (Fig. 2f).

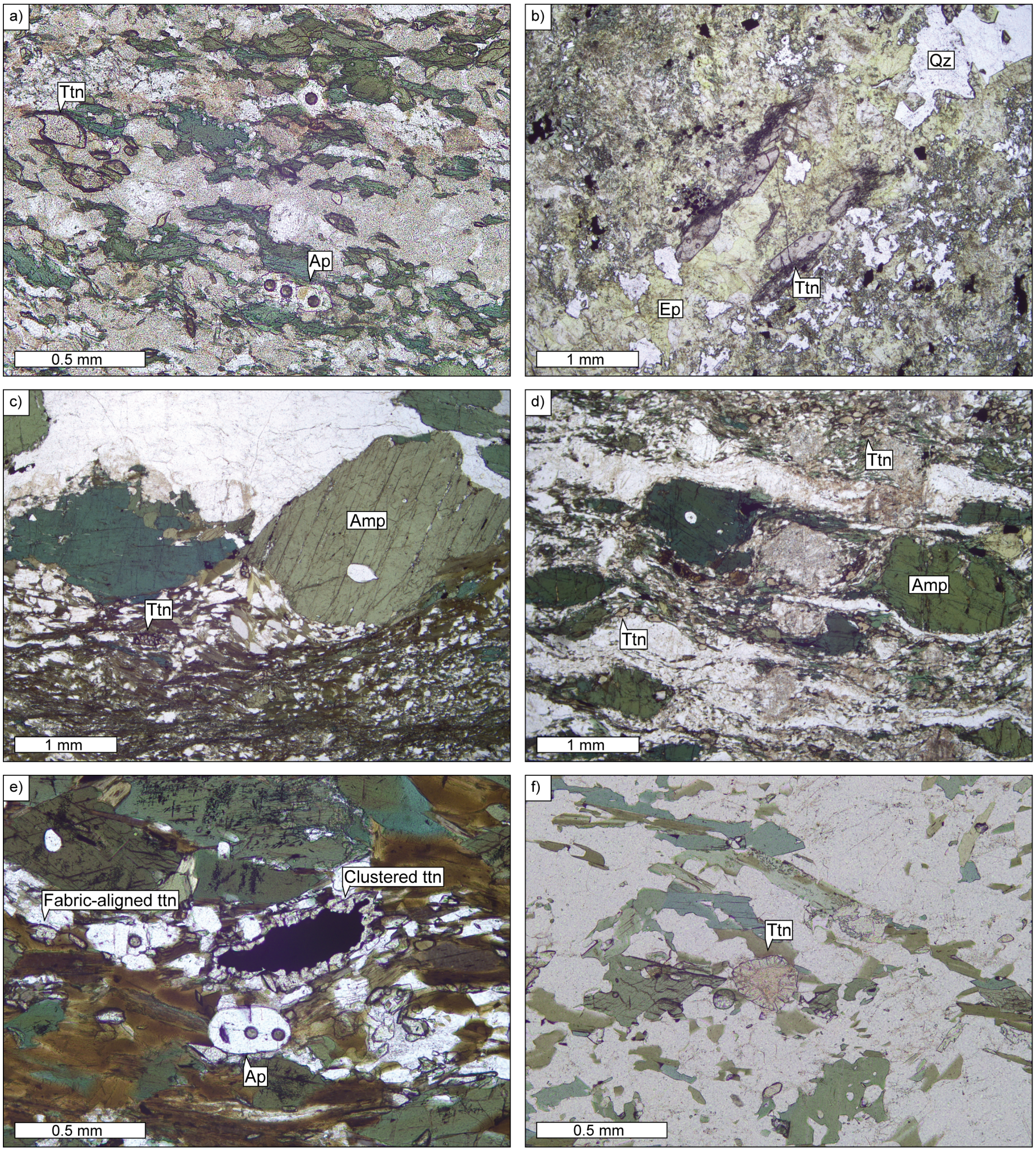


**Figure 2.** Summary of microstructural characteristics of apatite- and titanite-bearing samples. Mineral abbreviations follow Whitney and Evans (2010). (a) Well-aligned apatite and titanite

grains (GSL-18-BD07). (b) Titanite grains associated with late coarse-grained quartz-epidote vein (GSL-21-DS07). (c) Mylonitic fabric defined by fine-grained micaceous domains wrapping around amphibole porphyroclasts (GSL-21-DS14). (d) Well-developed foliation wrapping amphibole porphyroclasts (GSL-21-DS18). (e) Fabric-aligned and clustered titanite grains in GSL-21-DS16. (f) Core-rim structure visible in a titanite grain (GSL-18-BD24).

**Table 1.** Summary of apatite and titanite grain characteristics.

| **Sample** | **Latitude (degrees)** | **Longitude (degrees)** | **Mineral** | **Grain characteristics** | | | | |
|---|---|---|---|---|---|---|---|---|
| | | | | **Occurrence** | **Relationship to fabric** | **Size (µm)** | **Shape** | **Zoning** |
| GSL-18-BD07 | 61.643778 | -112.212944 | Ap | Matrix | Aligned | 50–100 | Sub- to anhedral | Patchy core-rim |
| | | | Ttn | Matrix | Aligned | 60–700 | Elongate, sub- to euhedral | Homogeneous or irregular patchy |
| GSL-21-DS07 | 61.646371 | -112.195418 | Ttn | Along qz-ep veins | Not aligned | 200–1000 | Euhedral | Oscillatory |
| GSL-18-BD27 | 61.630500 | -112.200944 | Ap | Matrix + inclusions in grt | Varies | 50–200 | Rounded, subhedral | Homogeneous |
| GSL-18-C50 | 61.629250 | -112.199889 | Ap | Within grt pseudomorph (+ matrix) | Oblique (+ aligned) | 50–400 | Anhedral, fractured | Patchy or core-rim |
| | | | Ttn | Within grt pseudomorph | Oblique | 100–800 | Rhombic | Patchy or oscillatory |
| GSL-21-DS14 | 61.647845 | -112.105861 | Ap | Matrix | Aligned | 60–500 | Elongate | Patchy |
| | | | Ttn | Matrix | Aligned | 50–200 | Subhedral | Core-rim |
| GSL-18-BD11 | 61.629250 | -112.167250 | Ap | Matrix | Aligned | 60–250 | Elongate, sub- to anhedral | Oscillatory or core-rim |
| | | | Ttn | Matrix, along micaceous layers | Aligned | 20–120 | Blocky | Homogeneous |

| | | | | | | | | |
|---|---|---|---|---|---|---|---|---|
| GSL-21-DS16 | 61.608126 | -112.137535 | Ap | Matrix, in amp-rich domains | Aligned | 80–250 | Rounded, elongate | Irregular core-rim |
| | | | Ttn | Fabric-aligned ttn: matrix | Aligned | 25–120 | Sub- to anhedral | Core-rim |
| | | | | Clustered ttn: surrounding masses of ilm | Not aligned | 25–120 | Elongate clusters of rounded grains | Core-rim |
| GSL-21-DS18 | 61.585146 | -112.177447 | Ap | Matrix | Aligned | 50–200 | Elongate, sub- to euhedral | Patchy, uncommon bright cores |
| | | | Ttn | Matrix, often with bt | Aligned | 50–350 | Elongate, sub- to anhedral | Irregular patchy |
| GSL-18-BD24 | 61.600083 | -112.089167 | Ap | Matrix | Aligned | 50–200 | Elongate, sub- to euhedral | Patchy, uncommon bright cores |
| | | | Ttn | Matrix | Aligned | 100–1500 | Sub- to anhedral | Core-rim |
| GSL-21-DS20 | 61.561525 | -112.139314 | Ap | Matrix | Aligned | 70–300 | Elongate, sub- to euhedral | Irregular oscillatory |
| | | | Ttn | Matrix, often with amp + bt | Aligned | 50–500 | Rhombic | Homogeneous |
| GSL-21-BD12 | 61.530367 | -112.034200 | Ap | Matrix + inclusions in amp | Varies | 50–200 | Anhedral | Patchy core-rim |
| | | | Ttn | Matrix | Aligned | 50–200 | Blocky to anhedral | Patchy core-rim |

**Note.** Samples are ordered geographically, NW to SE. Mineral abbreviations follow Whitney and Evans (2010).

4.2 Apatite U-Pb and trace element results

Tera-Wasserburg diagrams and representative REE profiles for all apatite populations are presented in Figures 3 and 4a, respectively. Detailed trace element plots as well as BSE and CL images of representative grains for all populations are presented in Figure S1 and full analytical results for all unknowns and reference materials are reported in Table S2. In the following text, unless otherwise specified, uncertainties reported refer to internal uncertainties only and do not reflect the externally reproducible uncertainties.

All apatite-bearing samples contain one main age population (Fig. 3). Lower intercept dates were calculated using the robust regression of Powell et al. (2020) for all populations and range from ca. 1920–1760 Ma. The oldest apatite populations are from samples collected north of the Laloche River fault and yield lower intercept dates of 1918 ± 10 Ma (GSL-18-C50; spine width [s] = 0.67) and 1915 ± 12 Ma (GSL-18-BD07; s = 0.57). The remainder of the apatite populations yield lower intercept dates between ca. 1860–1760 Ma.

Apatite spot analyses across all samples yield similar REE profiles with the main difference between analyses being the relative abundance of elements. Analyses that are classified as low-U analyses (<0.4 ppm) and that correspond to grains that disaggregated during ablation tend to exhibit the lowest overall concentrations of REE.

Four samples (GSL-18-BD27, GSL-21-DS14, GSL-21-DS18, GSL-21-DS20) exhibit depletion in Eu relative to Sm and Gd (Fig. 4a) with mean Eu/Eu* ranging from 0.15–0.60, the greatest of which is recorded in GSL-18-BD27 (mean Eu/Eu* = 0.15). There does not appear to be a correlation between Eu/Eu* and other REE ratios.

Three samples (GSL-18-BD27, GSL-18-C50, GSL-21-DS16) exhibit significant enrichment of LREE relative to HREE (Fig. 4a), with mean $La_n/Yb_n$ ranging from 16.79–17.76. Despite the similarities in relative LREE enrichment, these three samples exhibit distinct REE profiles. GSL-18-BD27 has a significant negative Eu anomaly, giving its REE profile a sawtooth appearance, while GSL-18-C50 and GSL-21-DS16 exhibit steadier decreases in REE concentration across their profiles, consistent with the overall enrichment of LREE relative to HREE observed (Fig. 4a). Five samples (GSL-18-BD07, GSL-21-DS18, GSL-18-BD24, GSL-21-DS20, GSL- 21-BD12) also exhibit enrichment of LREE relative to HREE (Fig. 4a), but record slightly lower mean $La_n/Yb_n$, with values ranging from 2.06–9.20. Meanwhile, the two remaining samples (GSL-21-DS14, GSL-18-BD11) exhibit an overall depletion of LREE relative to HREE (Fig. 4a), with mean $La_n/Yb_n$ of 0.45 and 0.49, respectively.

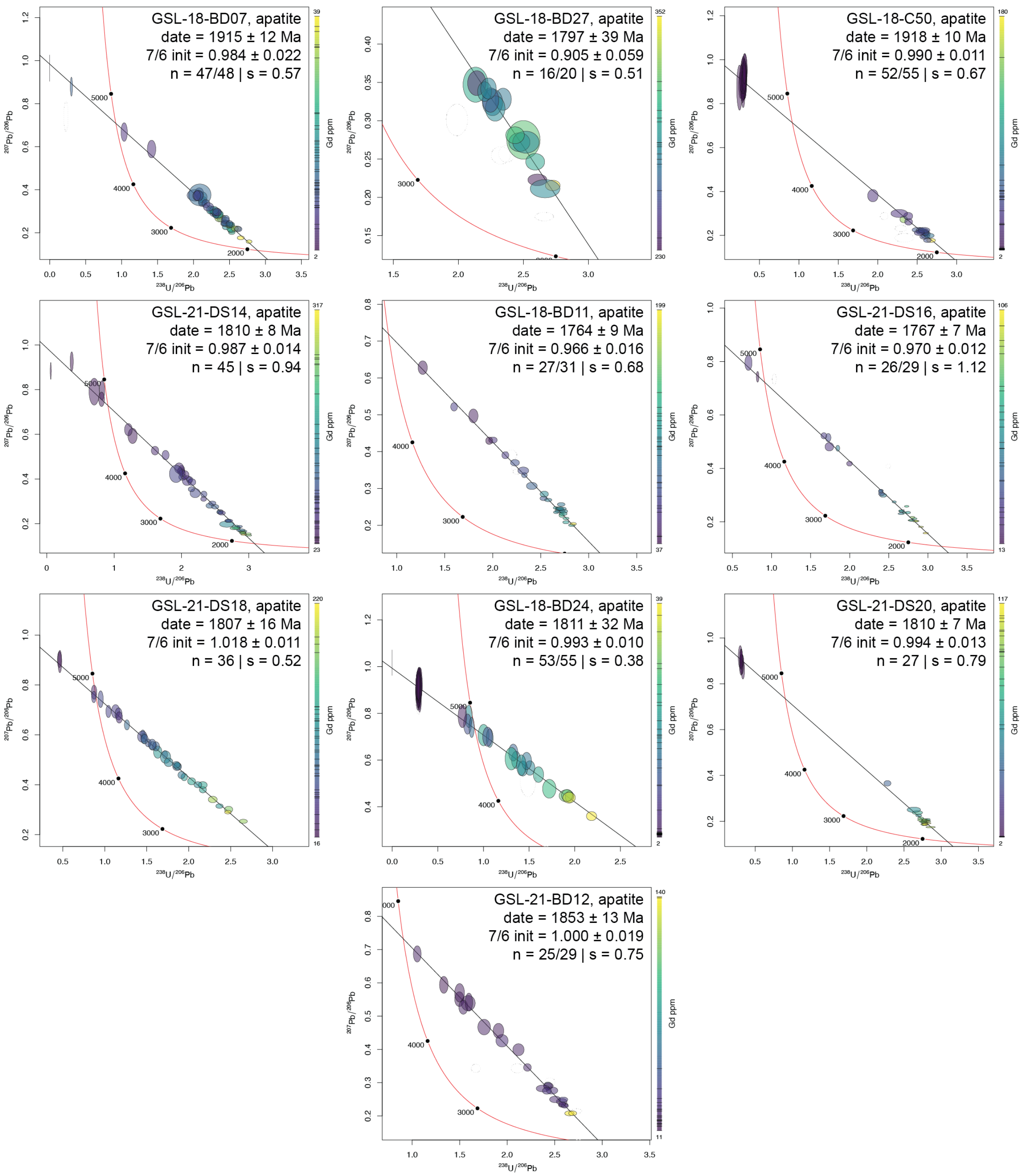


348

349 **Figure 3.** Tera-Wasserburg diagrams for each apatite population, constructed using ChrontouR
350 (Larson, 2022). 7/6 init – initial $^{207}Pb/^{206}Pb$ ratio.

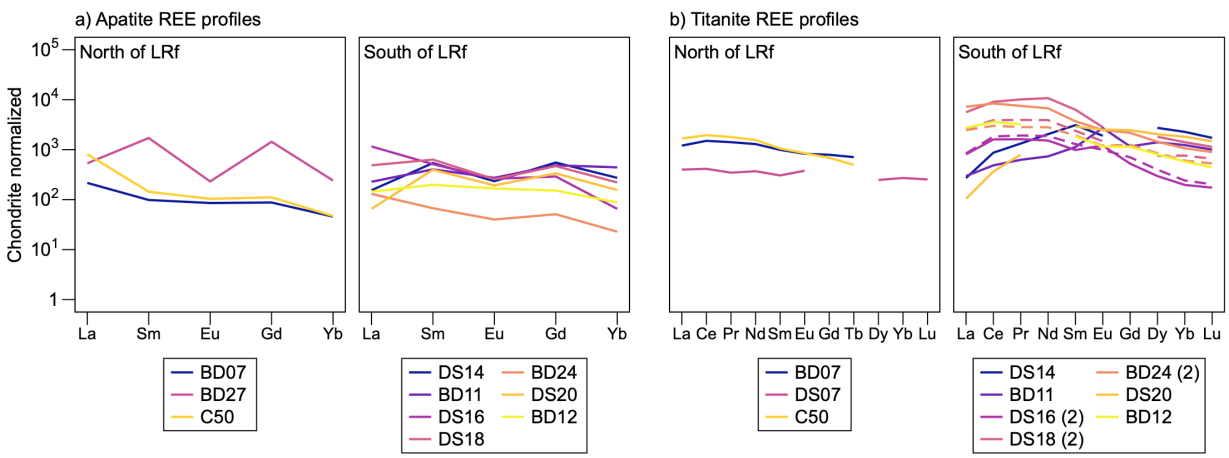


**Figure 4.** Average REE profiles for all apatite (a) and titanite (b) populations. All samples contain one population of each mineral, except for DS16, DS18, and BD24, which each contain two titanite populations; dashed lines indicate secondary populations (clustered titanite in DS16; BSE-dark titanite in DS18, BD24). LRf – Laloche River fault.

4.3 Titanite U-Pb and trace element results

Tera-Wasserburg diagrams and representative REE profiles for all titanite populations are presented in Figures 5 and 4b, respectively. Detailed trace element plots and BSE images of representative grains for all populations are presented in Figure S2 and full analytical results for all unknowns and reference materials are reported in Table S3. As with the apatite data, unless otherwise specified, uncertainties reported in-text refer to internal uncertainties only.

With the exceptions of GSL-18-BD24, GSL-21-DS16, and GSL-21-DS18, which each contain two distinct populations characterized by differences in grain morphology and trace element profiles, most titanite-bearing samples contain one main age population (Fig. 5). Lower intercept dates were calculated for all populations and range from ca. 1910–1740 Ma across the shear zone. The oldest titanite populations yield lower intercept dates of 1904 ± 9 Ma (GSL-18-BD07; s = 1.19) and 1888 ± 11 Ma (GSL-18-C50; s = 1.27) and occur in the same two samples that have the oldest apatite populations. Meanwhile, the youngest titanite populations are from samples collected south of the Laloche River fault and yield lower intercept dates of 1740 ± 9 Ma (GSL-21-DS14; s = 0.90) and 1768 ± 9 Ma (clustered titanite in GSL-21-DS16; s = 1.11). The remainder of the lower intercept dates fall between ca. 1870–1790 Ma.

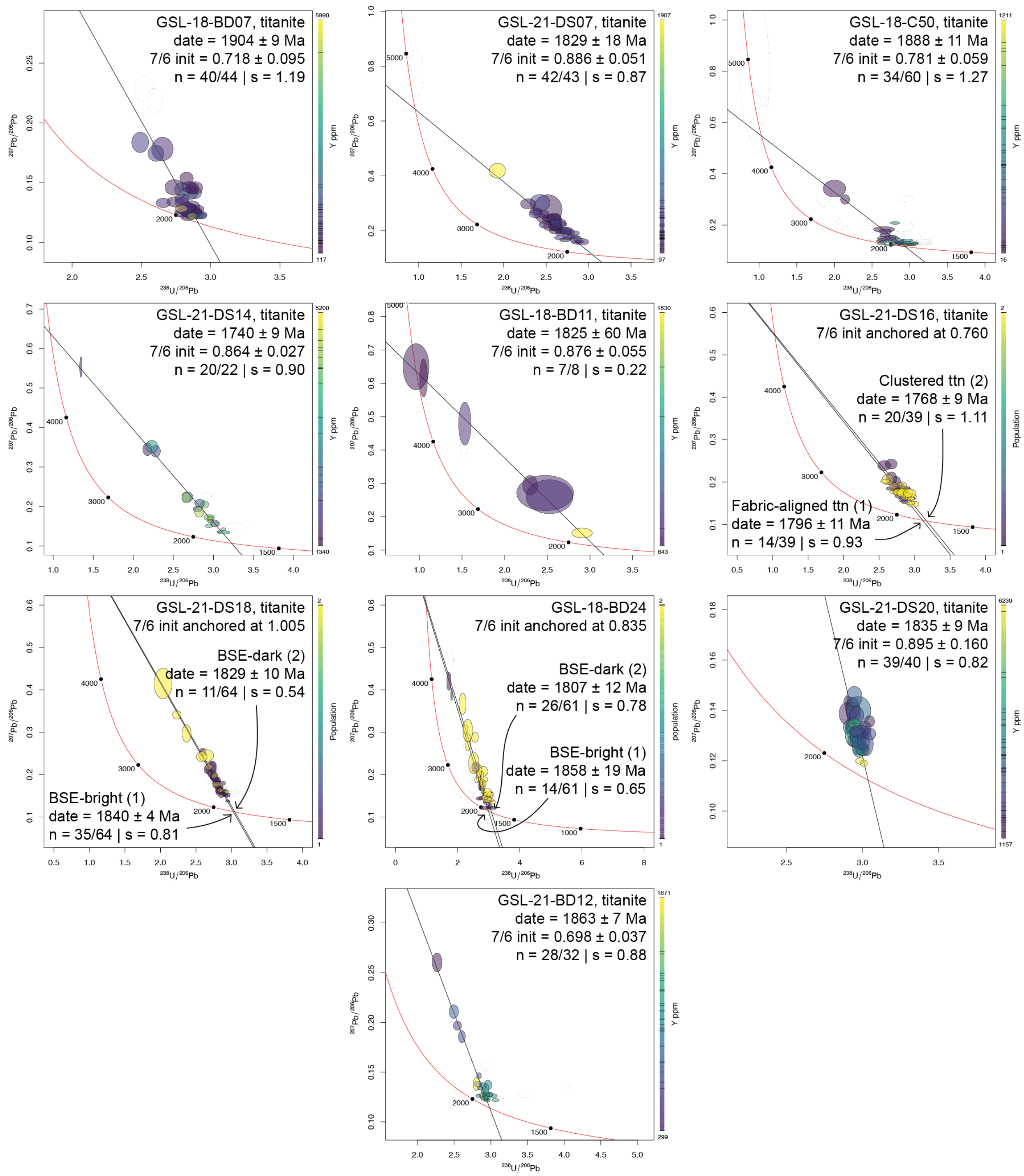


**Figure 5.** Tera-Wasserburg diagrams for each titanite population, constructed using ChrontouR (Larson, 2022). 7/6 init – initial $^{207}Pb/^{206}Pb$ ratio.

Most analyses within individual samples have similar REE profiles with the main difference between analyses being the relative abundance of elements. Seven populations (GSL-21-BD12, two in GSL-18-BD24, two in GSL-21-DS16, two in GSL-21-DS18) exhibit strikingly similar concave-down REE profiles that show an overall enrichment in LREE relative to HREE

(Fig. 4b). These samples record mean $La_n/Lu_n$ ranging from 4.24–8.67. All seven populations exhibit little to no enrichment of LREE relative to MREE, with mean $La_n/Sm_n$ ranging from 0.67–2.11; however, all seven populations show enrichment of MREE relative to HREE, with mean $Sm_n/Lu_n$ ranging from 3.37–6.34. Three additional samples (GSL-21-DS14, GSL-18-BD11, GSL-21-DS20) also have concave-down REE profiles but show an overall depletion in LREE relative to HREE (Fig. 4b), with mean $La_n/Lu_n$ ranging from 0.08–0.38. All three further exhibit a depletion in LREE relative to MREE, with mean $La_n/Sm_n$ ranging from 0.04–0.43, as well as a relatively low enrichment of MREE relative to HREE, with mean $Sm_n/Lu_n$ ranging from 1.04–1.90. One sample (GSL-21-DS07) has a relatively flat REE profile compared to the others (Fig. 4b), with a mean $La_n/Lu_n$ of 1.71. The mean $La_n/Sm_n$ and $Sm_n/Lu_n$ are similarly stable, with values of 1.43 and 1.23.

The REE profiles for the distinct age populations in GSL-18-BD24, GSL-21-DS16, and GSL-21-DS18 differ. In GSL-21-DS16, most of the analyses from the fabric-aligned titanite population exhibit enrichment in Eu relative to Sm and Gd, whereas there is no enrichment in Eu in the analyses from the clustered titanite population (Fig. 4b). In GSL-18-BD24 and GSL-21-DS18, the BSE-bright and BSE-dark populations exhibit similar overall patterns in REE profiles, however, the BSE-dark analyses typically record lower REE concentrations than the analyses from BSE-bright domains (Fig. 4b). For example, Sm concentrations in GSL-18-BD24 range from 271–932 ppm (BSE-bright) compared with 49–606 ppm (BSE-dark), while in GSL-21-DS18, they range from 328–1384 ppm (BSE-bright) compared with 146–812 ppm (BSE-dark).

### 4.4 Zr-in-titanite thermometry

Zr-in-titanite temperatures were calculated for each of the titanite analyses following the steps outlined by Hayden et al. (2008). Mean and median temperatures were calculated for each titanite population. Mean temperatures are used for comparison between populations. A box-and-whisker plot of temperatures calculated for each titanite population is presented in Figure 6 and full results are reported in Table S4. Titanite records temperatures ranging from approximately 630–950 °C across all samples. Mean temperatures calculated for each of the thirteen titanite populations range from 674 ± 20 °C (GSL-21-DS07) up to 768 ± 20 °C (GSL-18-C50).

## 5 Discussion

### 5.1 A temporal record of dynamic (re)crystallization

The lower intercept dates recorded by all apatite and titanite populations are plotted in Figure 6 according to sample position along the transect of the study area. The apatite and titanite chronometers yield overlapping ranges of dates across the shear zone, spanning from ca. 1920–1760 Ma and ca. 1910–1740 Ma, respectively. The range of dates recorded by both chronometers post-date prograde-to-peak metamorphism in the shear zone as recorded by two garnet Lu-Hf ages of 1931 ± 12 and 1917 ± 6 Ma and overlapping zircon and monazite ages (ca. 1933–1913 Ma; Cutts & Dyck, 2022). Furthermore, the dates yielded by apatite and titanite south of the Laloche River fault (ca. 1860–1760 and ca. 1870–1740 Ma, respectively) post-date the crystallization of plutonic host rocks within the shear zone (> 1930 Ma; Cutts et al., 2022). Together, these relationships indicate that the populations both north and south of the Laloche River fault are unlikely to represent either a primary igneous or prograde metamorphic origin.

Both chronometers record older dates on the north side of the Laloche River fault (Fig. 6) with the oldest apatite and titanite dates occurring in the same two samples: GSL-18-BD07 (apatite 1915 ± 12 Ma; titanite 1904 ± 9 Ma) and GSl-18-C50 (apatite 1918 ± 10 Ma; titanite 1888 ± 11 Ma). Moreover, both chronometers demonstrate an overall younging trend toward the fault in the southern structural domain (Fig. 6). A similar pattern is also reflected in Zr-in-titanite temperatures, which exhibit an overall decrease from south of the study area towards the Laloche River fault (Fig. 6).

In all but three populations (GSL-21-BD27, GSL-21-DS07, clustered titanite in GSL-21-DS16), apatite and titanite grains have a shape-preferred orientation that is aligned with ductile shear fabrics (Figs. 2a, c & d). Considering these textural observations in conjunction with the timing and nature of apatite and titanite (re)crystallization in the shear zone, we interpret the apatite and titanite dates as recording syn-kinematic (re)crystallization, which encompasses both dynamic recrystallization of, or re-equilibration of the U-Pb system in, pre-existing apatite and titanite as well as syn-tectonic growth of new grains. It is possible that the apatite and titanite grains that are aligned with shear planes do not record the timing of the shear process (i.e., they record pre-shear (re)crystallization processes), however, given that the apatite and titanite data are significantly younger than prograde-to-peak metamorphism as outlined above, it is unlikely that these chronometers are recording earlier magmatic or metamorphic events. Moreover, given that apatite and titanite dates at similar structural positions typically overlap, we consider it unlikely that they are cooling ages. Apatite has a nominal closure temperature (in the sense of Dodson, 1973) of ~425–530 ˚C (Chamberlain & Bowring, 2001; Cherniak et al., 1991) whereas recent estimates for titanite closure temperatures are much higher in excess of 700 ˚C (Gao et al., 2012; Kohn, 2017; Kohn & Corrie, 2011; Spencer et al., 2013; Stearns et al., 2015).

While most of the apatite and titanite populations are interpreted to record the timing of ductile shear, two titanite populations (GSL-21-DS07, clustered titanite in GSL-21-DS16) and one apatite population (GSL-18-BD27) exhibit distinct textural and geochemical characteristics that require additional explanation. Titanite grains in GSL-21-DS07 occur predominantly along late coarse-grained quartz-epidote veins (Fig. 2b) and exhibit oscillatory zoning in BSE (Fig S2b). Titanite also occurs in the heavily altered matrix of the sample. These grains display resorption textures and exhibit irregular, patchy zoning (Fig. S2b), which we interpret as textural evidence of fluid alteration. Analyses from the quartz-epidote vein-hosted grains yield flat REE profiles that are distinct from all other titanite populations (Fig. 4b). The lack of enrichment or depletion in any of the REE is consistent with titanite (re)crystallization occurring in a relatively isolated system, away from the presence of other REE-bearing minerals (e.g., allanite, garnet; Garber et al., 2017). This observation is consistent with the interpretation that titanite in this sample (re)crystallized due to the fluid infiltration that resulted in the formation of quartz-epidote veins. Meanwhile, the clustered titanite in GSL-21-DS16 are differentiated from the fabric-aligned titanite in this sample by the absence of a strong positive Eu anomaly in their geochemical signature (Fig. 4b). The positive Eu anomaly exhibited by the fabric-aligned titanite is interpreted as indicating (re)crystallization coeval with plagioclase breakdown (e.g., Garber et al., 2017). Given the geochemical differences between the two populations and the lack of alignment of the clustered titanite with the mylonitic fabric (Fig. 2e), we interpret the clustered titanite as reflecting post-kinematic (re)crystallization in a plagioclase-free environment. Finally, the apatite population in GSL-18-BD27 yields a distinct REE profile with an overall enrichment in REE and a pronounced negative Eu anomaly (Fig. 4a). These geochemical characteristics have been previously interpreted to reflect hydrothermal alteration of apatite (e.g., Adlakha et al., 2018), and while the specific effects of a fluid on apatite REE chemistry may vary between localities, various studies have demonstrated the sensitivity of apatite trace element systematics to hydrothermal activity (e.g., Bouzari et al., 2016; Mao et al., 2016; Ribeiro et al., 2020). Furthermore, although apatite in this sample occurs both in the matrix and as inclusions in garnet, both types of apatite record matching REE signatures (Fig. 4a), which is consistent with all apatite grains re-equilibrating with a fluid.

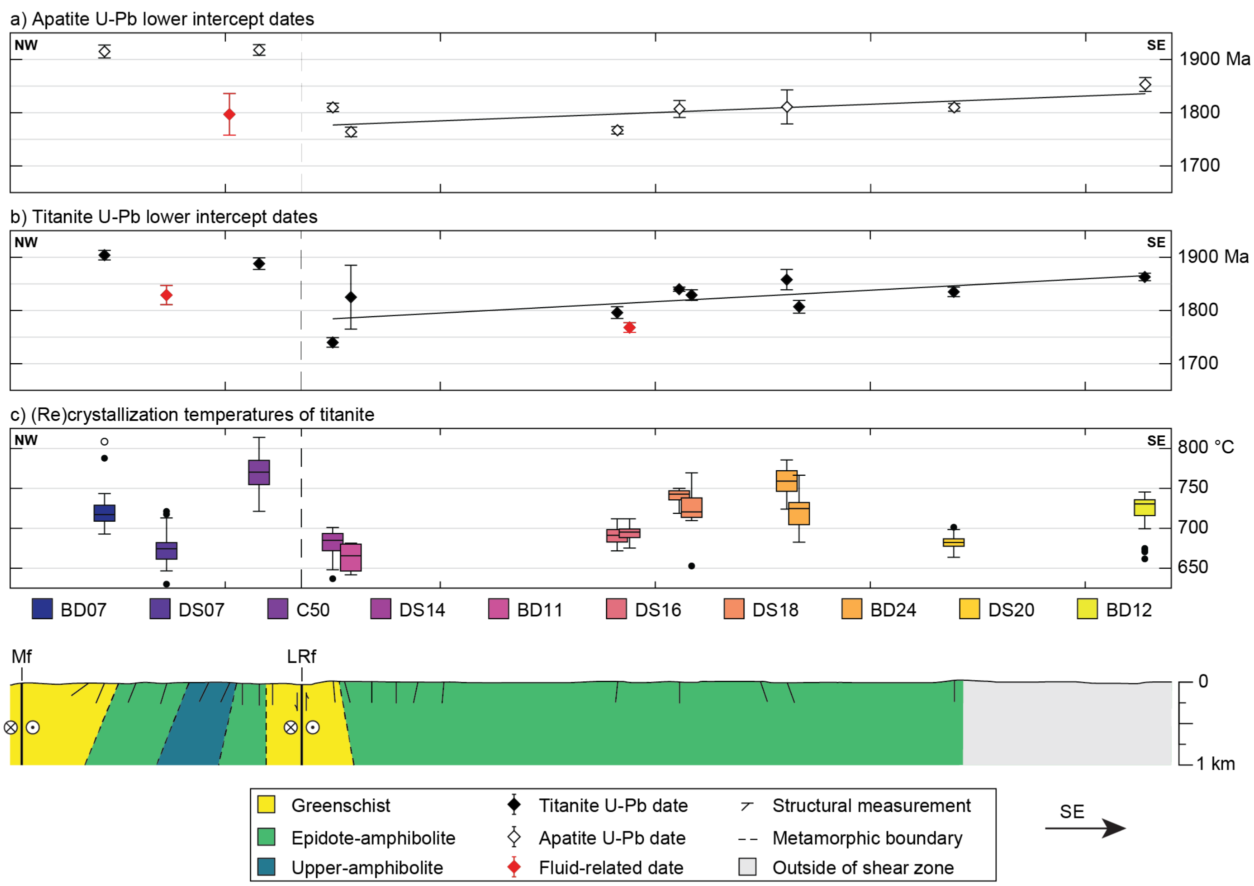


**Figure 6.** Summary of petrochronology results plotted along the transect of the study area (Fig. 1c). The McDonald fault (Mf) and the Laloche River fault (LRf) are marked and the position of the Laloche River fault is indicated on the plots by a dashed line. The horizontal position of each marker corresponds to its approximate position along the transect. (a) Lower intercept dates of apatite with 2σ error bars. A linear fit to the data in the southern structural domain indicates a faultward younging trend. (b) Lower intercept dates of titanite with 2σ error bars. A linear fit to the data in the southern structural domain (excluding clustered titanite in GSL-21-DS16) indicates a faultward younging trend. (c) Box and whisker plot of the titanite (re)crystallization temperatures, calculated using the geothermometer of Hayden et al. (2008). Outliers are indicated by solid and open circles, which correspond to values larger than 1.5 and 3x the interquartile range, respectively.

### 5.2 Architecture and temporal evolution of the GSLsz

Figure 7 presents a simplified model of the GSLsz. This model builds on basic Sibson-Scholz shear zone models, which consist of a zone of active deformation that is narrow near the surface and broadens with depth, giving it a characteristic triangular shape (Scholz, 1988). In the upper crust, deformation is dominated by brittle processes and strain is localized along one or more discrete fault surfaces, whereas in the middle to lower crust, there is a gradual transition from brittle to ductile processes and strain is distributed across a broadening zone of deformation. One key prediction of the Sibson-Scholz model is the overprinting of higher-grade metamorphic mineral assemblages by lower-grade ones, which is observed in all units of the GSLsz. This overprinting is the result of the crust being exhumed and consequently experiencing decreases in both pressure and temperature, reflected by changes in the stable mineral assemblage. Because the metamorphic conditions preserved at the surface level of the GSLsz reflect the lowest-grade mineral assemblages associated with ductile fabrics, the observed metamorphic grade can be used to estimate depth at which a package of crustal material exited the zone of active shear.

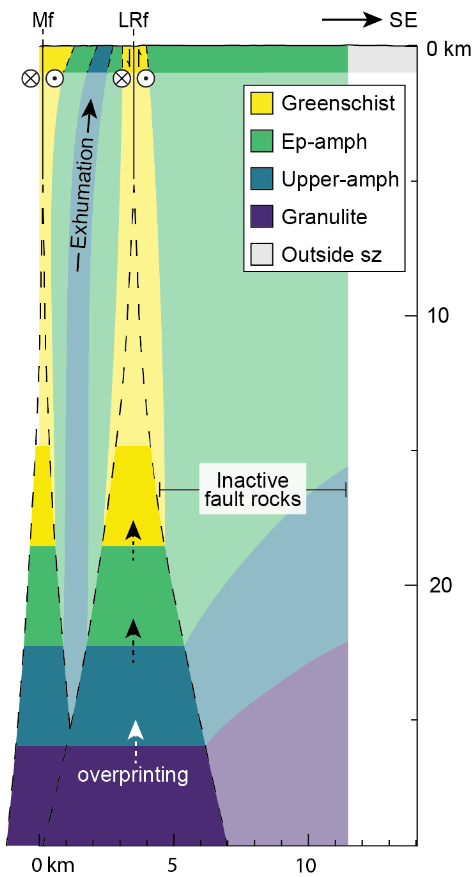


**Figure 7.** Two-strand shear zone model proposed for the GSLsz. The McDonald fault (Mf) and the Laloche River fault (LRf) are marked. The zones of active deformation are outlined by dashed lines. Gs refers to greenschist facies, Ep-amph to epidote-amphibolite facies, and upper-amph to upper-amphibolite facies.

Our simplified model of the GSLsz adopts the peak thermal gradient of ~1000 °C/GPa reported by Dyck et al. (2021), which is based on petrological modelling of units from the northern structural domain. Using this thermal gradient, the depths corresponding to key thermal boundaries between metamorphic facies are estimated by assuming an average overburden density of 2750 kg/m$^3$. The following thermal boundaries are assumed: (1) greenschist facies corresponds to the temperature range of 400–500 °C, (2) epidote-amphibolite facies to 500–600 °C, (3) upper-amphibolite facies to 600–700 °C, and (4) granulite facies to 700–800 °C (Palin & Dyck, 2021). The depths calculated for the thermal boundaries are used to define the vertical extent of metamorphic layers in the shear zone.

Based on the observed symmetry of the metamorphic units exposed between the McDonald and Laloche River faults, we propose that the GSLsz initially had two simultaneously active strands of deformation, with one centered on the McDonald fault and the other centered on the Laloche River fault (Fig. 7). As the width of the actively deforming region narrowed structurally upward, a symmetrical pattern would have developed with respect to the most recent recorded conditions of metamorphism and shear-(re)crystallization. The two greenschist facies belts and neighboring epidote-amphibolite rocks that are centered on the McDonald and Laloche River faults are consistent with progressive localization of strain along these structures.

Figure 8 presents a kinematic model for the GSLsz that builds on the two-strand model presented in Figure 7. By using the apatite ages as a record of the time at which a sample exited the actively deforming shear zone (and stopped (re)crystallizing), we estimate both the position and width of the zones of active deformation over time. We propose three main stages for the temporal evolution of the GSLsz (Fig. 8). In stage 1 (ca. 1920–1880 Ma), there are two strands of active deformation centered on the McDonald and Laloche River faults. In stage 2 (ca. 1880–1800 Ma), ductile deformation associated with the McDonald fault ceases and the locus of deformation shifts southwards towards the Laloche River fault and one (or more) parallel strands operating to the south of the Laloche River fault. During stage 3 (ca. 1800–1740 Ma), the active deformation south of the Laloche River fault migrates northward, leaving no lower-grade brittle record to the south of the fault. From the lack of variability in metamorphic grade on the south side of the Laloche River fault, we interpret that the localization of shear along the fault occurred while the now present-day surface was 15–20 km deep, and still below the base of the seismogenic crust.

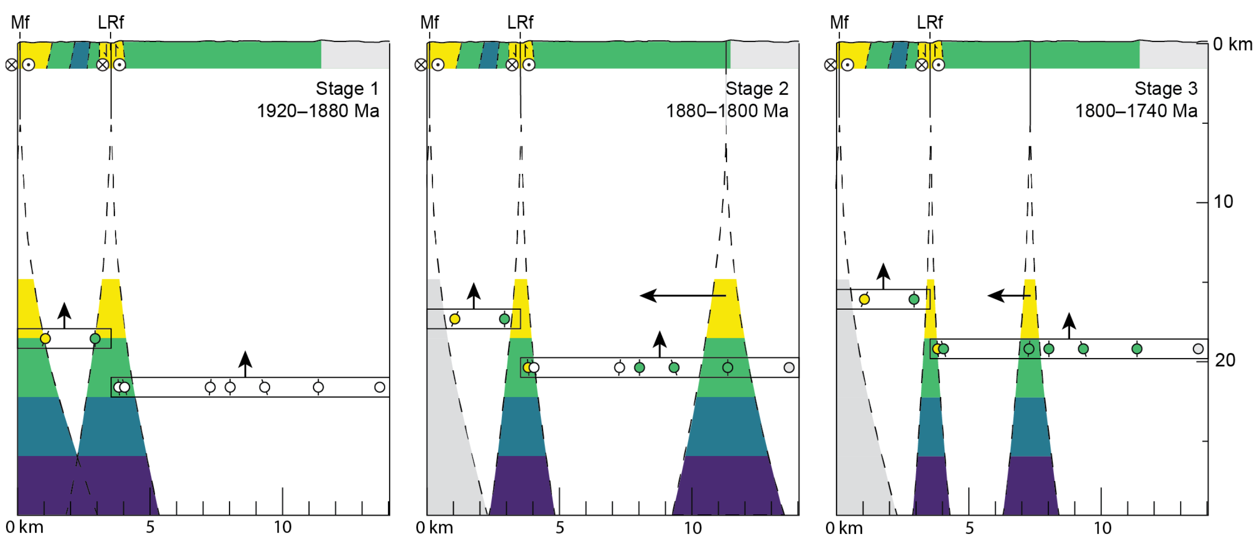


**Figure 8.** Tectonic model for the GSLsz. Colors correspond to metamorphic facies: yellow to greenschist, green to epidote-amphibolite, blue to upper-amphibolite, purple to granulite. A thermal gradient of 1000 °C/GPa is assumed for all stages. Apatite samples are indicated by circles. Colored circles indicate samples that have exited the actively deforming shear zone by

the end of each stage. Arrows illustrate the exhumation of crustal layers as well as the lateral migration of the actively deforming strands over time. The McDonald fault (Mf) and Laloche River fault (LRf) are marked in each panel.

Our kinematic model (Fig. 8) involves a broad width of crust that was last deformed under epidote-amphibolite facies conditions. The active shear zone may have significantly widened when the stress that was originally accommodated by the McDonald fault is transferred southwards into the Rae craton. The Rae cratonic margin would have been relatively young at the time when the GSLsz was developed with voluminous Talston age (1.99–1.92 Ga) plutonism making up the bulk of the leading edge of the craton. It is possible that the (then) recent magmatism would contribute to an elevated crustal thermal gradient and a less-competent Rae margin. Along similar lines, the higher peak-metamorphic conditions and crustal thickening recorded in the northern domain may have led to a dehydrated and more competent Slave margin.

Over the span of 50 to 100 Myr, it is possible that an actively deforming strand shifted laterally by up to 10 km. In our model, the loci of shear shifted back towards the Laloche River fault and the McDonald fault upon exhumation. Therefore, the only evidence of localized, low-grade deformation has been lost due to the erosion of the upper-crustal expressions of these structures. The migration of the actively deforming strands over time does not change the interpretation that the strands decrease in width and range over time.

The presence of multiple active strands within major shear zones, as well as the lateral migration of these actively deforming strands, has been documented in modern-day analogues. The Karakoram fault zone in southwestern Tibet is known to have had several active fault strands throughout its history with varying amounts of slip occurring along each of these structures (e.g., Searle, 1996; Dunlap et al., 1998; Phillips et al., 2004). The North Anatolian fault zone in Turkey provides another example of a major strike-slip fault system consisting of multiple active branches (e.g., Okay et al., 1999; Hejl et al., 2010). Yet another well-known example would be the San Andreas fault system, which consists of over a dozen faults that all record distinct but often overlapping slip histories (e.g., Scharer and Streig, 2019). Each of these major transform systems yields extensive evidence of seismic activity along both main and subsidiary structures, a phenomenon that likely applied to the GSLsz as well.

Our model highlights several key observations, including the discrepancy in ages recorded across the Laloche River fault (Fig. 8). We posit that the Laloche River fault represents a much more significant tectonic boundary than previously thought. Both the apatite and titanite chronometers record significantly older ages of dynamic (re)crystallization on the north side of the Laloche River fault, while on the south side of the fault, they record younger ages that define a younging trend towards the centre of the shear zone. There may be several contributing factors that explain the age and depth discrepancy recorded across the fault, including: 1) a component of dip-slip motion along the Laloche River fault, resulting in the vertical juxtaposition of units of different ages; 2) the Laloche River fault represents a major tectonic boundary with inherent differences in rheology; and 3) there was an increased crustal thermal gradient in the southern structural domain at the time of deformation.

If the first explanation for the age discrepancy holds true, then the age difference recorded across the Laloche River fault could be the result of a north side-down component of dip-slip motion along the fault. Hanmer (1988) and Dyck et al. (2021) report evidence of a shallow north side-down dip-slip component along the Laloche River fault, including mineral lineations and slickenlines along splay fault surfaces. Using the estimates of sample depth from the kinematic model, approximately 2–5 km of dip-slip motion would be required to bring all the samples to the same structural level.

The second explanation for the age discrepancy, which is that the Laloche River fault represents the suture between the Rae and Slave cratons, assumes a difference in crustal affinity across the boundary. This interpretation is consistent with lithological differences found across the shear zone. Recent work focusing on the plutonic rocks hosting the GSLsz has revealed distinct geochemical and geochronological signatures in zircon on either side of the Laloche River fault (Cutts et al., 2022). To the north of the fault, zircon preserve Archean ages and mantle oxygen isotope compositions, while to the south, they are Proterozoic in age and preserve heavier oxygen isotope compositions (Cutts et al., 2022). Additionally, mylonitic rocks on the south side of the Laloche River fault appear to reflect a broadly homogeneous deformation event, with minimal variation in the developed resultant textures and mineral assemblages, while those found north of the Laloche River fault preserve broad ranges in degree of mylonitization as well as metamorphic conditions, which extend up to granulite facies. There is a notable lack of evidence for high-pressure (>1 GPa), migmatization, and granulite facies metamorphism to the south of the fault (Dyck et al., 2021). Another key difference across the Laloche River fault is the presence of metasedimentary lithologies to the north of the fault, whereas none have been documented on the south side, indicating contrasting lithotectonic architectures. Together, these lines of evidence point to a difference in crustal affinity across the Laloche River fault consistent with the Laloche River fault representing the suture between the Rae and Slave cratons.

The third explanation for the age discrepancy involves a difference in crustal thermal gradient across the Laloche River fault. A modest increase in the thermal gradient of the southern structural domain, from 1000 to ~1100 °C/GPa, would reconcile the apparent differences in recrystallization depths at any given time. With the younger ages found only to south of the fault, there is no need for a step-change in temperatures across the fault. Instead, the entire shear zone could have experienced heating as it matured.

Considering the apatite and titanite ages in the context of the Rae-Slave suture, we interpret the older ages on the north side of the suture as recording the initial stages of strike-slip deformation related to the oblique collision between the Rae and Slave cratons. We interpret the ages on the south side of the suture as the broad-scale deformational response of the western Rae cratonic margin to the convergence and subsequent transform motion along the cratonic boundary. As there are no younger ages related to ductile deformation on the north side of the suture, the Slave craton likely remained relatively stable and rigid following its response to the initial collision, whereas the younger and weaker Rae cratonic margin continued to accommodate the bulk of the deformation related to the convergence.

## 6 Conclusions

We present *in situ* U-Pb geochronology results for the shear-induced (re)crystallization of apatite and titanite, which yield new information on the timing and duration of ductile deformation along the GSLsz and record a near-continuous history of ductile shear spanning ca. 1920–1740 Ma. Based on the integration of this new geochronological data with structural and metamorphic observations across the structure, we propose a time-dependent kinematic model for the GSLsz that involves three stages of evolution. During stage 1 (ca. 1920–1880 Ma), ductile shear is localized along two strands of active deformation in the northern structural domain, centered on the McDonald and Laloche River faults. Stage 2 (ca. 1880–1800 Ma) involves the cessation of shear along the McDonald fault and the migration of the locus of deformation into the southern structural domain. Finally, during stage 3 (ca. 1800–1740 Ma), deformation localizes back along the Laloche River fault. These interpretations reveal further complexities in the case of the GSLsz, including the posited presence of the Slave-Rae suture along the Laloche River fault, as supported by other lithological and geochemical work, and the significance of the lateral migration of the zone of active deformation in major crustal shear zones. Our results illustrate the necessity of providing structural and metamorphic context for geochronological data to accurately constrain the evolution of crustal-scale structures and we believe that the approach outlined here is widely applicable to other continental transform systems.

## Acknowledgments

We respectfully acknowledge the unceded traditional territories of the Dene peoples, including the Łútsël K'é (Lutsel K'e) and the Deninu Kų́ę́ (Deninu Kue) First Nations, on which we conducted fieldwork. We thank Mark Button, Sudip Shrestha and Dan Gibson for their technical support and Alix Osinchuk and Rebecca Canam for fieldwork support. Funding for this study was provided by a Natural Sciences and Engineering Research Council (NSERC) graduate scholarship awarded to DS, a NSERC Discovery Grant awarded to BD, as well as support from Natural Resource Canada's Polar Continental Shelf and GEM Geoscience programs.

## Open Research

All U-Pb isotope and trace element data used in this manuscript are available in Supplementary Tables S2–S4 and are also available from the Open Science Framework online repository via https://doi.org/10.17605/OSF.IO/WP3XQ (Šilerová et al., 2022).

## References

Adlakha, E., Hanley, J., Falck, H., & Boucher, B. (2018). The origin of mineralizing hydrothermal fluids recorded in apatite chemistry at the Cantung W–Cu skarn deposit, NWT, Canada. *European Journal of Mineralogy*, *30*(6), 1095–1113. https://doi.org/10.1127/ejm/2018/0030-2780

Apen, F. E., Wall, C. J., Cottle, J. M., Schmitz, M. D., Kylander-Clark, A. R. C., & Seward, G. G. E. (2022). Apatites for destruction: Reference apatites from Morocco and Brazil for U-Pb petrochronology and Nd and Sr isotope geochemistry. *Chemical Geology*, *590*, 120689. https://doi.org/10.1016/j.chemgeo.2021.120689

Berman, R. G., Davis, W. J., Sanborn-Barrie, M., Whalen, J. B., Taylor, B. E., McMartin, I., McCurdy, M. W., Mitchell, R. K., Ma, S., Coyle, M., Roberts, B., & Craven, J. A. (2018). Report of activities for the GEM-2 Chantrey-Thelon activity: Thelon Tectonic Zone project, Nunavut. *Geological Survey of Canada*. https://doi.org/10.4095/306622

Bethune, K. M., Berman, R. G., Rayner, N., & Ashton, K. E. (2013). Structural, petrological and U–Pb SHRIMP geochronological study of the western Beaverlodge domain: Implications for crustal architecture, multi-stage orogenesis and the extent of the Taltson orogen in the

SW Rae craton, Canadian Shield. *Precambrian Research*, *232*, 89–118. https://doi.org/10.1016/j.precamres.2013.01.001

Bostock, H. H., & Loveridge, W. D. (1988). Geochronology of the Taltson Magmatic Zone and its eastern cratonic margin, District of Mackenzie. *Radiogenic Age and Isotopic Studies: Report 2; Geological Survey of Canada, Paper no. 88-2*, 59–65. https://doi.org/10.4095/126603

Bostock, H. H., van Breemen, O., & Loveridge, W. D. (1987). Proterozoic geochronology in the Taltson Magmatic Zone, N.W.T. *Radiogenic Age and Isotopic Studies: Report 1; Geological Survey of Canada, Paper no. 87-2*, 73–80. https://doi.org/10.4095/122751

Bostock, H. H., van Breemen, O., & Loveridge, W. D. (1991). Further geochronology of plutonic rocks in northern Taltson Magmatic Zone, District of Mackenzie, N.W.T. *Radiogenic Age and Isotopic Studies: Report 4; Geological Survey of Canada, Paper no. 90-2*, 67–78. https://doi.org/10.4095/131938

Bouzari, F., Hart, C. J. R., Bissig, T., & Barker, S. (2016). Hydrothermal alteration revealed by apatite luminescence and chemistry: A potential indicator mineral for exploring covered porphyry copper deposits. *Economic Geology*, *111*(6), 1397–1410. https://doi.org/10.2113/econgeo.111.6.1397

Bowring, S. A., Schmus, W. R. V., & Hoffman, P. F. (1984). U–Pb zircon ages from Athapuscow aulacogen, East Arm of Great Slave Lake, N.W.T., Canada. *Canadian Journal of Earth Sciences*, *21*(11), 1315–1324. https://doi.org/10.1139/e84-136

Cawood, T. K., & Platt, J. P. (2021). What controls the width of ductile shear zones? *Tectonophysics*, *816*, 229033. https://doi.org/10.1016/j.tecto.2021.229033

Chacko, T., De, S. K., Creaser, R. A., & Muehlenbachs, K. (2000). Tectonic setting of the Taltson magmatic zone at 1.9–2.0–Ga: A granitoid-based perspective. *Canadian Journal of Earth Sciences*, *37*(11), 1597–1609. https://doi.org/10.1139/e00-029

Chamberlain, K. R., & Bowring, S. A. (2001). Apatite–feldspar U–Pb thermochronometer: A reliable, mid-range (~450°C), diffusion-controlled system. *Chemical Geology*, *172*(1), 173–200. https://doi.org/10.1016/S0009-2541(00)00242-4

Cherniak, D. J., Lanford, W. A., & Ryerson, F. J. (1991). Lead diffusion in apatite and zircon using ion implantation and Rutherford Backscattering techniques. *Geochimica et Cosmochimica Acta*, *55*(6), 1663–1673. https://doi.org/10.1016/0016-7037(91)90137-T

Cutts, J. A., Dyck, B., Davies, J., & Stern, R. (2022). Tectonic setting and provenance of plutonic rocks hosting the Great Slave Lake shear zone from microanalytical zircon U-Pb geochronology and oxygen and hafnium isotopes. *GAC-MAC-IAH-CNC-CSPG 2022 Halifax Meeting: Abstracts*, *45*, 94. https://doi.org/10.12789/geocanj.2022.49.188

Cutts, J. A., & Dyck, B. (2022). Incipient collision of the Rae and Slave cratons at ca. 1.95 Ga. *GSA Bulletin*. https://doi.org/10.1130/B36393.1

Dunlap, W. J., Weinberg, R. F., & Searle, M. P. (1998). Karakoram fault zone rocks cool in two phases. *Journal of the Geological Society*, *155*(6), 903–912. https://doi.org/10.1144/gsjgs.155.6.0903

Dyck, B., Goddard, R. M., Wallis, D., Hansen, L. N., & Martel, E. (2021). Metamorphic evolution of the Great Slave Lake shear zone. *Journal of Metamorphic Geology*, *39*(5), 567–590. https://doi.org/10.1111/jmg.12576

Fisher, C. M., Bauer, A. M., Luo, Y., Sarkar, C., Hanchar, J. M., Vervoort, J. D., Tapster, S. R., Horstwood, M., & Pearson, D. G. (2020). Laser ablation split-stream analysis of the Sm-Nd and U-Pb isotope compositions of monazite, titanite, and apatite – Improvements, potential reference materials, and application to the Archean Saglek Block gneisses. *Chemical Geology*, *539*, 119493. https://doi.org/10.1016/j.chemgeo.2020.119493

Gao, X.-Y., Zheng, Y.-F., Chen, Y.-X., & Guo, J. (2012). Geochemical and U–Pb age constraints on the occurrence of polygenetic titanites in UHP metagranite in the Dabie orogen. *Lithos*, *136–139*, 93–108. https://doi.org/10.1016/j.lithos.2011.03.020

Garber, J. M., Hacker, B. R., Kylander-Clark, A. R. C., Stearns, M., & Seward, G. (2017). Controls on trace element uptake in metamorphic titanite: Implications for petrochronology. *Journal of Petrology*, *58*, 1031–1057. doi:10.1093/petrology/egx046

Gibb, R. A., & Thomas, M. D. (1977). The Thelon front: A cryptic suture in the Canadian Shield? *Tectonophysics*, *38*(3–4), 211–222. https://doi.org/10.1016/0040-1951(77)90211-6

Gordon, S. M., Kirkland, C. L., Reddy, S. M., Blatchford, H. J., Whitney, D. L., Teyssier, C., Evans, N. J., & McDonald, B. J. (2021). Deformation-enhanced recrystallization of titanite drives decoupling between U-Pb and trace elements. *Earth and Planetary Science Letters*, *560*, 116810. https://doi.org/10.1016/j.epsl.2021.116810

Hanmer, S. (1988). Great Slave Lake Shear Zone, Canadian Shield: Reconstructed vertical profile of a crustal-scale fault zone. *Tectonophysics*, *149*(3–4), 245–264. https://doi.org/10.1016/0040-1951(88)90176-X

Hanmer, S., Bowring, S., van Breemen, O., & Parrish, R. (1992). Great Slave Lake shear zone, NW Canada: Mylonitic record of Early Proterozoic continental convergence, collison and indentation. *Journal of Structural Geology*, *14*(7), 757–773. https://doi.org/10.1016/0191-8141(92)90039-Y

Hanmer, S., & Lucas, S. B. (1985). Anatomy of a ductile transcurrent shear: The Great Slave Lake Shear Zone, District of Mackenzie, NWT (preliminary report). *Current Research Part B; Geological Survey of Canada, Paper no. 85-1B*, 7–22. https://doi.org/10.4095/120223

Hayden, L. A., Watson, E. B., & Wark, D. A. (2008). A thermobarometer for sphene (titanite). *Contributions to Mineralogy and Petrology*, *155*(4), 529–540. https://doi.org/10.1007/s00410-007-0256-y

Hejl, E., Bernroider, M., Parlak, O., & Weingartner, H. (2010). Fission-track thermochronology, vertical kinematics, and tectonic development along the western extension of the North Anatolian Fault zone. *Journal of Geophysical Research: Solid Earth*, *115*(B10). https://doi.org/10.1029/2010JB007402

Hoffman, P. F. (1987). Continental transform tectonics: Great Slave Lake shear zone (ca. 1.9 Ga), northwest Canada. *Geology*, *15*(9), 785–788. https://doi.org/10.1130/0091-7613(1987)15<785:CTTGSL>2.0.CO;2

Hoffman, P. F. (1988). United Plates of America, the birth of a craton: Early Proterozoic assembly and growth of Laurentia. *Annual Review of Earth and Planetary Sciences*, *16*(1), 543–603. https://doi.org/10.1146/annurev.ea.16.050188.002551

Horstwood, M. S. A., Košler, J., Gehrels, G., Jackson, S. E., McLean, N. M., Paton, C., Pearson, N. J., Sircombe, K., Sylvester, P., Vermeesch, P., Bowring, J. F., Condon, D. J., & Schoene, B. (2016). Community-derived standards for LA-ICP-MS U-(Th-)Pb geochronology – Uncertainty propagation, age interpretation and data reporting. *Geostandards and Geoanalytical Research*, *40*(3), 311–332. https://doi.org/10.1111/j.1751-908X.2016.00379.x

Hull, J. (1988). Thickness-displacement relationships for deformation zones. *Journal of Structural Geology*, *10*(4), 431–435. https://doi.org/10.1016/0191-8141(88)90020-X

Kapp, P., Manning, C. E., & Tropper, P. (2009). Phase-equilibrium constraints on titanite and rutile activities in mafic epidote amphibolites and geobarometry using titanite–rutile equilibria. *Journal of Metamorphic Geology*, *27*(7), 509–521. https://doi.org/10.1111/j.1525-1314.2009.00836.x

Kavanagh-Lepage, C., Gervais, F., Larson, K., Grazziani, R., & Moukhsil, A. (2022). Deformation induced decoupling between U-Pb and trace elements in titanite revealed through petrochronology and study of localized deformation. *Geoscience Frontiers*. https://doi.org/10.1016/j.gsf.2022.101496

Kohn, M. J. (2017). Titanite petrochronology. *Reviews in Mineralogy and Geochemistry*, *83*(1), 419–441. https://doi.org/10.2138/rmg.2017.83.13

Kohn, M. J., & Corrie, S. L. (2011). Preserved Zr-temperatures and U–Pb ages in high-grade metamorphic titanite: Evidence for a static hot channel in the Himalayan orogen. *Earth and Planetary Science Letters*, *311*(1–2), 136–143. https://doi.org/10.1016/j.epsl.2011.09.008

Larson, K. P. (2022). ChrontouR: Geochronology plotting scripts in R [Software]. Open Science Framework. https://doi.org/10.17605/OSF.IO/P46MB

Lusk, A. D. J., & Platt, J. P. (2020). The deep structure and rheology of a plate boundary-scale shear zone: Constraints from an exhumed Caledonian shear zone, NW Scotland. *Lithosphere*, *2020*(1), 8824736. https://doi.org/10.2113/2020/8824736

Ma, S. M., Kellett, D. A., Godin, L., & Jercinovic, M. J. (2020). Localisation of the brittle Bathurst fault on pre-existing fabrics: A case for structural inheritance in the northeastern Slave craton, western Nunavut, Canada. *Canadian Journal of Earth Sciences*, *57*(6), 725–746. https://doi.org/10.1139/cjes-2019-0100

Mao, M., Rukhlov, A. S., Rowins, S. M., Spence, J., & Coogan, L. A. (2016). Apatite trace element compositions: A robust new tool for mineral exploration. *Economic Geology*, *111*(5), 1187–1222. https://doi.org/10.2113/econgeo.111.5.1187

McDonough, M. R., McNicoll, V. J., Schetselaar, E. M., & Grover, T. W. (2011). Geochronological and kinematic constraints on crustal shortening and escape in a two-sided oblique-slip collisional and magmatic orogen, Paleoproterozoic Taltson magmatic zone, northeastern Alberta. *Canadian Journal of Earth Sciences, 37*(11), 1549–1573. https://doi.org/10.1139/e00-089

Miller, A. R., Cumming, G. L., & Krstic, D. (1989). U–Pb, Pb–Pb, and K–Ar isotopic study and petrography of uraniferous phosphate-bearing rocks in the Thelon Formation, Dubawnt Group, Northwest Territories, Canada. *Canadian Journal of Earth Sciences*, *26*(5), 867–880. https://doi.org/10.1139/e89-070

Moser, A. C., Hacker, B. R., Gehrels, G. E., Seward, G. G. E., Kylander-Clark, A. R. C., & Garber, J. M. (2022). Linking titanite U-Pb dates to coupled deformation and dissolution-reprecipitation. *Contributions to Mineralogy and Petrology*, *177*(3), 42. https://doi.org/10.1007/s00410-022-01906-9

Mulch, A., Teyssier, C., Cosca, M. A., & Vennemann, T. W. (2006). Thermomechanical analysis of strain localization in a ductile detachment zone. *Journal of Geophysical Research: Solid Earth*, *111*(B12). https://doi.org/10.1029/2005JB004032

Odlum, M. L., & Stockli, D. F. (2020). Geochronologic constraints on deformation and metasomatism along an exhumed mylonitic shear zone using apatite U-Pb, geochemistry, and microtextural analysis. *Earth and Planetary Science Letters*, *538*, 116177. https://doi.org/10.1016/j.epsl.2020.116177

Okay, A. I., Demirbağ, E., Kurt, H., Okay, N., & Kuşçu, İ. (1999). An active, deep marine strike-slip basin along the North Anatolian fault in Turkey. *Tectonics*, *18*(1), 129–147. https://doi.org/10.1029/1998TC900017

Oriolo, S., Wemmer, K., Oyhantçabal, P., Fossen, H., Schulz, B., & Siegesmund, S. (2018). Geochronology of shear zones – A review. *Earth-Science Reviews*, *185*, 665-683. https://doi.org/10.1016/j.earscirev.2018.07.007

Palin, R. M., & Dyck, B. (2021). Metamorphism of pelitic (Al-rich) rocks. In D. Alderton & S. A. Elias (Eds.), *Encyclopedia of Geology* (Second Edition, pp. 445–456). Academic Press. https://doi.org/10.1016/B978-0-08-102908-4.00081-3

Paton, C., Hellstrom, J., Paul, B., Woodhead, J., & Hergt, J. (2011). Iolite: Freeware for the visualisation and processing of mass spectrometric data. *Journal of Analytical Atomic Spectrometry*, *26*(12), 2508. https://doi.org/10.1039/c1ja10172b

Phillips, R. J., Parrish, R. R., & Searle, M. P. (2004). Age constraints on ductile deformation and long-term slip rates along the Karakoram fault zone, Ladakh. *Earth and Planetary Science Letters*, *226*(3–4), 305–319. https://doi.org/10.1016/j.epsl.2004.07.037

Platt, J. P., & Behr, W. M. (2011). Deep structure of lithospheric fault zones. *Geophysical Research Letters*, *38*(24). https://doi.org/10.1029/2011GL049719

Powell, R., Green, E. C. R., Marillo Sialer, E., & Woodhead, J. (2020). Robust isochron calculation. *Geochronology*, *2*, 325–342. https://doi.org/10.5194/gchron-2-325-2020

Rainbird, R. H., & Davis, W. J. (2007). U-Pb detrital zircon geochronology and provenance of the late Paleoproterozoic Dubawnt Supergroup: Linking sedimentation with tectonic reworking of the western Churchill Province, Canada. *GSA Bulletin, 119*(3–4), 314–328. https://doi.org/10.1130/B25989.1

Ribeiro, B. V., Lagoeiro, L., Faleiros, F. M., Hunter, N. J. R., Queiroga, G., Raveggi, M., Cawood, P. A., Finch, M., & Campanha, G. A. C. (2020). Strain localization and fluid-assisted deformation in apatite and its influence on trace elements and U–Pb systematics.

*Earth and Planetary Science Letters*, *545*, 116421. https://doi.org/10.1016/j.epsl.2020.116421

Scharer, K., & Streig, A. (2019). The San Andreas fault system: Complexities along a major transform fault system and relation to earthquake hazards. In *Transform Plate Boundaries and Fracture Zones* (pp. 249–269). Elsevier. https://doi.org/10.1016/B978-0-12-812064-4.00010-4

Schoene, B., & Bowring, S. A. (2006). U–Pb systematics of the McClure Mountain syenite: Thermochronological constraints on the age of the $^{40}Ar/^{39}Ar$ standard MMhb. *Contributions to Mineralogy and Petrology*, *151*(5), 615. https://doi.org/10.1007/s00410-006-0077-4

Scholz, C. H. (1988). The brittle-plastic transition and the depth of seismic faulting. *Geologische Rundschau*, *77*(1), 319–328. https://doi.org/10.1007/BF01848693

Searle, M. P. (1996). Geological evidence against large-scale pre-Holocene offsets along the Karakoram Fault: Implications for the limited extrusion of the Tibetan plateau. *Tectonics*, *15*(1), 171–186. https://doi.org/10.1029/95TC01693

Sibson, R. H. (1977). Fault rocks and fault mechanisms. *Journal of the Geological Society*, *133*(3), 191–213. https://doi.org/10.1144/gsjgs.133.3.0191

Sibson, R. H. (1983). Continental fault structure and the shallow earthquake source. *Journal of the Geological Society*, *140*(5), 741–767. https://doi.org/10.1144/gsjgs.140.5.0741

Šilerová, D., Dyck, B., Cutts, J. A., & Larson, K. (2022) GSLsz apatite and titanite geochronology [Dataset]. Open Science Framework. https://doi.org/10.17605/OSF.IO/WP3XQ

Spandler, C., Hammerli, J., Sha, P., Hilbert-Wolf, H., Hu, Y., Roberts, E., & Schmitz, M. (2016). MKED1: A new titanite standard for in situ analysis of Sm–Nd isotopes and U–Pb geochronology. *Chemical Geology*, *425*, 110–126. https://doi.org/10.1016/j.chemgeo.2016.01.002

Spencer, K. J., Hacker, B. R., Kylander-Clark, A. R. C., Andersen, T. B., Cottle, J. M., Stearns, M. A., Poletti, J. E., & Seward, G. G. E. (2013). Campaign-style titanite U–Pb dating by laser-ablation ICP: Implications for crustal flow, phase transformations and titanite closure. *Chemical Geology*, *341*, 84–101. https://doi.org/10.1016/j.chemgeo.2012.11.012

Stacey, J. S., & Kramers, J. D. (1975). Approximation of terrestrial lead isotope evolution by a two-stage model. *Earth and Planetary Science Letters*, *26*(2), 207–221. https://doi.org/10.1016/0012-821X(75)90088-6

Stearns, M. A., Hacker, B. R., Ratschbacher, L., Rutte, D., & Kylander-Clark, A. R. C. (2015). Titanite petrochronology of the Pamir gneiss domes: Implications for middle to deep crust exhumation and titanite closure to Pb and Zr diffusion. *Tectonics*, *34*(4), 784–802. https://doi.org/10.1002/2014TC003774

Thériault, R. J. (1992). Nd isotopic evolution of the Taltson Magmatic Zone, Northwest Territories, Canada: Insights into early Proterozoic accretion along the western margin of the Churchill Province. *The Journal of Geology*, *100*(4), 465–475.

Thomson, S. N., Gehrels, G. E., Ruiz, J., & Buchwaldt, R. (2012) Routine low-damage apatite U-Pb dating using laser ablation–multicollector–ICPMS. *Geochemistry, Geophysics, Geosystems*, *13*(2), Q0AA21. https://doi.org/10.1029/2011GC003928

van Breemen, O., Hanmer, S., & Parrish, R. R. (1990) Archean and Proterozoic mylonites along the southeastern margin of the Slave Structural Province, Northwest Territories. *Radiogenic Age and Isotopic Studies: Report 3; Geological Survey of Canada, Paper no. 89-2*, 55–61. https://doi.org/10.4095/129070

Vermeesch, P. (2018). IsoplotR: A free and open toolbox for geochronology. *Geoscience Frontiers*, *9*(5), 1479–1493. https://doi.org/10.1016/j.gsf.2018.04.001

Visual DataTools, Inc. (2021). DataGraph (Version 5.0) [Software]. https://www.visualdatatools.com/

Wallis, D., Lloyd, G. E., & Hansen, L. N. (2018). The role of strain hardening in the transition from dislocation-mediated to frictional deformation of marbles within the Karakoram Fault Zone, NW India. *Journal of Structural Geology*, *107*, 25–37. https://doi.org/10.1016/j.jsg.2017.11.008

Walters, J. B., Cruz-Uribe, A. M., Song, W. J., Gerbi, C., & Biela, K. (2022). Strengths and limitations of in situ U–Pb titanite petrochronology in polymetamorphic rocks: An example from western Maine, USA. *Journal of Metamorphic Geology*, *40*(6), 1043–1066. https://doi.org/10.1111/jmg.12657

Whitney, D. L., & Evans, B. W. (2010). Abbreviations for names of rock-forming minerals. *American Mineralogist*, *95*, 185–187. https://doi.org/10.2138/am.2010.3371

*Tectonics*

Supporting Information for

**Long-lived (180 Myr) ductile flow within the Great Slave Lake shear zone**

D. Šilerová[1], B. Dyck[2], J. A. Cutts[2,3], and K. Larson[2]

[1] Department of Earth Sciences, Simon Fraser University, Burnaby, BC, Canada; [2] Department of Earth, Environmental and Geographical Sciences, University of British Columbia, Kelowna, BC, Canada; [3] Geological Survey of Canada, 601 Booth Street, K1A 0E8, Ottawa, ON, Canada

## Contents of this file

Text S1
Figures S1 to S2

## Additional Supporting Information (Files uploaded separately)

Captions for Tables S1 to S4

## Introduction

This supplement includes detailed petrographic descriptions for the eleven samples selected for *in situ* U-Th-Pb accessory mineral petrochronology as well as supplementary figures containing apatite and titanite trace element analyses and images of representative apatite and titanite grains. Tables containing instrumentation settings for LA-ICP-MS analyses, apatite and titanite U-Pb and trace element data, and Zr-in-titanite temperature data are uploaded separately.

**Text S1.**

**Sample petrography:**

For the following petrographic descriptions, samples are ordered geographically from northwest to southeast. Four of the eleven samples (GSL-18-BD07, GSL-21-DS07, GSL-18-BD27, GSL-18-C50) were collected north of the Laloche River fault while the remaining seven are from south of the fault.

Sample GSL-18-BD07 is a greenschist facies ultramylonitic granodiorite that was collected from the northernmost greenschist belt (Fig. 1c). The metamorphic mineral assemblage is epidote–titanite–chlorite–biotite–muscovite–plagioclase–quartz–K-feldspar with relict amphibole and accessory (<0.5 modal%) apatite. Apatite grains occur primarily in the matrix and typically range from 50–100 μm in diameter (Fig. 2a). Most apatite grains are sub- to anhedral, although several preserve evidence of a hexagonal habit, and grains exhibit patchy core-rim zoning in CL (Fig. S1a). Titanite grains only occur in the matrix and are well-aligned with the foliation (Fig. 2a). They range from 60–700 μm in diameter and typically have an elongate sub- to euhedral shape. Most titanite grains appear either homogeneous in BSE or exhibit irregular, patchy zoning (Fig. S2a).

Sample GSL-21-DS07 is a heavily altered epidote-amphibolite facies mylonitic schist that was collected from the northernmost epidote-amphibolite belt (Fig. 1c). The metamorphic mineral assemblage is epidote–chlorite–feldspar–quartz with accessory titanite. The sample exhibits a weak foliation that is defined by the orientation of chlorite grains as well as by a pervasive network of thin anastomosing opaque-lined fractures. Late, coarse-grained quartz-epidote veins are present in the sample and crosscut the main matrix foliation; the majority of titanite grains occur along the boundaries of these veins (Fig. 2b). Several titanite grains also occur in the matrix, but these contain a higher density of inclusions and, therefore, were not selected as targets. Titanite grains range from 200–1000 μm in diameter. The quartz-epidote vein-hosted titanite grains are euhedral and exhibit oscillatory zoning in BSE (Fig. S2b). In contrast, matrix-hosted titanite grains display resorption textures and exhibit irregular, patchy zoning (Fig. S2b).

Sample GSL-18-BD27 is an upper-amphibolite facies garnet mylonitic schist that was collected from the upper-amphibolite belt (Fig. 1c). The metamorphic mineral assemblage is garnet–sillimanite–biotite–plagioclase–quartz with accessory apatite. The alignment of individual biotite grains defines an irregular, wavy foliation that wraps porphyroclasts of garnet. Apatite grains are found primarily in the matrix, although some occur as inclusions in garnet porphyroclasts. Apatite range from 50–200 μm in diameter and are typically rounded, subhedral and exhibit no zoning in CL (Fig. S1b).

Sample GSL-18-C50 is an epidote-amphibolite facies amphibole mylonitic schist that was collected immediately north of the Laloche River fault (Fig. 1c). The metamorphic mineral assemblage is clinozoisite–amphibole–biotite–titanite–chlorite–quartz–albite–K-feldspar with accessory apatite. The sample consists of a very fine-grained mylonitic matrix with large (cm-scale) winged porphyroclasts that record a dextral shear sense. The sample exhibits a penetrative foliation that is defined by the alignment of matrix minerals. The matrix is primarily composed of chlorite, plagioclase, quartz and K-feldspar, and wraps large clinozoisite–amphibole–titanite pseudomorphs after garnet (Dyck et al., 2021). Apatite grains in this sample occur both in the matrix, where they are aligned with the foliation, and within the pseudomorphed garnet domains, where they tend to be oriented oblique to the main matrix foliation. Apatite grains range from 50–400 μm in diameter and are anhedral and fractured. Grains exhibit either patchy or core-rim zoning in CL (Fig. S1c). Titanite grains are typically oriented oblique to the main matrix foliation and range from 100–800 μm in diameter. The grains are rhombic and exhibit either patchy or oscillatory zoning in BSE (Fig. S2c).

Sample GSL-21-DS14 is a greenschist facies amphibole mylonitic granodiorite that was collected from a mafic boudin in the greenschist facies belt immediately to the south of the Laloche River fault (Fig. 1c). The metamorphic mineral assemblage is biotite–amphibole–plagioclase–K-feldspar–calcite–quartz with secondary chlorite and accessory apatite, titanite and allanite. Fine-grained micaceous domains wrap around winged amphibole and feldspar porphyroclasts, defining a penetrative foliation (Fig. 2c). Coarser-grained regions of quartz, biotite and chlorite are observed adjacent to large porphyroclasts. Quartz ribbons display a crystallographic preferred orientation under the tint plate, consistent with dextral shear. Apatite grains only occur in the matrix, are well-aligned with the foliation and range from 60–500 μm in diameter. Grains are elongate and commonly exhibit patchy CL zoning (Fig. S1d). Titanite grains in this sample occur only in the matrix, are aligned with the foliation, and are relatively small (50–200 μm in diameter; Fig. 2c). Titanite grains exhibit core-rim zoning in BSE (Fig. S2d).

Sample GSL-18-BD11 is an epidote-amphibolite facies mylonitic granodiorite collected south of Laloche River fault (Fig. 1c). The metamorphic mineral assemblage is biotite–quartz–albite–K-feldspar with accessory apatite and titanite. The thin section exhibits a strong, anastomosing foliation defined by the alignment of biotite and by the orientation of planar quartz ribbons. Quartz ribbons display a crystallographic preferred orientation under the tint plate consistent with dextral shear. Apatite grains occur primarily in the matrix and are well-aligned with the foliation. Grains range from 60–250 μm in diameter and are typically sub- to anhedral and elongate. The grains commonly exhibit either oscillatory or core-rim zoning in CL (Fig. S1e). Titanite grains are uncommon, occurring primarily along micaceous layers, and are very small, ranging from 20–120 μm in diameter. Titanite grains are blocky in shape and exhibit little to no zoning in BSE (Fig. S2e).

Sample GSL-21-DS16 is an epidote-amphibolite facies amphibole mylonitic granodiorite that was collected from a mafic boudin south of Laloche River fault (Fig. 1c). The metamorphic mineral assemblage is amphibole–plagioclase–biotite–epidote–quartz with secondary chlorite and accessory apatite and titanite. This sample exhibits a strong foliation that is defined by the alignment of amphibole and biotite. Apatite grains commonly occur in amphibole-rich domains and are well-aligned with the foliation (Fig. 2e). Apatite grains range in diameter from 80–250 μm, are typically rounded and elongate in shape and exhibit irregular core-rim zoning in CL (Fig. S1f). Two populations of titanite were identified based on textural observations (Fig. 2e). The first population consists of sub- to anhedral titanite grains that are well-aligned with the foliation (referred to as "fabric-aligned titanite"), while the second consists of round titanite grains clustered together around long masses of ilmenite (referred to as "clustered titanite"). Grain size varies similarly across both populations, ranging from 25–120 μm. Clusters of titanite are typically elongate and can reach up to 500 μm in length. Both populations of titanite exhibit some evidence of core-rim zoning in BSE (Figs. S2f & g).

Sample GSL-21-DS18 is an epidote-amphibolite facies amphibole mylonitic granodiorite that was collected from a strongly foliated mafic boudin at an outcrop otherwise dominated by pink, heteroclastic mylonitic granodiorite host rock. The metamorphic mineral assemblage is amphibole–biotite–plagioclase–quartz with secondary chlorite and accessory titanite, apatite and monazite. The sample exhibits a strong foliation that is defined by the alignment of planar quartz ribbons, biotite and chlorite, all of which wrap amphibole and plagioclase porphyroclasts (Fig. 2d). Apatite occurs primarily in the matrix and grains range from 50–200 μm in diameter. They are elongate, aligned with the foliation and exhibit patchy zoning with uncommon bright core domains in CL (Fig. S1g). Titanite only occurs in the matrix and is commonly associated with biotite. Titanite grains range from 50–350 μm in diameter and are elongate in shape, aligned with the foliation (Fig. 2d). Most grains exhibit irregular, patchy zoning in BSE (Figs. S2h & i).

Sample GSL-18-BD24 is an epidote-amphibolite facies amphibole mylonitic granodiorite collected south of Laloche River fault (Fig. 1c). The metamorphic mineral assemblage is amphibole–biotite–titanite–albite–epidote–quartz with secondary chlorite and accessory apatite. This sample is medium-grained with a strong foliation defined by the crystallographic and shape preferred orientation of amphibole grains. Apatite occurs primarily in the matrix and grains range from 50–200 μm in diameter. Apatite grains are elongate, aligned with the foliation and exhibit patchy zoning with uncommon bright core domains in CL (Fig. S1h). Titanite grains occur in the matrix, are well-aligned with the foliation, ranging in diameter from 100–1500 μm. The grains are sub- to anhedral and exhibit distinct core and rim structures in transmitted light and BSE (Figs. 2f, S2j & k).

Sample GSL-21-DS20 is an epidote-amphibolite facies amphibole mylonitic granodiorite that is the southernmost sample analyzed from the shear zone (Fig. 1c). The thin section from this sample features both the mafic boudin and the pink, homoclastic mylonitic host rock. The metamorphic mineral assemblage amphibole–epidote–biotite–plagioclase–quartz with secondary chlorite and accessory titanite and apatite. The sample exhibits a strong foliation that is defined by the alignment of amphibole, biotite and chlorite. Apatite grains only occur in the matrix and range from 70–300 μm in diameter.

Apatite grains are elongate in shape, aligned with the foliation, and exhibit irregular oscillatory zoning in CL (Fig. S1i). Titanite grains are aligned with the foliation and commonly associated with amphibole and biotite. Titanite grains range from 50–500 μm in diameter, are rhombic in shape and do not typically exhibit internal zoning in BSE (Fig. S2l).

Sample GSL-21-BD12 is an upper-amphibolite facies amphibole schist that was collected from a supracrustal unit in the Rutledge Group, ~10 km to the south of the previously defined southern boundary of the shear zone (Fig. 1c). The metamorphic mineral assemblage is amphibole–plagioclase–quartz–biotite–chlorite with accessory titanite, apatite and monazite. The sample is strongly foliated, as defined by the shape and crystallographic preferred orientation of amphibole and biotite grains. The thin section exhibits a flattened equigranular texture, with interlocking plagioclase, quartz, and amphibole grains separated by thin lenticular domains of fine-grained micaceous and quartz-rich material. Apatite occurs either in the matrix or as inclusions in amphibole grains. Apatite grains range from 50–200 μm in diameter, are anhedral and exhibit patchy core-rim zoning in CL (Fig. S1j). Titanite grains occur in the matrix, are well-aligned with the foliation, and range from 50–200 μm in diameter. The grains exhibit a range of shapes, from blocky to anhedral, and often have patchy, core-rim zoning in BSE (Fig. S2m).

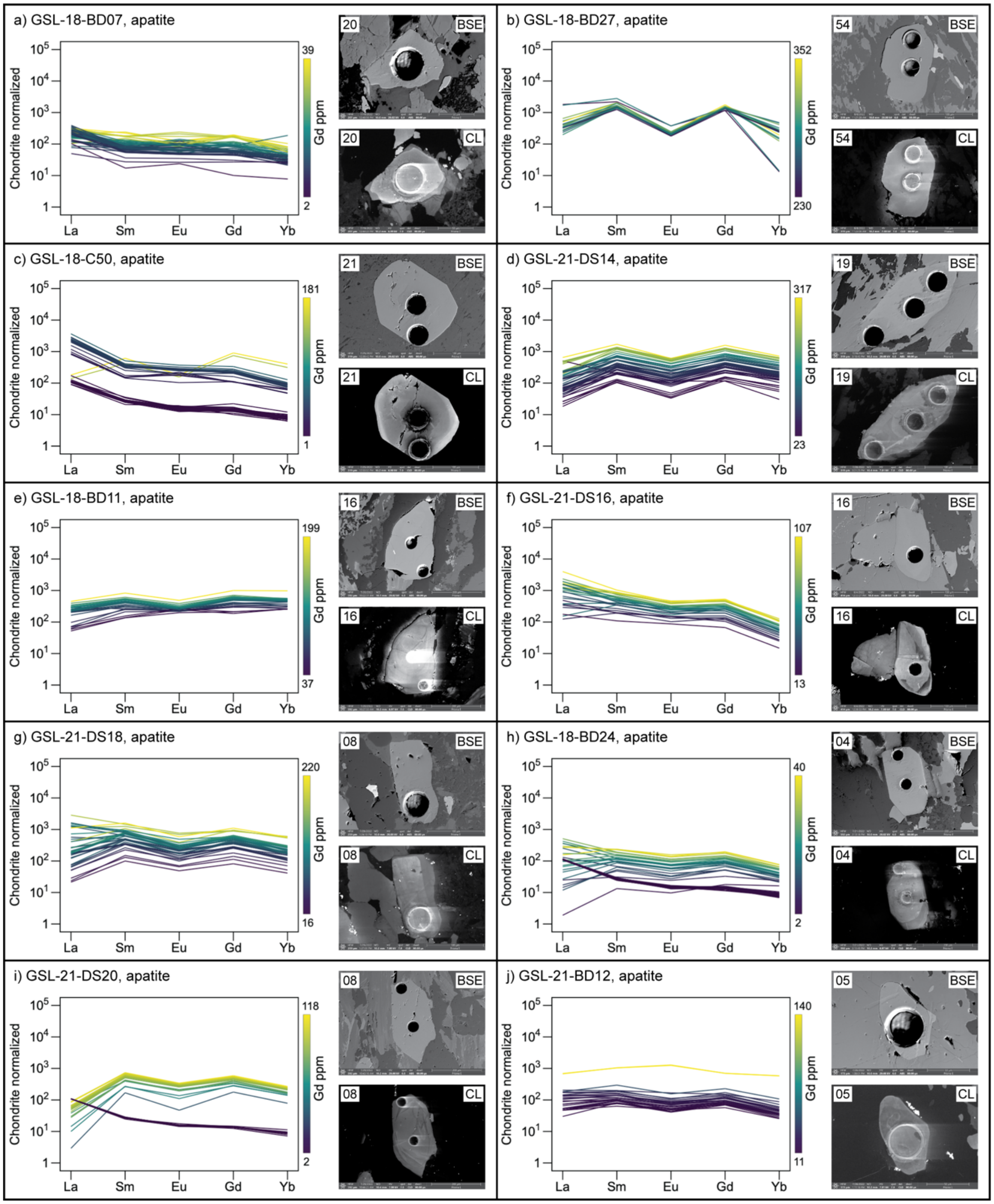


**Figure S1.** Trace element results for all apatite populations plotted on chondrite-normalized REE plots. BSE and CL images of representative grains are shown for each population. Populations (samples) are ordered geographically from NW to SE.

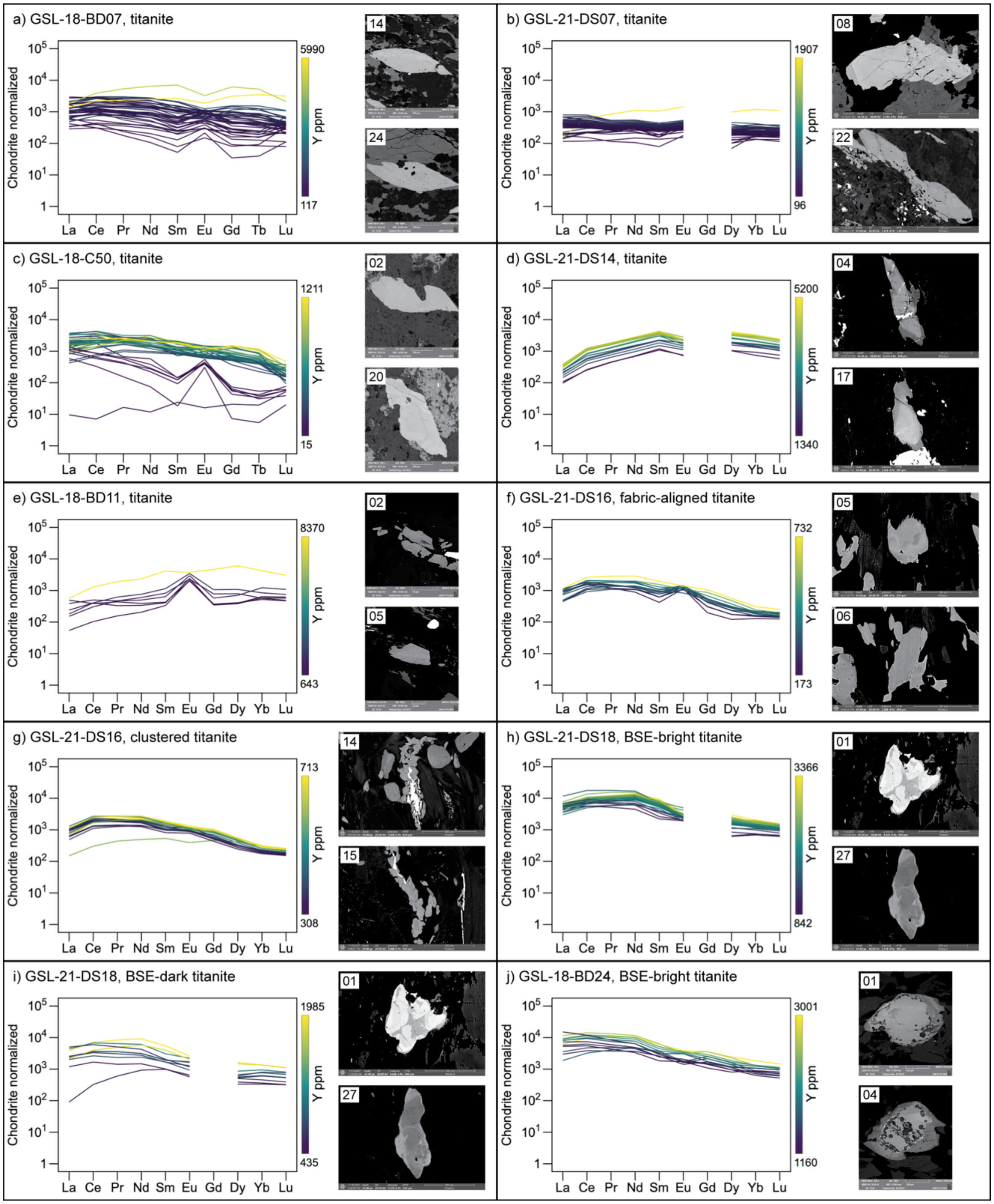
a) GSL-18-BD07, titanite
b) GSL-21-DS07, titanite
c) GSL-18-C50, titanite
d) GSL-21-DS14, titanite
e) GSL-18-BD11, titanite
f) GSL-21-DS16, fabric-aligned titanite
g) GSL-21-DS16, clustered titanite
h) GSL-21-DS18, BSE-bright titanite
i) GSL-21-DS18, BSE-dark titanite
j) GSL-18-BD24, BSE-bright titanite
Chondrite normalized
Y ppm
La Ce Pr Nd Sm Eu Gd Tb Lu
La Ce Pr Nd Sm Eu Gd Dy Yb Lu

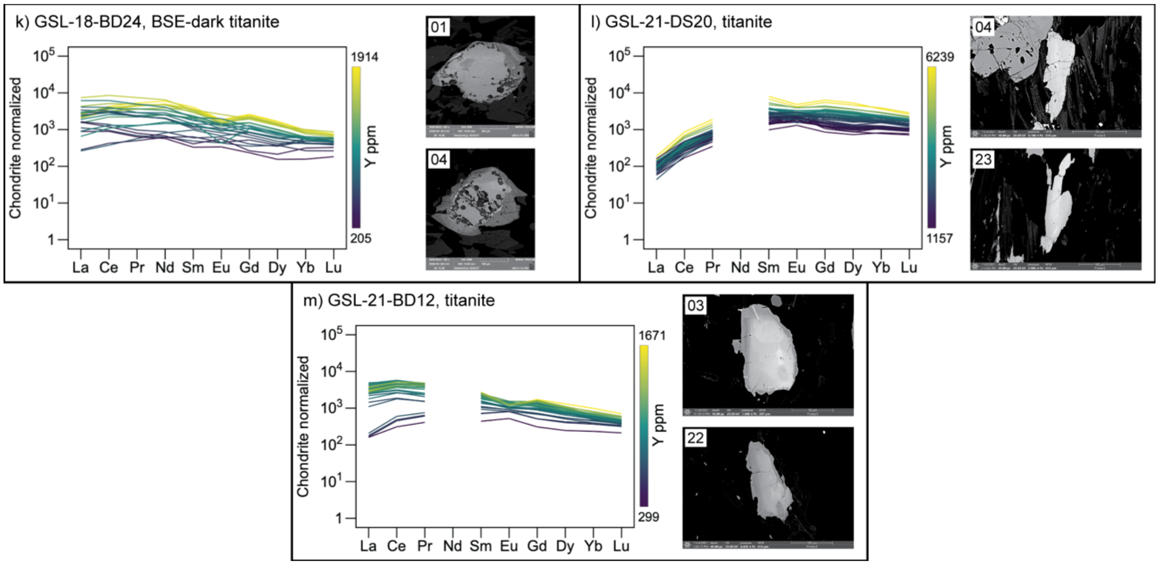


**Figure S2.** Trace element results for all titanite populations plotted on chondrite-normalized REE plots. BSE images of representative grains are shown for each population. Populations (samples) are ordered geographically from NW to SE.

**Table S1.** LA-ICP-MS metadata for all analytical sessions.

**Table S2.** Apatite U-Pb isotope and trace element data (unknowns and reference materials).

**Table S3.** Titanite U-Pb isotope and trace element data (unknowns and reference materials).

**Table S4.** Zr-in-titanite geothermometry results for all titanite analyses.